

# Predictive capability of coupled rock behaviour – development of an experimentally based benchmark for numerical quality assurance (BeNuQuA)

## Authors

MSc. Lucas Witte, MSc. Hossein Asghari Chehreh  
Prof. Tobias Backers  
Dr. Mandy Duda  
Dr. Murat Aydin  
BSc. Sasan Parvin

## Contact

Ruhr-University Bochum  
Prof. Dr. Tobias Backers  
Engineering Geology and Rock Mass Mechanics  
Universitätsstraße 150, 44801 Bochum, Germany  
Email: tobias.backers@rub.de

Bochum, 10.10.2024

# Summary

Simulation tasks and numerical codes have become increasingly complex in the context of temporal and spatial upscaling for understanding and predicting subsurface rock mass mechanics, for example associated with radioactive waste disposal. Benchmark procedures based on laboratory datasets are required to verify the predictive capabilities of computational approaches. In this study, a high-quality laboratory dataset of conventional geomechanical experiments on granite was generated. Numerical simulations of the experiments were performed as proof-of-concept using COMSOL Multiphysics and RocScience RS to derive a benchmark procedure for numerical quality assurance that can be applied to computational approaches in the context of nuclear waste disposal and beyond.

The laboratory schedule was specifically developed for the numerical simulation of time-dependent deformation characteristics in granite. Splitting tensile strength, uniaxial compressive strength, and triaxial compressive strength of carefully characterised specimens were investigated at different strain rates covering five orders of magnitude. Strength decreased with decreasing strain rate, and the presence of water decreased strength significantly. A significant contribution of end face friction in the experimental setup to the results of strength tests was verified and recommendations for preparational and experimental procedures in deformation experiments on granite were derived.

Based on the laboratory dataset, 2D numerical simulations with RocScience RS2 successfully reproduced the effect of different lubricants to modify end face friction on strength, and COMSOL Multiphysics was able to reproduce the time-dependent deformation characteristics observed for granite. Using crack phase field damage modelling, COMSOL Multiphysics predicted triaxial compressive strength from uniaxial compressive strength by adjusting nothing but the boundary conditions. In both approaches, the adaptation of microstructural properties was required to successfully simulate the experimental findings pointing to a distinct need to further improve the understanding of microstructural processes causing the time-dependent deformation characteristics and to evaluate the potential for temporal upscaling to long-term processes exceeding those covered by laboratory experiments.

The results of this study will significantly contribute to gaining more confidence in the predictive capabilities of numerical codes and identify code-specific parameters that are critical for successful prediction.

# Content

<b>Context .....</b>	<b>11</b>
<b>Organisation of the project .....</b>	<b>13</b>
<b>Laboratory program .....</b>	<b>14</b>
1. Sample material and specimen preparation.....	14
2. Basic rock physical characterisation .....	17
2.1 Methodology.....	17
2.2 Results from basic characterisation.....	19
3. Strength testing.....	22
3.1 Methodology.....	23
3.2 Results and discussion of strength testing .....	23
3.2.1 Splitting tensile strength tests .....	24
3.2.2 Uniaxial compressive strength tests .....	25
Effect of end face friction .....	25
Analysis of strain rate and saturation.....	28
Analysis of length-to-diameter ratio .....	30
3.2.3 Triaxial compressive strength tests .....	32
Effect of strain-rate and saturation.....	32
Analysis of Mohr-Coulomb failure criterion .....	35
Analysis of shear failure experiments .....	36
3.2.4 Micromechanics .....	39
Computer Tomographic Scans (CT-scans) .....	39
Subcritical crack growth .....	40
3.2.5 Acoustic Emission (AE) analysis .....	40
<b>Numerical Simulations.....</b>	<b>43</b>
1. Fundamental modelling principles of crystalline rock failure.....	43
1.1 Numerical approach 1: Crack phase field damage model (CPFDM) .....	43
1.2 Numerical approach 2: Voronoi grain-based model (VGBM).....	47
2. Model configuration .....	48
2.1 Calibration assumptions .....	50
2.1.1 CPFDM-COMSOL .....	50
2.1.2 CPFDM-COMSOL sensitivity analysis .....	52
2.2 VGBM-RS2 .....	53
2.2.1 VGBM-RS2 sensitivity parameters analysis .....	54
2.3 Input calibrated parameters .....	57
3. A posteriori-simulation of experiments .....	59
3.1 Basic model and strain rate effect simulation .....	59
3.1.1 CPFDM-COMSOL basic model .....	59
3.1.2 Strain rate effect simulation with CPFDM-COMSOL.....	60
3.1.3 VGBM-RS2 basic model .....	62
3.2 STS test simulations with calibrated parameters .....	62
3.2.1 STS simulation with CPFDM-COMSOL .....	63
3.2.2 STS simulation with VGBM-RS2 .....	68
4. A priori-simulation of experiments .....	70
4.1 Overview of end friction effect on mechanical laboratory tests .....	70
4.2 End friction effect simulation with VGBM-RS2 .....	72
4.3 Triaxial compressive strength test simulation with CPFDM-COMSOL .....	79
4.4 Triaxial compressive test simulation with VGBM-RS2 .....	82
4.5 Accuracy of predictions.....	83

<b>Workflow for benchmarking .....</b>	<b>86</b>
<b>Conclusions, outlook and limitations .....</b>	<b>90</b>
1. Laboratory program .....	90
2. Numerical simulation .....	91
3. Limitations.....	92
4. Data access .....	93
<b>References .....</b>	<b>94</b>
<b>Digital Appendix .....</b>	<b>100</b>
1. Geophysical parameters.....	100
2. Geomechanical parameters .....	100
3. COMSOL Multiphysics - CPFDM .....	100
3.1 Models of UCS test simulation.....	100
3.2 Models of STS test simulation .....	100
3.3 Models of TCS test simulation .....	100
4. RS2 Rocscience - VGBM .....	100
4.1 Models of UCS test simulation.....	100
4.2 Models of STS test simulation .....	100
4.3 Models of TCS test simulation .....	100

# List of Figures

Figure 1: Final status of planned (black) and completed (grey) laboratory program. The number of planned uniaxial compressive strength tests was exceeded by tests with different lubricants The number of previously 54 planned permeability tests was reduced to five tests due to very low permeability in agreement with SSM. ....	14
Figure 2: Computertomographic scan (CT-Scan) of specimen PG3-36, drilled in x-direction: 3D view (left) and axial cross section (right). Biotite (white), quartz (dark grey) and feldspar (light grey) can be recognised. ....	20
Figure 3: Optical images in cross-polarized light with 1) biotite, 2) quartz and 3) feldspar for different thin section orientations of PG1 (left), PG2 (middle) and for three different specimens tested for tensile strength after failure with loading direction from top to bottom (right). Scale is identical for all images. In thin section PG1, scratch marks are recognisable that were created during the preparation process. ....	21
Figure 4: Results of permeability tests at different pore pressure gradients and constant mean effective stresses of 3 MPa. Tests were performed on specimens orientated in x direction of block 1, block 2 and block 3. ....	22
Figure 5: Relations between ultrasound velocities and dry density (a) and thermal conductivity and total porosity (b). Circles represent P-wave velocity, triangles symbolise S-wave velocity (left); circles represent the top end face, triangles symbolise the bottom end face (right). ....	22
Figure 6: Splitting tensile strength vs displacement rate for block 1 (a) and block 2 (b), no loading point lubricant was used. The letters (x, y, z) indicate the direction of drilling when preparing the specimens. ....	24
Figure 7: Averaged (if applicable) uniaxial compressive strength vs strain rate for oven-dried specimens, using no lubricant, Teflon of 0.5 mm and 0.025 mm thickness and graphite powder as lubricant. Error bars indicate the standard deviation. ....	26
Figure 8: Fracture pattern from uniaxial compressive strength test of specimens where (a) no lubricant, (b) graphite powder, (c) Teflon 0.025 mm and (d) Teflon 0.5 mm was used. The red lines visualise macroscopic fractures. Scale is identical for all images. ....	27
Figure 9: Frequency of fracture patterns of oven-dried specimens in relation of various lubricants and strain rates. ./ denotes that no tests were performed. Light grey to dark grey represents axial splitting, wedge failure and shear failure. ....	28
Figure 10: Uniaxial compressive strength vs strain-rate for oven-dried and saturated specimens of Padang granite TG34 drilled in X-direction. Graphite powder was used as lubricant. Each symbol represents one uniaxial compressive strength test. Black circles: series PG2a, grey circles: series PG2b (attention: see discussion in text on validity of results), black triangles: series PG3a, blue triangles: series 3b, fluid saturated. ....	29
Figure 11: Young`s modulus vs strain rate for oven-dried and saturated specimens of Padang granite TG34 drilled in X-direction. Graphite powder was used as lubricant. Each symbol represents one uniaxial compressive strength test. Black circles: series PG2a, grey circles: series PG2b (attention: see discussion in text on validity of results), black triangles: series PG3a, blue triangles: series 3b, fluid saturated. ....	29

Figure 12: Results of oven-dried uniaxial compressive strength tests with (a) different length to diameter ratios and different diameters (b) at a strain rate of $1 \cdot 10^{-5} \text{ s}^{-1}$ . Graphite powder was used as lubricant, the specimens were in y-direction orientated. ....	31
Figure 13: Triaxial compressive strengths vs strain rate for specimens being oven-dried, saturated during the TCS test and saturated to constant mass before assembling at 3, 5 and 9 MPa confining pressure using graphite powder as lubricant. ....	34
Figure 14: Angle of internal friction (a) and cohesion (b) vs strain rate for oven-dried specimens tested by 3, 5 and 9 MPa confining pressure. ....	35
Figure 15: Fracture angle of incidence vs nominal strain rate for specimens being oven-dried and saturated to constant mass tested by 3, 5 and 9 MPa confining pressure using graphite powder as lubricant. ....	36
Figure 16: Friction angle vs strain rate for specimens being oven-dried and saturated to constant mass tested by 3, 5 and 9 MPa confining pressure using graphite powder, 0.5 mm – 0.25 mm thick Teflon and no lubricant. ....	37
Figure 17: Results of triaxial compressive strength for oven-dried specimens at a nominal strain rate of $10^{-5} \text{ s}^{-1}$ using different lubricants. Each symbol represents one experiment. ....	37
Figure 18: Fracture pattern from triaxial compressive strength test of specimens where (a) no lubricant, (b) graphite powder, (c) Teflon 0.025 mm and (d) Teflon 0.5 mm was used. The red lines visualise macroscopic fractures. Scale is identical for all images. ....	38
Figure 19: Computertomographic scans (CT-Scan) of oven-dried specimens after uniaxial (left) and triaxial (right) compressive strength test at a strain rate of $10^{-4} \text{ s}^{-1}$ and 5 MPa confining pressure. Biotite (white), quartz (light grey) and feldspar (dark grey) can be recognised. ....	39
Figure 20: AE records of oven-dried Padang granite TG34 specimens at 9 MPa confining pressure and at a strain rate of (a) $1 \cdot 10^{-7} \text{ s}^{-1}$ , (b) $1 \cdot 10^{-5} \text{ s}^{-1}$ , and (c) $1 \cdot 10^{-3} \text{ s}^{-1}$ . Blue line indicates axial load, green and red triangles represent AE-events shorter and longer than 100 $\mu\text{s}$ , the green line illustrates the cumulative number of hits. ....	41
Figure 21: Number of AE-events vs strain rate for oven-dried specimens tested under triaxial compression at 9 MPa confining pressure. AE-events louder than 52 dB were measured only. ....	42
Figure 22: Triaxial compressive strength vs number of AE-events for oven-dried specimens tested under triaxial compression at 9 MPa confining pressure. AE-events louder than 52 dB were measured only. ....	42
Figure 23: Stages of crack development in rock during uniaxial compressive test and its representation in the mechanic and phase field model. ....	44
Figure 24: The mineralogical parameters used for CPFDM based on image analysis technique (a) photo of Padang granite TG34, (b) mineral's Young's modulus distribution in STS and (c) mineral's Young's modulus distribution in UCS. ....	49
Figure 25: (a) Uniaxial compressive strength test model used by VGBM-RS2, (b) lubricant position, (c) free triangular mesh in COMSOL, (d) uniaxial compressive strength test model used by CPFDM-COMSOL, (e) triangular mesh in RS2, (f) pre-existing and new crack in CPFDM, (g) Goodman's joint element in the interface between two blocks, (h) new existing crack in phase field model. ....	50
Figure 26: Calibration flowchart of main parameters in CPFDM-COMSOL (MF: material factor). ....	51

Figure 27: Effect of critical stress and relation between frequency of pre-existed micro crack and UCS (material factor, $\xi = 1$ ). .....	52
Figure 28: Relation between material factor and UCS. ....	52
Figure 29: Calibration flowchart of main parameters in VGBM-RS2. ....	54
Figure 30: Sensitivity analysis of Mohr-coulomb parameters of VGBM-RS2: (a) effect of cohesion of grain and grain boundary on UCS, (b) effect of friction angle of grain and grain boundary on UCS. ....	55
Figure 31: Sensitivity analysis of stiffness parameters of VGBM-RS2: (a) effect of the $Kn/Ks$ ratio on bulk Young's modulus and UCS, (b) effect of $Kn$ on Young's modulus and UCS with constant $Kn/Ks$ ratio, (c) effect of Poisson's ratio of grain on UCS and Poisson's ratio of model. ....	56
Figure 32: Numerical uniaxial compression test results of specimens used to investigate the effect of nine different grain arrangements. ....	57
Figure 33: Stress-strain curves of basic model of CPFDM-COMSOL. ....	59
Figure 34: (a) Crack initiation, (b) final failure, and (c) post failure in basic model of CPFDM-COMSOL. ....	60
Figure 35: Stress-strain curves of UCS with different strain rate simulation with CPFDM-COMSOL. ....	61
Figure 36: Failure and post failure stage of UCS for different strain rate simulations with CPFDM-COMSOL. ....	61
Figure 37: Stress-strain curves of basic model simulation of VGBM-RS2. ....	62
Figure 38: STS test model configuration (a) VGBM-RS2, (b) CPFDM-COMSOL. ....	63
Figure 39: Axial load – axial displacement curve of STS tests with different displacement rates from CPFDM-COMSOL. ....	64
Figure 40: Microscopic view of tensile fracture under cross-polarized light: STS test with (a) displacement rate $1.5 \cdot 10^{-4} \text{ mm.s}^{-1}$ , (b) displacement rate $1.5 \cdot 10^{-3} \text{ mm.s}^{-1}$ , (c) displacement rate $1.5 \cdot 10^{-2} \text{ mm.s}^{-1}$ . ....	64
Figure 41: STS test simulation of displacement rate $1.5 \cdot 10^{-4} \text{ mm.s}^{-1}$ with CPFDM-COMSOL: (a) crack initiation, (b) crack propagation, (c) final failure and (d) thin section in natural light. ....	65
Figure 42: STS test simulation of displacement rate $1.5 \cdot 10^{-3} \text{ mm.s}^{-1}$ with CPFDM-COMSOL: (a) crack initiation, (b) crack propagation, (c) final failure and (d) thin section in natural light. ....	66
Figure 43: STS test modelling of displacement rate $1.5 \cdot 10^{-2} \text{ mm.s}^{-1}$ with CPFDM-COMSOL (a) Crack initiation, (b) Crack propagation, (c) final failure and (d) Thin section in natural light. ....	67
Figure 44: STS test simulation from VGBM-RS2. ....	68
Figure 45: Progressive failure of VGBMs of Padang granite TG34 intact rock under STS test. (a) Maximum shear strain and (b) stress in xx direction or tensile stress at first crack initial stage (left) and different stages of failure (right). ....	69
Figure 46: Illustration of confined zones due to frictional end effects in specimens in rock UCS: (a) hoop stress in upper surface of specimen, (b) high friction contact, (c) low	

friction contact [80]; [81], (d) end friction effect BSF and (e) UCS with no friction effect. ....	71
Figure 47: Result of numerical simulation of UCS tests without and with different lubricants. ....	73
Figure 48: Specimen length vs lateral displacement of UCS test modelling without and with different lubricants. ....	74
Figure 49: Lateral tensile and compressional stress in UCS model without and with different lubricants in VGBM-RS2. ....	75
Figure 50: Failure modes under unconfined compression in VGBM-RS2 and laboratory: (a-d) without lubricant, (e-h) with Teflon 0.025 mm, (i-l) with graphite powder; (d, h & l) represent minor principal strain in the upper part of the sample and they are scaled between 0 to 0.001. Legend refers only to a, e, i. ....	77
Figure 51: Stress-strain-relations of UCS tests in experiments and simulated with VGBM-RS2 without lubricant. ....	78
Figure 52: Stress-strain-relations of UCS tests in experiments and simulated with VGBM-RS2 with graphite powder. ....	78
Figure 53: Stress-strain-relations of UCS tests in experiments and simulated with VGBM-RS2 with Teflon 0.025 mm. ....	79
Figure 54: Fracture modes under triaxial compression with strain rate $1 \cdot 10^{-5} \text{ s}^{-1}$ in CPFDM-COMSOL and laboratory: (a & c) diagonal micro fractures in triaxial test with 3 MPa confining pressure (b & d) vertical micro fractures in triaxial test with 5 MPa confining pressure. ....	80
Figure 55: Result of numerical simulation of TCS tests under strain rate $1 \cdot 10^{-5} \text{ s}^{-1}$ with 6 MPa pore pressure. ....	81
Figure 56: Comparing laboratory results of TCS tests with strain rate $1 \cdot 10^{-5} \text{ s}^{-1}$ under 6 MPa pore pressure in experiments and simulated with CPFDM-COMSOL ....	81
Figure 57: Results of numerical simulation of TCS tests under strain rate $1 \cdot 10^{-4} \text{ s}^{-1}$ with graphite powder as a lubricant. ....	82
Figure 58: Comparing laboratory results TCS tests with graphite powder as a lubricant in experiments and simulated with VGBM-RS2. ....	83
Figure 59: Comparing results from experiments and numerical simulations of geomechanical tests of Padang granite TG34. ....	85
Figure 60: Schematic workflow with several steps for benchmarking. ....	89



# List of Tables

Table 1: Parameters determined to select suitable sample material for the study. The Padang granite TG34 was chosen due to its comparable grain size and similar uniaxial compressive strength to Forsmark granite[73];[79].	15
Table 2: Summary of the results of the basic characterisation. For individual experimental results see Appendix. <b>n</b> denotes the number of performed tests.	20
Table 3: Number of splitting tensile strength tests (sts), uniaxial compressive strength tests (ucs) and triaxial compressive strength tests (tcs). 267 Padang granite specimens were investigated. ./ denotes that no experiments of that kind were performed to this point.	24
Table 4: Results of splitting tensile strength tests and standard deviation, no loading point lubricant was used. Specimens were prepared in x-, y-, z-direction from block 1 and block 2.	25
Table 5: Mechanical properties of oven-dried Padang granite TG34 at different strain rates (average and standard deviation, if applicable) for different lubricants placed between specimens and loading plates. The values represent from top to bottom the UCS ( $\sigma_c$ ) in MPa and Young's Modulus (E) in GPa. ./ denotes that no experiments of that kind were performed to this point.	26
Table 6: Results of 18 uniaxial compressive strength tests with different length-to-diameter ratios. Graphite powder was used as lubricant, the specimens were in y-direction orientated.	31
Table 7: Results of individual triaxial compressive strength tests with pore pressure of 6 MPa at different effective confining pressure. The specimens were saturated during TCS test and saturated to constant mass before assembling.	33
Table 8: Friction criteria after Mohr-Coulomb derived from single stage triaxial compressive strength tests of oven-dried specimens at different strain rates using graphite powder as lubricant. ./ denotes that no tests were performed.	35
Table 9: Results of shear failure experiments derived from single stage triaxial compressive strength tests of oven-dried and saturated to constant mass specimens at different strain rates using various lubricants.	36
Table 10: Subcritical crack growth index for Padang granite TG34.	40
Table 11: Effect of the number of finite elements on VGBM-RS2 response.	57
Table 12: Calibrated micro-parameters used in the VGBM-RS2 for basic model of Padang granite TG34.	58
Table 13: Calibrated micro-parameters used in the CPFDM-COMSOL for basic model of Padang granite TG34.	58
Table 14: Comparing results of Padang granite TG34 experimental UCS test and modelling with the CPFDM-COMSOL under different strain rate.	60
Table 15: Physical and mechanical properties of lubricants [33] ( <a href="https://catalog.wshampshire.com/asset/psg_teflon_ptfe.pdf">https://catalog.wshampshire.com/asset/psg_teflon_ptfe.pdf</a> ).	72
Table 16: Applied friction coefficients at specimen's end faces.	72

Table 17: Comparison of numerical and experimental results for uniaxial compressive strength tests with different lubricants. ....	73
Table 18: Numerical results for radial (lateral) strains at failure base on Barrel shape factor. ....	74
Table 19: Comparison of numerical and experimental results for TCS tests under strain rate $1 \cdot 10^{-5} \text{ s}^{-1}$ . ....	80
Table 20: Comparison of numerical and experimental results for TCS tests under strain rate $1 \cdot 10^{-4} \text{ s}^{-1}$ with graphite powder as a lubricant. ....	82
Table 21: Comparison of numerical and experimental results for STS tests. ....	83
Table 22: Comparison of numerical and experimental results for UCS tests. ....	84
Table 23: Comparison of numerical and experimental results for TCS tests under strain rate $1 \cdot 10^{-4} \text{ s}^{-1}$ with graphite powder as a lubricant by VGBM and strain rate $1 \cdot 10^{-5} \text{ s}^{-1}$ with 6 MPa pore pressure by CPFDM. ....	84

# Context

In modern rock mass mechanics numerical simulation is key to predict and understand the behaviour of the subsurface. This is true also for the Swedish radioactive waste disposal applications. Both, the simulation tasks and numerical codes have become increasingly complex. Modern codes show mostly impressive success regarding the ability to reproduce experimental or field data. Adjusting material parameters and constitutive laws of numerical models as part of the calibration procedure is inevitable to correctly reproduce the physical data. However, the validity of the physical basis for realistically looking predictions is at least questioned when physical problems and/or codes require extensive tuning.

Hence, an objective procedure to verify if codes are capable to mirror and predict physical processes is needed to gain trust in simulations related to sensitive applications like disposal of nuclear waste.

When using numerical codes to predict rock mass behaviour, their validity is usually tested against (a) analytical solutions and (b) experimental observations. The main purpose of a comparison within analytical solutions is to reveal programming flaws, because the analytical and numerical result to the constitutive equation the code is based on should be equivalent within numerical uncertainty; exceptions from this is e.g. PFC, which does not use direct physically based constitutive equations. Such tests become increasingly complex, when coupling phenomena are involved, e.g. hydromechanical or thermomechanical coupling.

The comparison with experimental observations is a fundamental part of the verification of numerical results when applying codes to problems of higher complexity or spatial or temporal scales beyond that of experiments. However, the need for intensive tuning drives this verification procedure ad absurdum.

Industrial and academic numerical codes developed during the past decades are in principle capable of investigating rock behaviour in simple to complex geological settings. While these codes are validated against analytical solutions, that are however based on the same assumptions underlying the numerical approach and succeed to simulate observed characteristics a posteriori by adjusting model parameters, material properties and constitutive laws, the robustness of results for predictive purposes has not yet been studied systematically and leaves a severe gap in terms of numerical quality assurance. The next logical step, the prediction of a-priori unknown physical data, is hardly performed.

For the Centennial AGU (American Geophysical Union) Fall meeting (2019) a session on damage evolution in rock titled ‘Validation data sets and computational challenges’ convened by well-known Laura Pyrak-Nolte had been announced. The motivation for the session was that “few computational approaches for simulating damage have been verified against readily available experimental data or have been validated via blind predictions of data sets ahead of data acquisition”. The announcement of the session also points out “the urgent need for code comparison programs [...]” in brittle-ductile materials.

This code comparison may not only be done by inter-code-comparison of complex datasets like in DECOVALEX (DEvelopment of COupled models and their VALidation against Experiments), but also with the help of

- a high-quality laboratory dataset, that is suitable for benchmarking a wide range of numerical codes, and
- deriving a benchmark procedure that can be used to validate numerical codes applied for prediction of rock mass behaviour.

Within this project ‘Predictive capability of coupled rock behaviour - development of an experimentally based benchmark for numerical quality assurance (BeNuQuA)’

- (a) a reliable, reproducible dataset of conventional laboratory experiments was generated,
- (b) numerical simulations of the experiments were performed as proof-of-concept using COMSOL Multiphysics and RocScience RS, and
- (c) a benchmark procedure for numerical quality assurance (NQA) that can be applied to any codes when simulating processes in the context of nuclear waste disposal was developed.

As a by-product, recommendations for sample preparation and procedures in conventional laboratory experiments exceeding those typically published within standards and suggested methods were derived specifically for granite samples.

The results of this study will significantly contribute to gaining more confidence in the predictive capabilities of numerical codes and identify code-specific parameters that are highly critical for successful prediction. The outcome of this project may be implemented into Quality Assurance schemes.

# Organisation of the project

The project aims at providing (a) a reliable, reproducible dataset of conventional laboratory experiments along with (b) simulations of the laboratory data. From these two integral parts of the project (c) a benchmark procedure to verify the capability of simulation software to not only re-simulate physical experiments but also to predict the mechanical behaviour of rock is proposed.

The original workplan consisted of four main work-packages (WPs). The general structure of the original workplan was maintained; however, some deviations and optimisations were done in coordination with SSM.

In Work Package 1 ‘Organisation and Preparation’ the laboratory programme was defined, the sample material for the laboratory campaign was selected, and the basic rock physical characterisation was performed.

The laboratory experimental program (WP 1.1 Definition of the experimental program) was defined such that a distinct set of basic rock parameters for numerical model input was prepared. The programme was specifically designed for numerical simulation of hydro-mechanically coupled rock behaviour. By the program it was provided that

- the variability of the rock properties is reflected, and
- the experiments have the potential to reflect coupled hydro-mechanical behaviour
- while considering potential limitations in the availability of sample material from natural drill cores.

The laboratory programme was discussed with and approved by SSM.

‘Sample collection’ (WP 1.2) was conducted such that a rock was identified that may be assumed representative for applications in nuclear waste. Starting with four granite varieties, it was decided in the course of the project to focus on one sample material. Specimen preparation was done from blocks ordered specifically for the project.

The ‘Basic rock physical characterisation’ (WP 1.3) for numerical model input was done according to the outcomes of WP 1.1 and 1.2.

More complex experiments for numerical simulations were conducted in Work Package 2 (Experimental Program). This focused on uniaxial and triaxial experiments at defined boundary conditions.

The numerical simulations (WP 3) of the physical experiments as performed in WP 2 were run using COMSOL Multiphysics and RocScience RS. Based on the insights from WP 3 the benchmarking procedure (WP 4.2) is suggested.

The project started in July 2021 and ended in August 2024. A final workshop presenting the main findings of the projects was held 2<sup>nd</sup> October 2024. The project was coordinated by Prof. Tobias Backers and Dr. Mandy Duda. The laboratory campaign was conducted by Lucas Conrad Witte. The numerical simulations were run by Hossein Armin Asghari Chehreh, Dr. Murat Aydin and Sasan Parvin.. The laboratory campaign started in October 2021 and preceded the numerical campaign by about four months.

# Laboratory program

The laboratory experimental plan has been developed specifically for numerical simulation of hydro-mechanical coupling processes and provides a set of basic physical parameters for model input. The plan has been presented to SSM on 18th February 2022 and accounts for key aspects such as anisotropy, reproducibility, sample and specimen variability, experimental uncertainty and a careful documentation of the experimental procedure. Results provide information on static and dynamic elastic, inelastic, hydraulic, thermal and friction parameters of the investigated rocks. Experiments were performed considering effects of specimen size, applied rates, water content and pore pressure. The planned and performed experiments are shown in Figure 1.

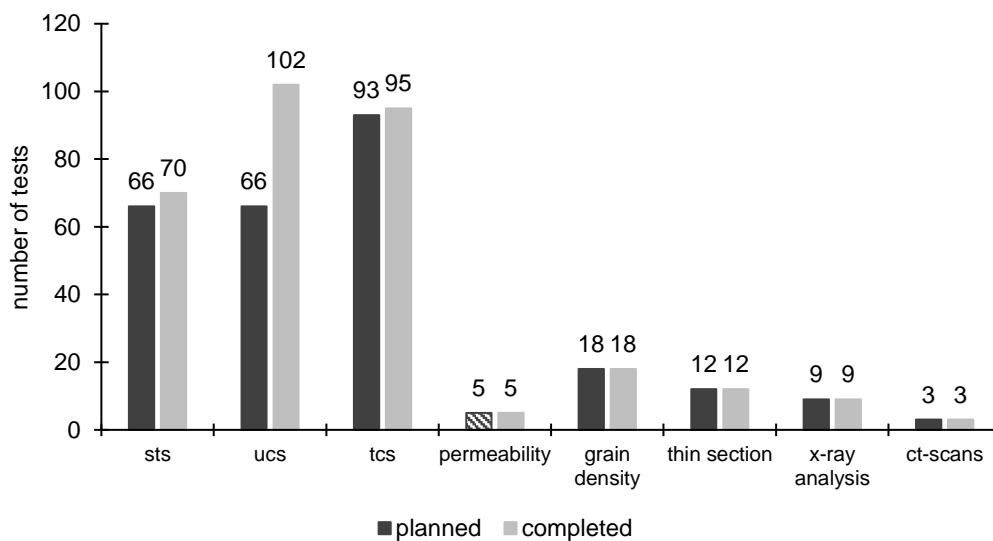


Figure 1: Final status of planned (black) and completed (grey) laboratory program. The number of planned uniaxial compressive strength tests was exceeded by tests with different lubricants. The number of previously 54 planned permeability tests was reduced to five tests due to very low permeability in agreement with SSM.


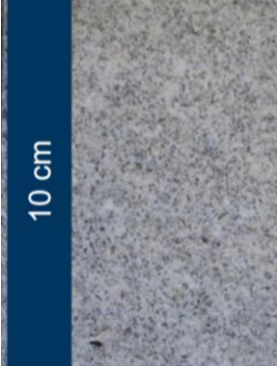



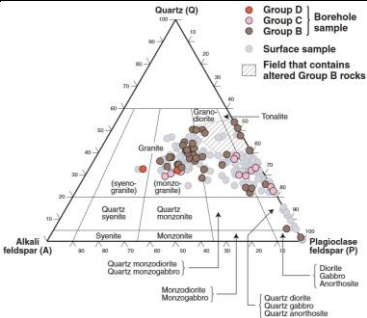
## 1. Sample material and specimen preparation

The sample material should have properties that are first-order similar to Forsmark granite and easily available for other laboratories perform complementary experiments, if required. A web survey was conducted leading to ordering of sample material of

- Padang TG33 (China)
- Padang TG34 (China)
- Padang G603-3 (China), and
- Epprechtstein granite (Germany).

For the sample material a range of initial parameters (grain size, uniaxial compressive strength, porosity, commercial availability, reproducibility, macroscopic isotropy and mineralogical analogy) were determined for selection of the suitable material for this study (Table 1).

Table 1: Parameters determined to select suitable sample material for the study. The Padang granite TG34 was chosen due to its comparable grain size and similar uniaxial compressive strength to Forsmark granite (photo from [73]; modal classification from [79], see Figure 2 for details).

	Forsmark (SWE) [73];[79]	Padang TG33 (CHN)	Padang TG34 (CHN)	Padang G603-3 (CHN)	Epprechtstein (GER)
					
grain size	fine to medium	fine	fine to medium	fine to medium	fine to medium
UCS	200 – 250 MPa	~ 120 MPa	~ 226 MPa	~ 180 MPa	~ 150 MPa
accessible porosity	< 1 %	< 1 – 2 %	< 1 – 2 %	1 %	1 %
mineral. composition		similar to TG34	32 wt-% quartz 23 wt-% orthoclase 40 wt-% plagioclase < 1 wt-% muscovite 5 wt-% biotite	similar to TG34	32 wt-% quartz 35 wt-% orthoclase 25 wt-% plagioclase 5 wt-% muscovite 3 wt-% biotite
		high reproducibility macroscopic isotropy worldwide available	high reproducibility macroscopic isotropy worldwide available	medium reproducibility macroscopic isotropy worldwide available	medium reproducibility macroscopic isotropy local quarry in GER

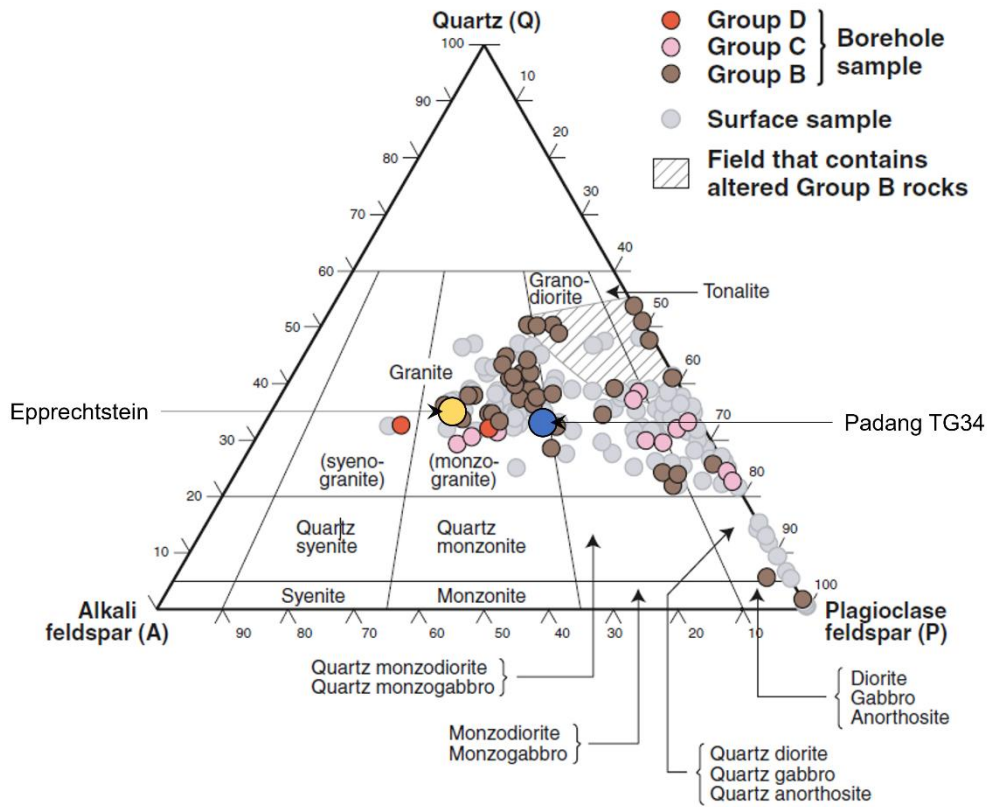


Figure 2: Quartz (Q) – Alkali feldspar (A) – Plagioclase feldspar (P) modal classification of analyzed intrusive rock samples at the Forsmark site. The classification is based on Streckeisen [80]. Groups B, C, and D are distinguished on the basis of their relative age: Group B – 1,886 to 1,865 million years, Group C – 1,864 million years, Group D – 1,852 million years. Figure modified from Stephens et al. [79].

It was decided to proceed with focus on Padang granite TG34; this decision was taken because of its low sample-to-sample variability and its geomechanical properties comparable to those of Forsmark granite.

Padang granite TG34 is medium-grained (grain size 0.5 mm - 4 mm), appears macroscopically isotropic and is composed of quartz (32 wt %), alkali feldspar (23 wt %), plagioclase (40 wt %) and biotite (5 wt %) as identified from X ray powder diffraction analysis, XRD (Table 2).

In addition to experiments on Padang granite TG34 selected experiments were performed on Epprechtstein granite. The results of this experimental programme may be found in [89].

The Padang granite TG34 sample consisted of five blocks with dimensions of approximately a.) length: 100 cm, b.) width: 30 cm c.) high: 10 cm. The specimen naming starts with PG for Padang granite, followed by the number of the block (PG1) and the final number is a specimen counting. X, Y, Z represents the specimen orientation.

For basic rock physical characterisation, determination of thermal properties, uniaxial and triaxial compressive strength tests, and permeability tests, cores of diameter  $D = 40$  mm and length  $L = 80$  mm and an end surface parallelism  $< 0.02$  mm were prepared.



For splitting tensile strength tests, specimens of diameter  $D = 40$  mm and length  $L = 20$  mm were prepared. Drilling, sawing and grinding were done using diamond drill bits and grinding plates with water as cooling fluid. To ensure careful end face preparation of specimens for uniaxial and triaxial compressive strength tests, the grinding procedure was adjusted to a duration of two hours for each end face. Before each test, specimens were oven-dried at 60 °C or saturated with distilled water. All specimens within a sample were drilled in one of three orthogonal directions denoted as X, Y, and Z, which were equivalent for the four sample blocks.

Computer tomographic scans of an intact specimen and specimens loaded uniaxially and triaxially were carried out on specimens both at Fraunhofer IEG, Bochum, Germany and at the Ruhr-University Bochum, Institute of Materials Engineering, Bochum, Germany.

## 2. Basic rock physical characterisation

The rock material was characterised with respect to basic physical and geomechanical properties, i.e., density (grain and bulk density), porosity (accessible, total), thermal properties (thermal conductivity, thermal effusivity, derived heat capacity), intrinsic permeability, mineralogical composition, texture, ultrasonic-velocities and dynamic elastic moduli.

The number of permeability tests was reduced to five because of the very low permeability of investigated specimens, resulting in excessive time effort to perform permeability tests (> 100 h) and the low variability.

### 2.1 Methodology

The geometric **densities** of oven-dried specimens as well as their **porosities** were determined in accordance with DIN EN 1936 [19]. The bulk densities were determined based on the ratio of mass to bulk volume. The accessible porosity was calculated from the ratio of the pore volume derived from water uptake using a desiccator to the total volume of the cylindrical specimen. The grain density was determined using a pycnometer in accordance with DIN EN ISO 17892 [20]. Total porosities were then calculated from the ratio of bulk density of oven-dried specimens to grain density.

Ultrasound **wave velocities** were determined following the updated ISRM Suggested Method for Determining Sound Velocity by Ultrasonic Pulse Transmission Technique [5]. Ultrasound P- and S-wave velocities were determined in axial specimen direction using a standard measurement device (Geotron Elektronik) with S-wave sensors producing a low-amplitude P-wave signal and a high-amplitude S-wave signal. Two identical ultrasound sensors, one serving as source and one as receiver, were pneumatically loaded to the end faces of the specimens with approximately 800 mbar. Rubber sheets (1 mm thickness) were used as coupling medium. The waveform generator generates a rectangular source with a frequency of 350 kHz. Signals were semi-automatically analysed using the software LightHouse UMPC by accounting for system travel time [5].

Thermal properties were determined using C-Therm's Trident system with the Modified Transient Plane Source (MTPS) on cylindrical specimens. The semi-automatic measurement technique applies a current to the sensor's spiral heating element that provides a small amount of heat, typically of 1 to 3 K, which was one-dimensionally transferred into the measured end face of the specimen [3]; [4]. The thermal feedback between specimen and sensor results in an increase in the sensor voltage used to determine the thermal properties in the direction perpendicular to the sensor's surface, i.e., **thermal conductivity**, thermal **effusivity**, and (derived) **heat capacity**. Specimens and sensors were coupled using distilled water. Coupling was improved by a 500 g weight placed on top of the specimen during measurement.

**Permeability** was determined on cylindrical rock specimens placed in a Hoek cell. The rubber sleeve of the Hoek cell was pressed against the lateral surface of the specimen by applying a confining pressure, so that circulation of the axially introduced fluid along the outer specimen surface was prevented. At the specimen's end faces, the fluid up- and downstream (distilled water) was connected to the pore pressure system by loading plates with concentric reliefs. Using Vindum Pump Engineering pumps, the specimens were first saturated to a set pore pressure until fluid uptake stopped. Five different pore pressure gradients of 0.2, 0.4, 0.6, 0.8 and 1 MPa between upstream and downstream were applied to generate steady state flow at an isostatic confining stress state of 5 MPa and a mean pore pressure of 2 MPa resulting in a mean effective stress of 3 MPa.

**Thin sections** with a thickness of 30  $\mu\text{m}$  were prepared for further petrographic analyses. Sample discs were glued to specimen holders before being saw-cut to a thickness of a few 100  $\mu\text{m}$ . Samples were then polished to 25-30  $\mu\text{m}$  and provided with cover glass for protection.

**X-ray** analysis was carried out using pulverised sample material. This ensures that the crystals of the rock-forming minerals were present in random orientations. During the analysis, an X-ray was directed at the sample. If the X-ray hits the periodic arrangement of atoms in the crystal, diffraction occurs, provided that Bragg's condition is fulfilled. A X-ray detector measures the intensity of the diffracted X-rays as a function of the diffraction angle ( $2\theta$ ), resulting in a characteristic diffraction pattern, the so-called diffractogram. The position and intensity of the peaks in the diffractogram were typical of the minerals contained in the rock. By comparing these peaks with reference databases, the various minerals and their relative occurrence in the sample can be identified.

**CT scans** were based on the use of X-rays, which are sent through the rock specimen. The CT scanner rotates around the sample and produces X-ray images (cross-sectional images) of the specimen from different angles. The intensity of the X-rays passing through the rock depends on the density and atomic composition of the material. Areas with higher density absorb more X-rays than less dense areas, and computer algorithms are used to create a three-dimensional reconstruction of the inner structure of the sample from the numerous X-ray images taken during the rotation of the scanner. This 3D volume data can be displayed in the form of cross-sectional images or as a complete 3D model.

**Acoustic Emission (AE)** was used to study the mechanical behaviour of specimens under stress by recording and analysing the sound waves released during these processes. AE relates to the emission of elastic waves generated by cracks, fractures or plastic deformations in the specimen. These sound waves propagate through the specimen and were measured as acoustic emissions. Sensors were attached to the specimen detecting these sound waves. Signals were recorded as time-dependent events (hits) containing characteristic information about size and intensity of the cracks.

## 2.2 Results from basic characterisation

The basic characterisation was performed on specimens prepared for strength testing. Mineralogical composition was determined by nine measurements. Results of density, porosity, ultrasonic velocities and thermal properties are summarised in Table 2; the individual experimental results may be found in Appendix I.

Microstructural analyses of thin sections for three orthogonal orientations and results from CT scans showed that no microstructural anisotropy is evident (Figure 3 , Figure 4). Thin sections show a very low amount of inter- (potentially accessible for fluids) and intraparticle (not accessible) porosity and pre-existing microfractures, in particular within quartz grains.

The permeability was determined on five specimens (Figure 5). The permeability of Padang granite TG34 was less than  $10^{-18} \text{ m}^2$ . With increasing pressure difference between inflow and outflow, the permeability first decreases and then becomes rather constant.

The individual measurements of axial P- and S-wave velocities are shown as a function of the individual measurements of dry density in Figure 6a. The individual measurements of thermal conductivity are plotted as function of total porosity (Figure 6b). A correlation was not observed.

Table 2: Summary of the results of the basic characterisation. For individual experimental results see Appendix. *n* denotes the number of performed tests.

	<b>n</b>		<b>Unit</b>	<b>Average</b>	<b>Standard deviation</b>	<b>Min</b>	<b>Max</b>
mineral. composition	9	quartz	wt-%	32	3	30	38
		alkali feldspar		23	3	20	38
		plagioclase		40	5	33	47
		biotite		5	2	2	8
density	95	bulk	kg/m <sup>3</sup>	2,635	13	2,604	2,664
	18	grain		2,679	2	2,675	2,681
porosity	95	accessible	%	0.8	0.2	0.4	1.1
	95	total		1.7	0.4	0.5	2.8
ultrasonic velocities	95	v <sub>P</sub>	m/s	4,357	255	3,773	4,876
	95	v <sub>S</sub>		2,480	102	2,297	2,721
thermal properties	95	conductivity	W/mK	3.2	0.7	2.5	3.9
	95	effusivity	Ws <sup>1/2</sup> /m <sup>2</sup> K	2,567	142	2,178	2,889
	95	heat capacity	J/kgK	770	17	725	809
permeability	5	ΔP = 0.2 MPa	m <sup>2</sup>	2.6 · 10 <sup>-18</sup>	3.1 · 10 <sup>-19</sup>	2.1 · 10 <sup>-18</sup>	3.0 · 10 <sup>-18</sup>
		ΔP = 0.4 MPa		1.6 · 10 <sup>-18</sup>	2.0 · 10 <sup>-19</sup>	1.2 · 10 <sup>-18</sup>	1.8 · 10 <sup>-18</sup>
		ΔP = 0.6 MPa		1.5 · 10 <sup>-18</sup>	1.4 · 10 <sup>-19</sup>	1.3 · 10 <sup>-18</sup>	1.7 · 10 <sup>-18</sup>
		ΔP = 0.8 MPa		1.5 · 10 <sup>-18</sup>	2.9 · 10 <sup>-19</sup>	1.2 · 10 <sup>-18</sup>	2.0 · 10 <sup>-18</sup>
		ΔP = 1.0 MPa		1.6 · 10 <sup>-18</sup>	2.5 · 10 <sup>-19</sup>	1.2 · 10 <sup>-18</sup>	1.9 · 10 <sup>-18</sup>

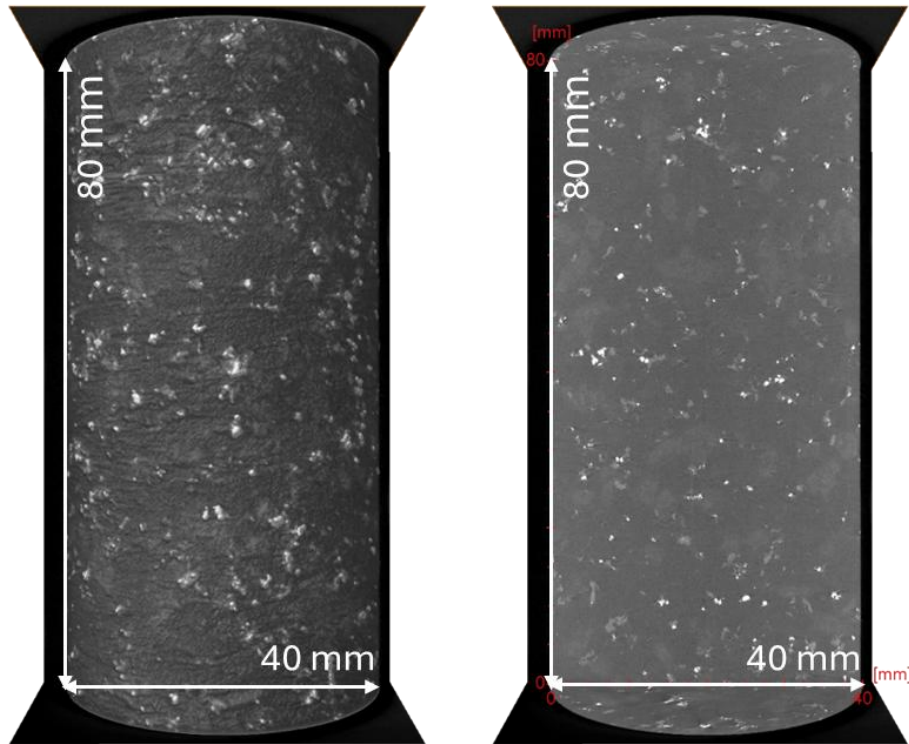


Figure 3: Computertomographic scan (CT-Scan) of specimen PG3-36, drilled in x-direction: 3D view (left) and axial cross section (right). Biotite (white), quartz (dark grey) and feldspar (light grey) can be recognised.





Figure 4: Optical images in cross-polarized light with 1) biotite, 2) quartz and 3) feldspar for different thin section orientations of PG1 (left), PG2 (middle) and for three different specimens tested for tensile strength after failure with loading direction from top to bottom (right). Scale is identical for all images. In thin section PG1, scratch marks are recognisable that were created during the preparation process.

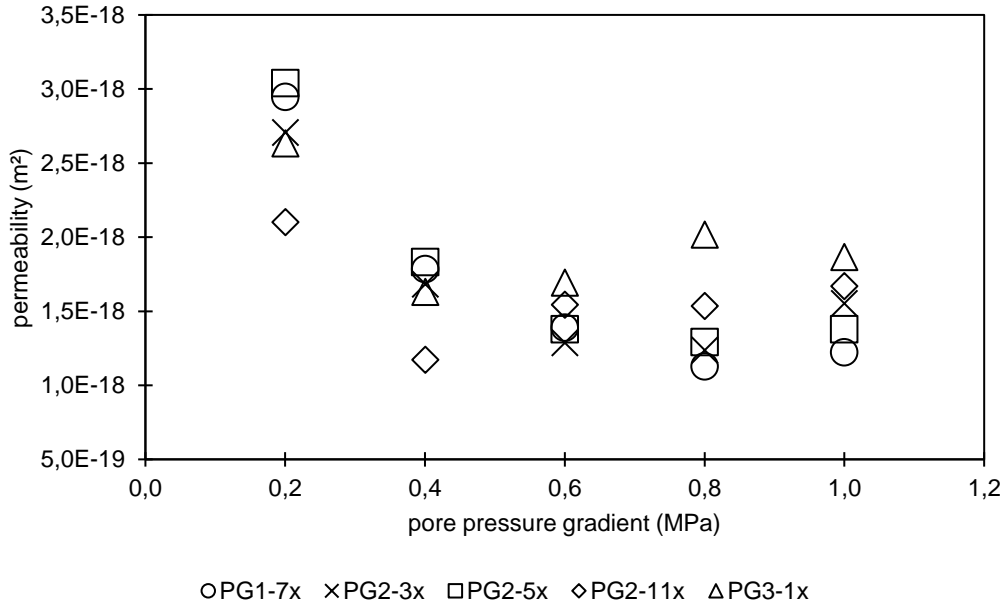


Figure 5: Results of permeability tests at different pore pressure gradients and constant mean effective stresses of 3 MPa. Tests were performed on specimens orientated in x direction of block 1, block 2 and block 3.

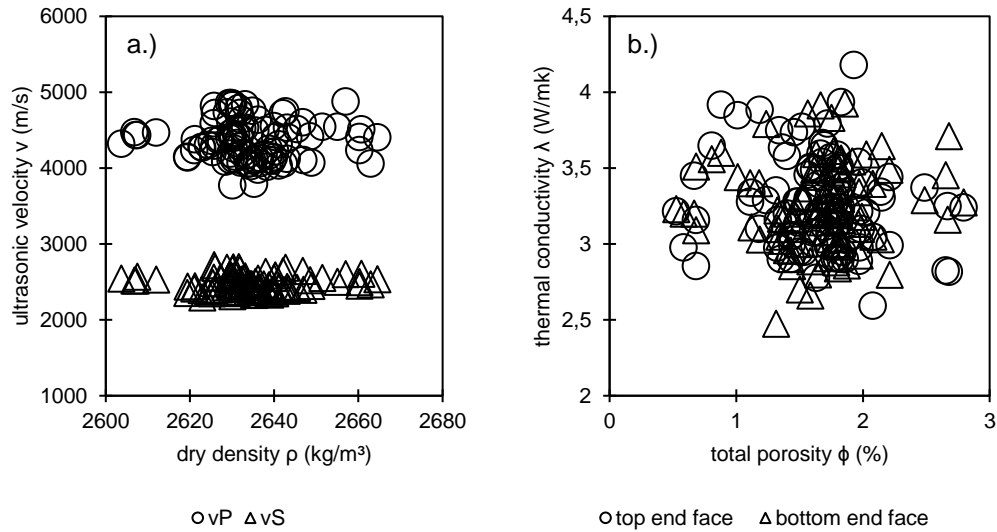


Figure 6. Relations between ultrasound velocities and dry density (a) and thermal conductivity and total porosity (b). Circles represent P-wave velocity, triangles symbolise S-wave velocity (left); circles represent the top end face, triangles symbolise the bottom end face (right).

### 3. Strength testing

The number of scheduled uniaxial compressive strength tests was exceeded due to an investigation of the influence of end face friction on uniaxial compressive strength, required to provide experimental results that can be used as a benchmark for numerical

simulations, which turned out to be particularly important for high-stiffness and high-strength materials such as granite. To evaluate the influence of specimen shape, as well as the strength of the mineral grains in addition to end face friction, 18 uniaxial compressive strength tests with different diameters and length-to-diameter ratios were conducted.

### 3.1 Methodology

For splitting **tensile strength** tests (STS) a rock disc was placed in a steel loading jaw. After centring the specimen an initial load of 200 N was applied. Further strain was applied with displacement rates varying between  $1.5 \cdot 10^{-4}$  and  $1.5 \cdot 10^{-2}$  mm/s until failure occurred. Tensile stress was calculated from load  $F$ , diameter  $D$  and specimen length  $L$  according to [37]; [47]. The splitting tensile strength was determined from the maximum in tensile stress.

To determine the **uniaxial compressive strength** (UCS) and **triaxial compressive strength** (TCS) specimens were placed in a stiff 4 MN loading frame centred between the loading plates, which feature a spherical seat. Experiments were performed without and with a lubricant between loading piston and specimen's end faces to reduce friction. In uniaxial tests, a radial strain chain was placed at the centre of the specimen. In triaxial tests, an isostatic stress state was applied by increasing confining pressure and axial stress simultaneously in a Hoek cell before axial differential stress was increased.

Tests were conducted servo-controlled with grade 1 testing equipment. During testing, axial load was applied until failure occurred. The axial piston advances with a constant velocity resulting in a nominal strain rate ranging between  $1 \cdot 10^{-7}$  and  $1 \cdot 10^{-3} \text{ s}^{-1}$ .

Axial stresses and strains are calculated based on the cross-sectional area of the specimen (disregarding effective contact between piston and specimen) and maximum specimen length, respectively.

UCS and TCS are derived from the maximum in the stress-strain-relation. The deformation modulus  $V$  and the Poisson's ratio  $\nu$  are determined at an axial stress in the range from 40 % to 60 % of UCS [37]; [58]; [69] and [88] using axial strains that are calibrated for system characteristics.

Actual strain rates were calculated from the linear part of the relation between strain and time in the range between 20 % and 80 % of the maximum.

In uniaxial and triaxial compression tests, various lubricants were used to investigate the effect of end face friction on contact surfaces between specimen and loading plates on strength results.

These lubricants were

- Teflon with thickness of 0.5 mm
- Teflon with thickness of 0.025 mm, and
- graphite powder

### 3.2 Results and discussion of strength testing

Tensile and compressive strength of Padang granite TG34 were determined from 267 specimens in total. The number of individual tests including an indication of which lubricant was applied to the load application surface is summarised in Table 3.



Table 3: Number of splitting tensile strength tests (sts), uniaxial compressive strength tests (ucs) and triaxial compressive strength tests (tcs). 267 Padang granite specimens were investigated. ./ denotes that no experiments of that kind were performed.

Test	Unit	Rate	no lubricant	Teflon 0.5 mm	Teflon 0.025 mm	Graphite powder
sts	(mm/s)	$1.5 \cdot 10^{-4}$	22	./	./	./
		$1.5 \cdot 10^{-3}$	26	./	./	./
		$1.5 \cdot 10^{-2}$	22	./	./	./
ucs	(s <sup>-1</sup> )	$1 \cdot 10^{-7}$	./	5	1	4
		$1 \cdot 10^{-6}$	8	4	1	4
		$1 \cdot 10^{-5}$	13	4	1	19
		$1 \cdot 10^{-4}$	6	4	6	9
		$1 \cdot 10^{-3}$	1	4	1	7
tcs	(s <sup>-1</sup> )	$1 \cdot 10^{-7}$	./	./	./	12
		$1 \cdot 10^{-6}$	./	./	./	9
		$1 \cdot 10^{-5}$	4	3	6	25
		$1 \cdot 10^{-4}$	3	./	./	15
		$1 \cdot 10^{-3}$	./	./	./	18

### 3.2.1 Splitting tensile strength tests

Splitting tensile strength of all specimens ranges between  $8.1 \pm 1.3$  MPa and  $12 \pm 1.3$  MPa for all strain rates (Figure 7 and Table 4). There is no significant difference among the blocks or for the different tested directions. In general, splitting tensile tends to increase with increasing rate of displacement, but the significance is low, because the effect of strain rate barely exceeds the reproducibility sample-to-sample variability. The variability is rather high, so that a quantification of the time dependence is challenging. It may be concluded the tensile strength is isotropic.

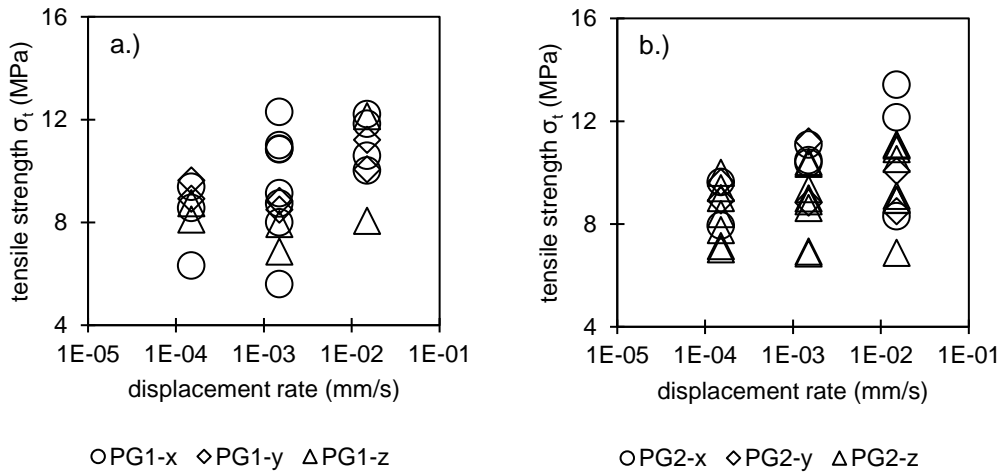


Figure 7: Splitting tensile strength vs displacement rate for block 1 (a) and block 2 (b), no loading point lubricant was used. The letters (x, y, z) indicate the direction of drilling when preparing the specimens.



Table 4: Results of splitting tensile strength tests and standard deviation, no loading point lubricant was used. Specimens were prepared in x-, y-, z-direction from block 1 and block 2.

Specimen (block/orientation)	Displacement rate (mm/s)	Splitting tensile strength (MPa)
PG1-x	$1.5 \cdot 10^{-4}$	$8.1 \pm 1.3$
	$1.5 \cdot 10^{-3}$	$8.8 \pm 2.2$
	$1.5 \cdot 10^{-2}$	$11.2 \pm 0.9$
PG1-y	$1.5 \cdot 10^{-4}$	$9.3 \pm 0.4$
	$1.5 \cdot 10^{-3}$	$8.7 \pm 0.2$
	$1.5 \cdot 10^{-2}$	$10.6 \pm 0.1$
PG1-z	$1.5 \cdot 10^{-4}$	$8.7 \pm 0.1$
	$1.5 \cdot 10^{-3}$	$7.6 \pm 0.6$
	$1.5 \cdot 10^{-2}$	$10.1 \pm 2.0$
PG2-x	$1.5 \cdot 10^{-4}$	$8.7 \pm 1.0$
	$1.5 \cdot 10^{-3}$	$10.4 \pm 0.1$
	$1.5 \cdot 10^{-2}$	$11.2 \pm 1.9$
PG2-y	$1.5 \cdot 10^{-4}$	$12.0 \pm 1.8$
	$1.5 \cdot 10^{-3}$	$11.7 \pm 0.1$
	$1.5 \cdot 10^{-2}$	$9.9 \pm 1.4$
PG2-z	$1.5 \cdot 10^{-4}$	$9.6 \pm 1.4$
	$1.5 \cdot 10^{-3}$	$9.6 \pm 1.4$
	$1.5 \cdot 10^{-2}$	$8.3 \pm 1.1$

### 3.2.2 Uniaxial compressive strength tests

The uniaxial compression strength was investigated for

- different end face friction properties by varying the lubricant,
- different strain rates, and
- different saturation conditions (oven-dried, saturated).

From the campaign focussing on the effect of a lubricant to reduce end friction effects on the compressive strength it was decided to continue further testing using graphite powder as end surface lubricant also for triaxial compression tests.

## EFFECT OF END FACE FRICTION

Uniaxial compressive strength ranged from  $194 \pm 15$  MPa to 258 MPa for strain rates from  $10^{-6} \text{ s}^{-1}$  up to  $10^{-3} \text{ s}^{-1}$ , when no lubricant was used (Table 5). The reproducibility was worse than expected from the good reproducible relation of strength to strain rate. Results from uniaxial compressive strength tests with various lubricants showed that uniaxial compressive strength

- is largest, when graphite is used as lubricant, and lowest for Teflon of thickness 0.5 mm,
- 0.5 mm thick Teflon as lubricant improves reproducibility.

Table 5: Mechanical properties of oven-dried Padang granite TG34 at different strain rates (average and standard deviation, if applicable) for different lubricants placed between specimens and loading plates. The values represent from top to bottom the UCS ( $\sigma_c$ ) in MPa and Young's Modulus (E) in GPa. ./. denotes that no experiments of that kind were performed.

Strain rate / Lubricant		$1 \cdot 10^{-7}$	$1 \cdot 10^{-6}$	$1 \cdot 10^{-5}$	$1 \cdot 10^{-4}$	$1 \cdot 10^{-3}$
		$s^{-1}$				
Graphite powder	$\sigma_c$ (MPa)	$206 \pm 14$	$213 \pm 20$	$225 \pm 17$	$243 \pm 18$	$259 \pm 18$
	E (GPa)	$55 \pm 2$	$53 \pm 1$	$55 \pm 1$	$55 \pm 2$	$56 \pm 1$
Teflon 0.025 mm	$\sigma_c$ (MPa)	174	196	203	$206 \pm 8$	237
	E (GPa)	55	56	49	$56 \pm 1$	57
Teflon 0.5 mm	$\sigma_c$ (MPa)	$137 \pm 3$	$153 \pm 8$	$153 \pm 9$	$182 \pm 12$	$196 \pm 1$
	E (GPa)	$56 \pm 1$	$57 \pm 0$	$57 \pm 3$	$61 \pm 5$	$63 \pm 4$
no lubricant	$\sigma_c$ (MPa)	./.	$194 \pm 15$	$216 \pm 7$	$216 \pm 28$	258
	E (GPa)	./.	$55 \pm 1$	$56 \pm 3$	$55 \pm 3$	56

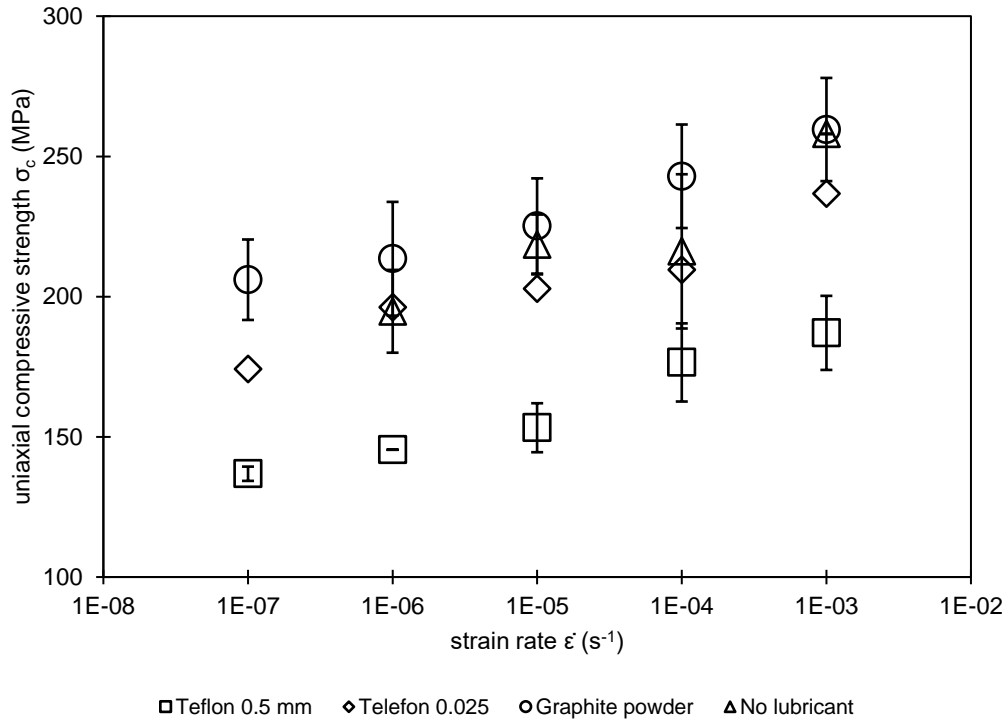


Figure 8: Averaged (if applicable) uniaxial compressive strength vs strain rate for oven-dried specimens, using no lubricant, Teflon of 0.5 mm and 0.025 mm thickness and graphite powder as lubricant. Error bars indicate the standard deviation.

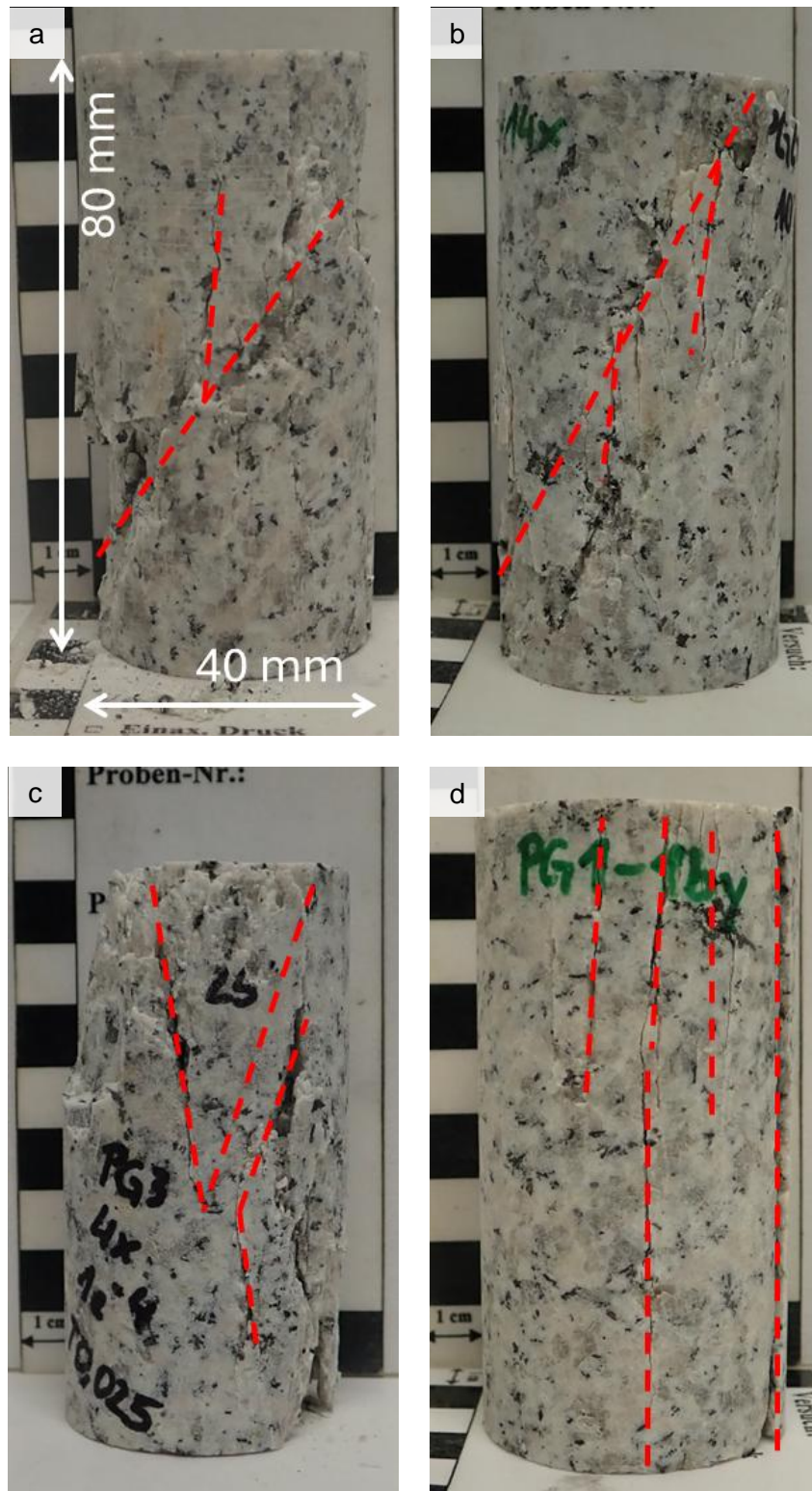


Figure 9: Fracture pattern from uniaxial compressive strength test of specimens where (a) no lubricant, (b) graphite powder, (c) Teflon 0.025 mm and (d) Teflon 0.5 mm was used. The red lines visualise macroscopic fractures. Scale is identical for all images.

lubricant \ strain rate	$10^{-7} \text{ s}^{-1}$	$10^{-6} \text{ s}^{-1}$	$10^{-5} \text{ s}^{-1}$	$10^{-4} \text{ s}^{-1}$	$10^{-3} \text{ s}^{-1}$
Teflon 0.5 mm	80 %	100 %	75 %	75 %	75 %
Teflon 0.025 mm	100 %	100 %	100 %	66 %	100 %
Graphite powder	75 %	100 %	79 %	77 %	71 %
no lubricant	./.	63 %	69 %	67 %	100 %
	axial splitting failure		wedge failure		shear failure

Figure 10: Frequency of fracture patterns of oven-dried specimens in relation of various lubricants and strain rates. ./ denotes that no tests were performed. Light grey to dark grey represents axial splitting, wedge failure and shear failure.

The results (Figure 8) suggest that graphite reduces the friction between piston and specimen, so that the stress distribution within the specimen is more homogeneous and failure is less driven by the stress perturbations near the specimen's end faces. Teflon, however, may penetrate flaws and pore space and, therefore, add a tensile stress contribution to the failure process causing specimens to fail at lower stresses. For Teflon with a thickness of 0.025 mm, it can be assumed that both contributions, the reduction in friction and a tensile stress component, result in a strength that is comparable to that of specimens tested without lubricant.

Specimens tested without lubricant or with graphite powder as a lubricant exhibit lower reproducibility than tests with 0.5 mm thick Teflon. Here the standard deviation was reduced by about half compared to tests with graphite powder or without lubricant. However, the strength decreases significantly in tests where Teflon of thickness 0.5 mm was used as a lubricant.

The post-failure fracture pattern of uniaxially deformed specimens varies depending on the lubricant. Specimens tested with thick and thin Teflon predominantly show axial splitting or wedge failure. Specimens with graphite powder or without lubricant show mainly diagonal shear fractures (Figure 9, Figure 10).

## ANALYSIS OF STRAIN RATE AND SATURATION

To quantify the effect of strain rate and saturation level of the uniaxial compressive strength, further tests were conducted with graphite powder as lubricant applied to the specimens' end surfaces.

The testing campaign was run on bundles of specimens prepared in one lot from one sample block and tested one after the other within subsequent days. This made sure that equipmental and environmental effects were kept to a minimum in one series.

The results are summarised in Figure 11 and Figure 12, highlighting that

- Uniaxial compressive strength (UCS)
  - increases with increasing strain-rate exceeding the standard deviation derived for individual strain rates,
  - decreases with increasing water content,
  - shows specimen-to-specimen variability by about  $\pm 10 \%$ , and
- Young's Modulus shows similar behaviour as UCS.

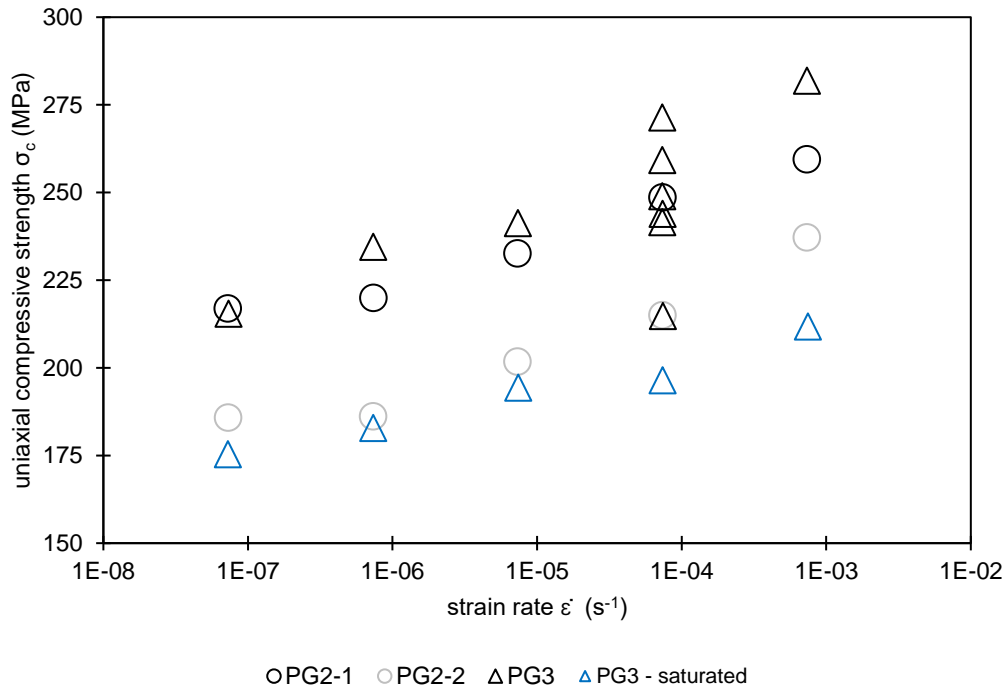


Figure 11: Uniaxial compressive strength vs strain-rate for oven-dried and saturated specimens of Padang granite TG34 drilled in X-direction. Graphite powder was used as lubricant. Each symbol represents one uniaxial compressive strength test. Black circles: series PG2a, grey circles: series PG2b (attention: see discussion in text on validity of results), black triangles: series PG3a, blue triangles: series 3b, fluid saturated.

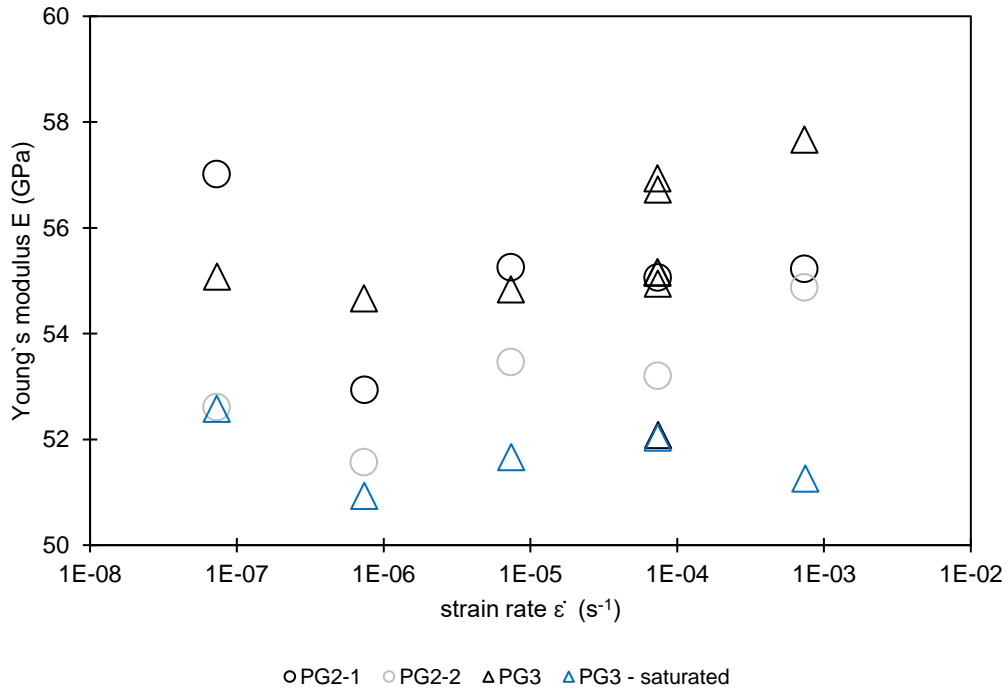


Figure 12: Young's modulus vs strain rate for oven-dried and saturated specimens of Padang granite TG34 drilled in X-direction. Graphite powder was used as lubricant. Each symbol represents one uniaxial compressive strength test. Black circles: series PG2a, grey circles: series PG2b (attention: see discussion in text on validity of results), black triangles: series PG3a, blue triangles: series 3b, fluid saturated.

Young's moduli of specimen with graphite powder as lubricant seem to exhibit a slight tendency to increase with increasing strain rate of  $1 \cdot 10^{-6} \text{ s}^{-1}$  and larger (Figure 12). However, the overall range in Young's moduli was narrow with values between 51 GPa and 58 GPa.

The compressive strength obtained from series PG2-2 is pronounced and consistently lower than the results from series PG2-1 (both oven-dried). The locations of the specimens within the block PG2 showed no preferred distribution for both series; local variability within the block can therefore not explain the systematic reduction in strength for series PG2-2.

The drilling of the cores for preparation of the specimens were done in one go for both series, hence drilling can be assumed to not be the cause for the systematic change of strength.

However, end surface grinding was done by different operators at different times. Therefore, one may suspect that the end surface preparation caused the pronounced and systematic change of UCS. As the testing series PG3, which was run later and showed results comparable to series PG2-1, the series PG2-2 may be considered invalid. Koehlen et al. [43] showed the influence of specimen end surface preparation on the results of strength testing. For this reason, the series PG2-2 is flagged as 'to be used with caution'.

The saturated specimens showed a significantly lower strength than the oven-dried specimens. This is true, especially for specimens tested at low relative strain rates, because due to the long test duration. But even specimens that were tested at high strain rates could be affected by air humidity, especially due to high weather humidity or no air ventilation. Here, the water has an influence on the strength, as the cohesive forces between the mineral grains and in the crystal structure were reduced. Furthermore, the humidity can act as a kind of lubricant and thus reduce the internal friction and strength. Furthermore, pore pressure increases slightly due to humidity which also reduces the strength.

## ANALYSIS OF LENGTH-TO-DIAMETER RATIO

As presented in Figure 13 and Table 6, uniaxial compressive strength tests with length-to-diameter ratios of 2:1, 2.5:1 and 3:1 at diameters of 15, 20, 25, 30 and 50 mm show no clear dependence on the length-to-diameter ratio, which is contrary to what has been published by [39]; [45]; [56]; [57]; [62]; [64]; [66]; [83] and [84], reporting a decrease in uniaxial compressive strength with increasing length-to-diameter ratio.

Furthermore, the results of the tests with different diameters (Figure 13 and Table 6), show that specimens with a diameter of 50 mm have the highest strength. The trend, that strength decreases with increasing diameter as reported by Hoek and Brown [35], cannot be confirmed for Padang granite TG34. However, the specimens of diameter 15 mm is violating the ISRM recommendation that the specimen diameter shall be ten times the largest grain size, which was 4 mm. [37].

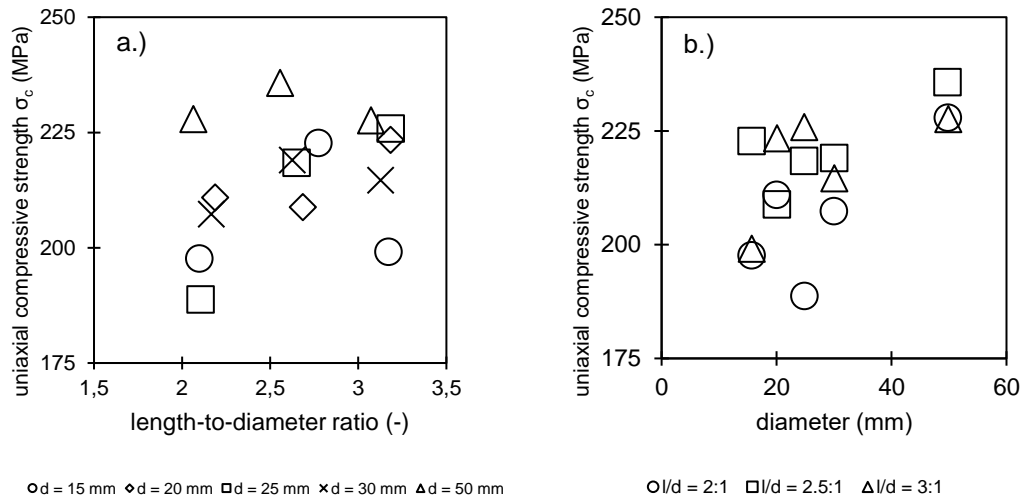


Figure 13: Results of oven-dried uniaxial compressive strength tests with (a) different length to diameter ratios and different diameters (b) at a strain rate of  $1 \cdot 10^{-5} \text{ s}^{-1}$ . Graphite powder was used as lubricant, the specimens were in y-direction orientated.

Table 6: Results of 18 uniaxial compressive strength tests with different length-to-diameter ratios. Graphite powder was used as lubricant, the specimens were in y-direction orientated.

Diameter (mm)	Strain rate ( $\text{s}^{-1}$ )	Length-to-diameter ratio (-)	$\sigma_c$ (MPa)
15	$1 \cdot 10^{-5}$	2.1	198
		2.8	223
		3.2	199
20	$1 \cdot 10^{-5}$	2.2	211
		2.7	209
		3.2	223
25	$1 \cdot 10^{-5}$	2.1	189
		2.6	218
		3.2	226
30	$1 \cdot 10^{-5}$	2.2	207
		2.6	219
		3.1	215
50	$1 \cdot 10^{-5}$	2.1	228
		2.6	236
		3.1	228

### 3.2.3 Triaxial compressive strength tests

Two kinds of experiments were performed: (a) conventional triaxial compression experiments and subsequently on the same specimen (b) shear failure experiments of pre-existing discontinuities. The experiments include a variation of confining stress, a pore pressure of 6 MPa, as well as various strain rates.

#### EFFECT OF STRAIN-RATE AND SATURATION

Triaxial deformation experiments at various strain rates for single stage triaxial compressive strength tests on specimens using graphite powder as lubricant were performed. The specimens were

- oven-dried before the experiment, or
- oven-dried before assembling and saturated after assembling, or
- saturated to constant mass before assembling and further saturated after assembling.

As shown in Figure 14, a dependence of the triaxial compressive strength on strain rate was observed. Triaxial compressive strength increases with increasing deformation rate in line with the results for uniaxial compressive strength.

A pore pressure of 6 MPa has a significant influence on triaxial compressive strength at different strain rates. Both types of specimens deformed at elevated pore pressures show a more pronounced sensitivity to strain rate than dry samples, with specimens saturated prior to assembling being slightly weaker than specimens saturated after assembling. Following observations by Duda & Renner [21], two mechanisms are responsible for the apparent increased sensitivity to strain rate for saturated specimens: 1) Physico-chemical interactions between the pore fluid and solid constituents cause weakening, probably due to stress corrosion at crack tips. 2) Insufficient drainage at higher strain rates causes pore pressure to locally drop, when cracks grow and propagate, and limited communication with the pore pressure reservoir cannot counteract the increasing pore volume to maintain pore pressure. Therefore, effective stress locally increases leading to dilatancy hardening, i.e., an apparent increase in strength caused by an increase in effective confining pressure. As a consequence, strength increases more significantly with increasing strain rate due to an increasing contribution from insufficient drainage at crack tips. Accordingly, the amount of observed weakening is largest at low strain rates, where maximum drainage can be maintained among the set of experiments at different strain rates. Additionally, weakening due to fluids appears to be time-dependent, because longer saturation durations seem to further weaken the specimens.

It remains unclear, whether drainage is fully maintained during the slowest experiments at the lowest strain rate. The critical strain rate above which drainage is lost is a function of hydraulic diffusivity, critical Deborah number, strain at failure and characteristic length scale of hydraulic transport processes. The weakening effect may therefore exceed the observed amount at even lower strain rates.



Table 7: Results of individual triaxial compressive strength tests with pore pressure of 6 MPa at different effective confining pressure. The specimens were saturated during TCS test and saturated to constant mass before assembling.

Test condition	$\sigma_{3\text{eff}}$ (MPa)	Strain rate ( $\text{s}^{-1}$ )	$\sigma_1$ (MPa)
Saturated during TCS test	3	$1 \cdot 10^{-7}$	103
		$1 \cdot 10^{-5}$	205
		$1 \cdot 10^{-3}$	304
	5	$1 \cdot 10^{-7}$	130
		$1 \cdot 10^{-5}$	225
		$1 \cdot 10^{-3}$	306
	9	$1 \cdot 10^{-7}$	219
		$1 \cdot 10^{-5}$	277
		$1 \cdot 10^{-3}$	340
Saturated before assembling	3	$1 \cdot 10^{-7}$	87
		$1 \cdot 10^{-5}$	130
		$1 \cdot 10^{-3}$	211
	5	$1 \cdot 10^{-7}$	122
		$1 \cdot 10^{-5}$	150
		$1 \cdot 10^{-3}$	247
	9	$1 \cdot 10^{-7}$	188
		$1 \cdot 10^{-5}$	217
		$1 \cdot 10^{-3}$	296

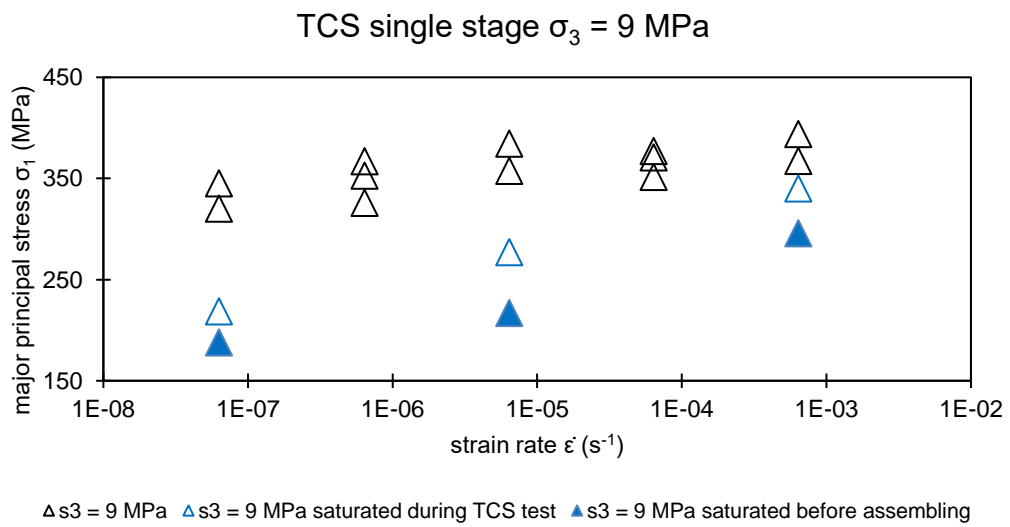
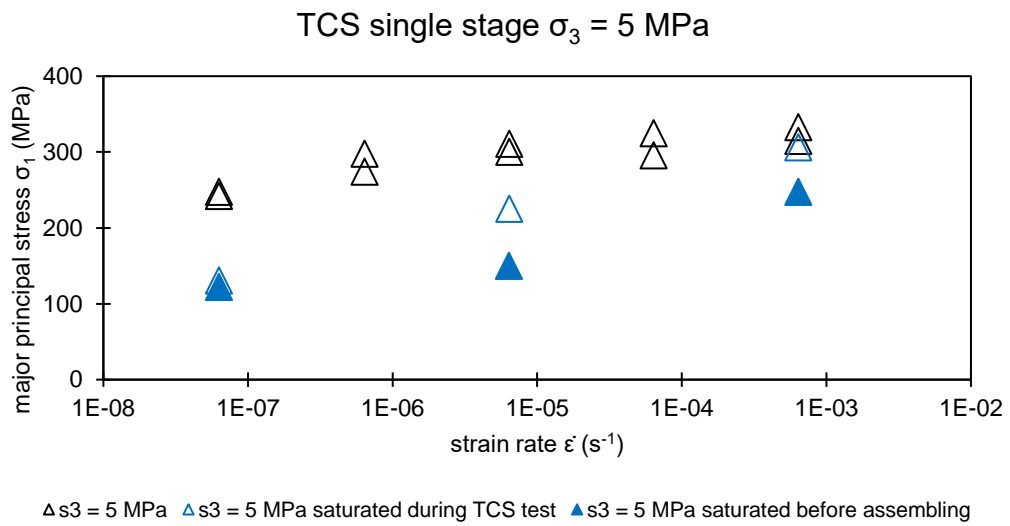
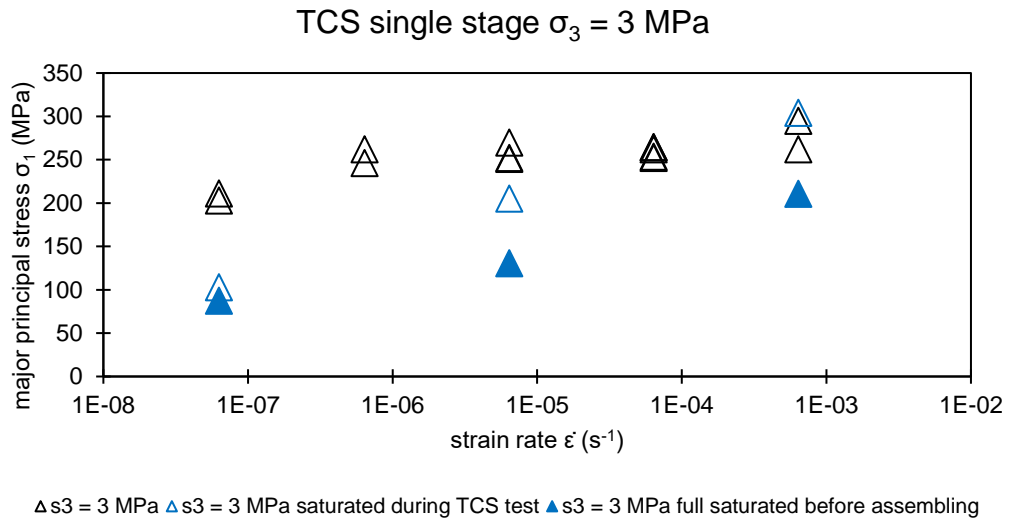


Figure 14: Triaxial compressive strengths vs strain rate for specimens being oven-dried, saturated during the TCS test and saturated to constant mass before assembling at 3, 5 and 9 MPa confining pressure using graphite powder as lubricant.

## ANALYSIS OF MOHR-COULOMB FAILURE CRITERION

The Mohr-Coulomb failure criterion was determined for experiments at all strain rates and at 3, 5, and 9 MPa confining pressure on oven-dried specimens. For saturated specimens only strain rates of  $1 \cdot 10^{-7} \text{ s}^{-1}$ ,  $1 \cdot 10^{-5} \text{ s}^{-1}$  and  $1 \cdot 10^{-3} \text{ s}^{-1}$  were used.

Cohesion and angle of internal friction of oven-dried specimens were quite constant and showed no dependence on the strain rate.

The water in the saturated specimens had an influence on the cohesion and the angle of internal friction. With increasing strain rate, the angle of internal friction apparently decreases and the cohesion increases (Table 8 and Figure 15), potentially also a superposition of physico-chemical interactions and drainage effects.

Table 8: Friction criteria after Mohr-Coulomb derived from single stage triaxial compressive strength tests of oven-dried specimens at different strain rates using graphite powder as lubricant. ./ denotes that no tests were performed.

Strain rate ( $\text{s}^{-1}$ )	Angle of internal friction ( $^{\circ}$ )		Cohesion (MPa)	
	oven-dry	saturated before assembling	oven-dry	saturated before assembling
$1 \cdot 10^{-7}$	62	64	22	5
$1 \cdot 10^{-6}$	60	./	30	./
$1 \cdot 10^{-5}$	63	60	27	17
$1 \cdot 10^{-4}$	64	./	26	./
$1 \cdot 10^{-3}$	62	55	29	36

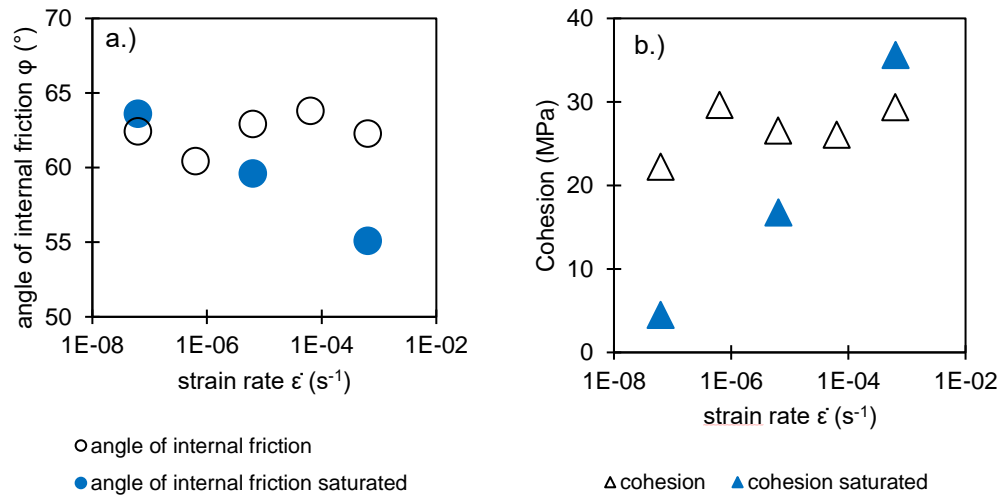


Figure 15: Angle of internal friction (a) and cohesion (b) vs strain rate for oven-dried specimens tested by 3, 5 and 9 MPa confining pressure.

## ANALYSIS OF SHEAR FAILURE EXPERIMENTS

Shear failure experiments were performed on specimens tested in single stage triaxial deformation experiments by continuing shear along the created fracture. The angle of inclination of the resulting fracture was measured and normal and shear stress were calculated to derive the friction criteria. The fracture angle of incidence, presented in Figure 16, varied between 64° and 77° and showed no dependence on deformation rate.

Friction angle is decreasing with increasing deformation rate (Table 9 and Figure 17). At a slow strain rate, interlocking of the fracture surfaces was high, resulting in a higher friction angle. The optically determined roughness of the fracture surface was reduced at higher strain rates, causing the friction angle to decrease.

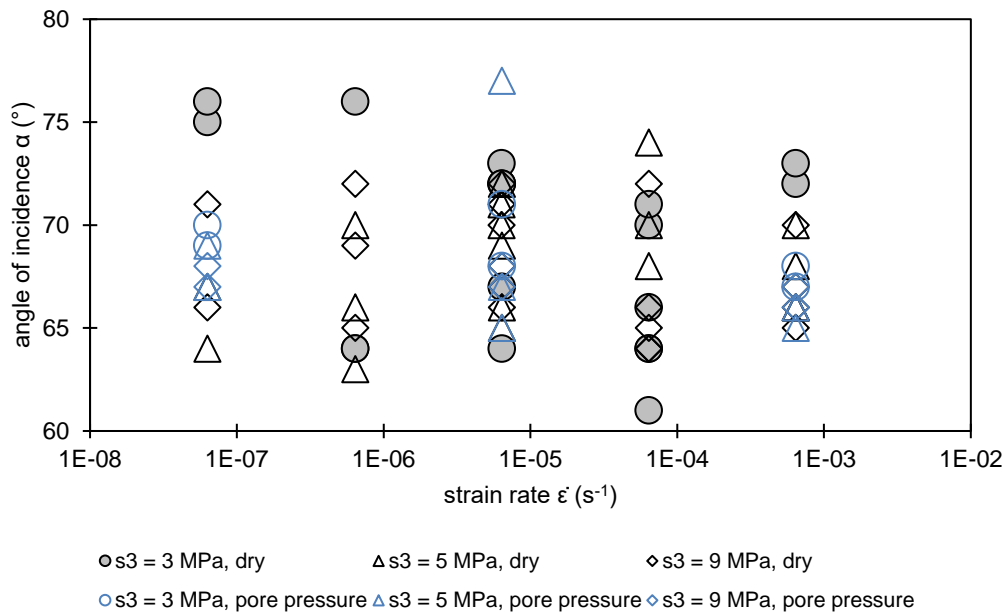


Figure 16: Fracture angle of incidence vs nominal strain rate for specimens being oven-dried and saturated to constant mass tested by 3, 5 and 9 MPa confining pressure using graphite powder as lubricant.

Table 9: Results of shear failure experiments derived from single stage triaxial compressive strength tests of oven-dried and saturated to constant mass specimens at different strain rates using various lubricants.

Lubricant	Condition	Strain rate (s <sup>-1</sup> )	Fracture friction angle (°)
Graphite powder	oven-dried	$1 \cdot 10^{-7}$	56
		$1 \cdot 10^{-6}$	57
		$1 \cdot 10^{-5}$	54
		$1 \cdot 10^{-4}$	29
		$1 \cdot 10^{-3}$	44
	pore pressure	$1 \cdot 10^{-7}$	51
Teflon 0.5 mm	oven-dried	$1 \cdot 10^{-5}$	48
		$1 \cdot 10^{-5}$	52
		$1 \cdot 10^{-5}$	27

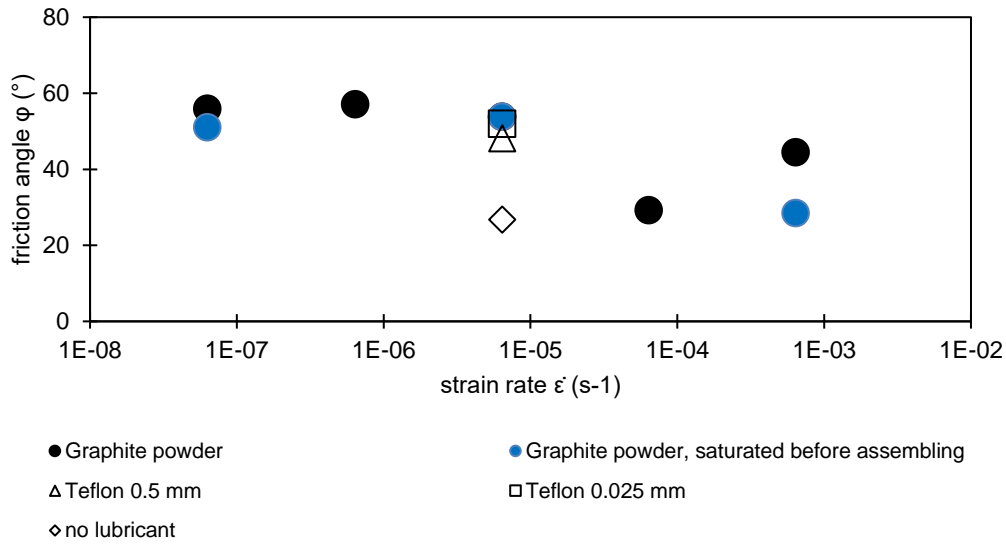


Figure 17: Friction angle vs strain rate for specimens being oven-dried and saturated to constant mass tested by 3, 5 and 9 MPa confining pressure using graphite powder, 0.5 mm – 0.25 mm thick Teflon and no lubricant.

In order to quantify the influence of different lubricants on the triaxial compressive strength, tests were carried out at confining pressures of 3, 5 and 9 MPa at a relative strain rate of  $1 \cdot 10^{-5} \text{ s}^{-1}$ .

The results of triaxial compressive strength tests with lubricant as shown in Figure 18, did not reflect the results of the uniaxial compression tests. The highest strength was observed for specimens where no lubricant was used, followed by samples with graphite powder on end faces, which is reverse to the result of the uniaxial compressive strength tests. The strength was the lowest for all confining pressures using Teflon of 0.5 mm thickness as a lubricant.

As with the uniaxial compression tests, the lubricants also have an influence on the fracture pattern. When using 0.5 mm or 0.025 mm thin Teflon, there was predominantly failure due to axial splitting or wedge formation. If graphite powder was used as lubricant or the lubricant was dispensed, diagonal shear failure dominates as shown in Figure 19.

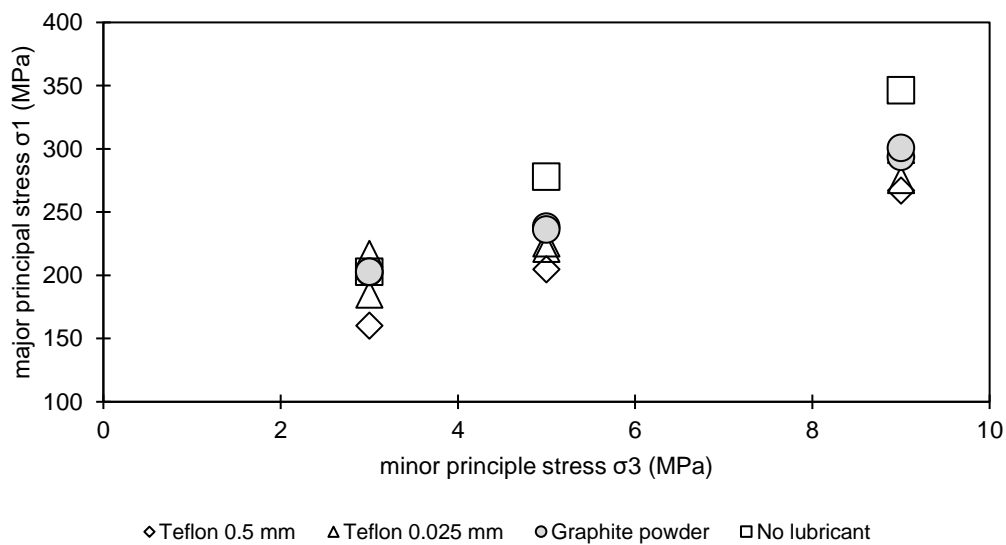


Figure 18: Results of triaxial compressive strength for oven-dried specimens at a nominal strain rate of  $10^{-5} \text{ s}^{-1}$  using different lubricants. Each symbol represents one experiment.

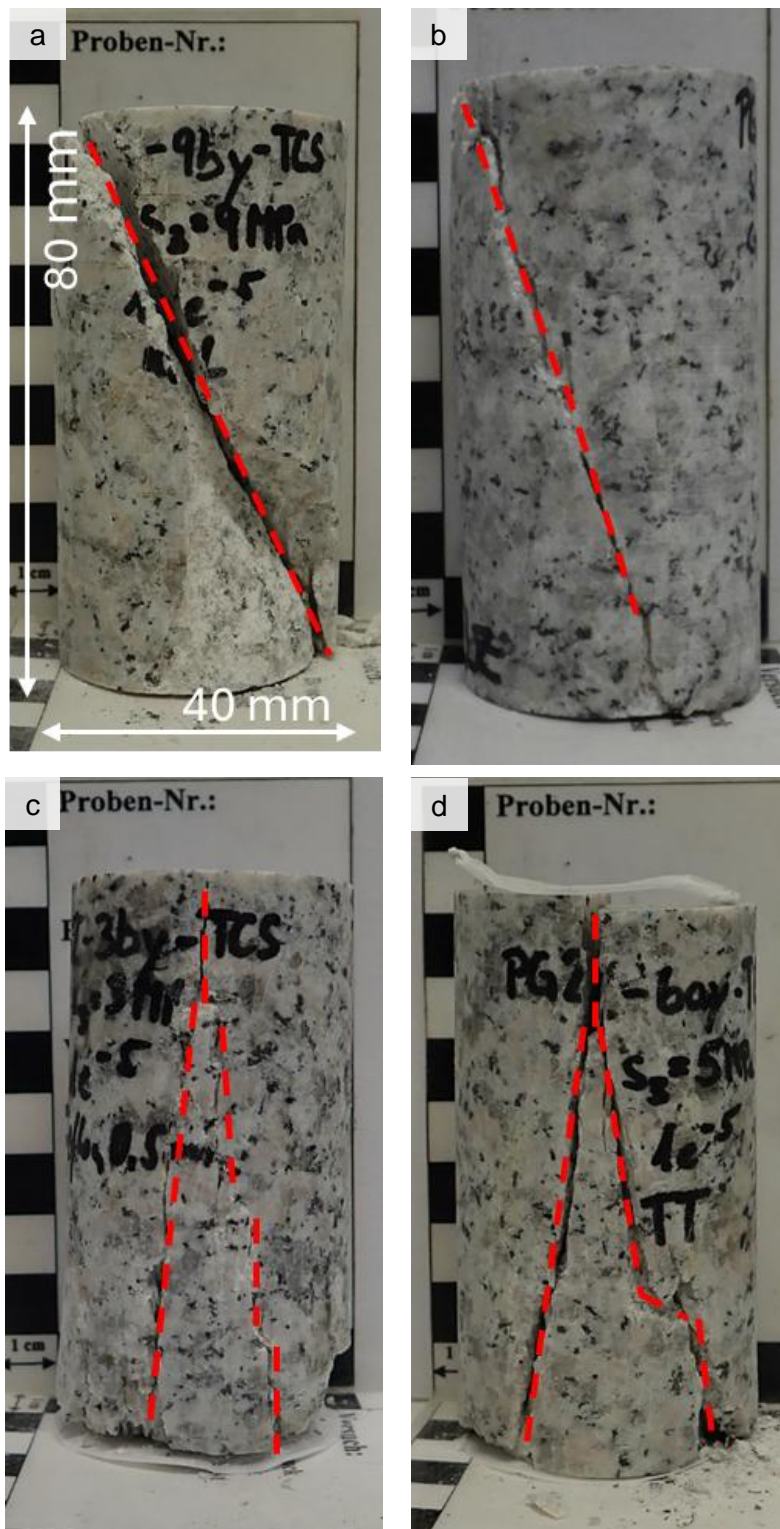


Figure 19: Fracture pattern from triaxial compressive strength test of specimens where (a) no lubricant, (b) graphite powder, (c) Teflon 0.025 mm and (d) Teflon 0.5 mm was used. The red lines visualise macroscopic fractures. Scale is identical for all images.

### 3.2.4 Micromechanics

#### COMPUTER TOMOGRAPHIC SCANS (CT-SCANS)

**CT-scans** were performed on both uniaxial and triaxial compressive strength tests loaded at a relative strain rate of  $1 \cdot 10^{-4} \text{ s}^{-1}$ . Graphite powder was used as a lubricant in each case. The confining pressure of this triaxial compressive strength test was 5 MPa.

As shown in Figure 20, both specimens were dominated by shear failure, which can be recognised macroscopically by a diagonal fracture. The fracture from uniaxial compressive strength test is partially open by around 1 mm and crosses the entire specimen from bottom left to top right. A slightly smaller and less open fracture starts from the main fracture at an angle of approximately  $60^\circ$ . On the right-hand side of the specimen, signs axial splitting can be detected due to a large number of isolated small fractures.

In the triaxial compression test, the primary, diagonal fracture is only slightly open and ends in the specimen. As in the uniaxial compressive strength test, a secondary fracture also occurs here at an angle of approximately  $60^\circ$ . Axial splitting is partially noticeable in the lower left and upper right sections.

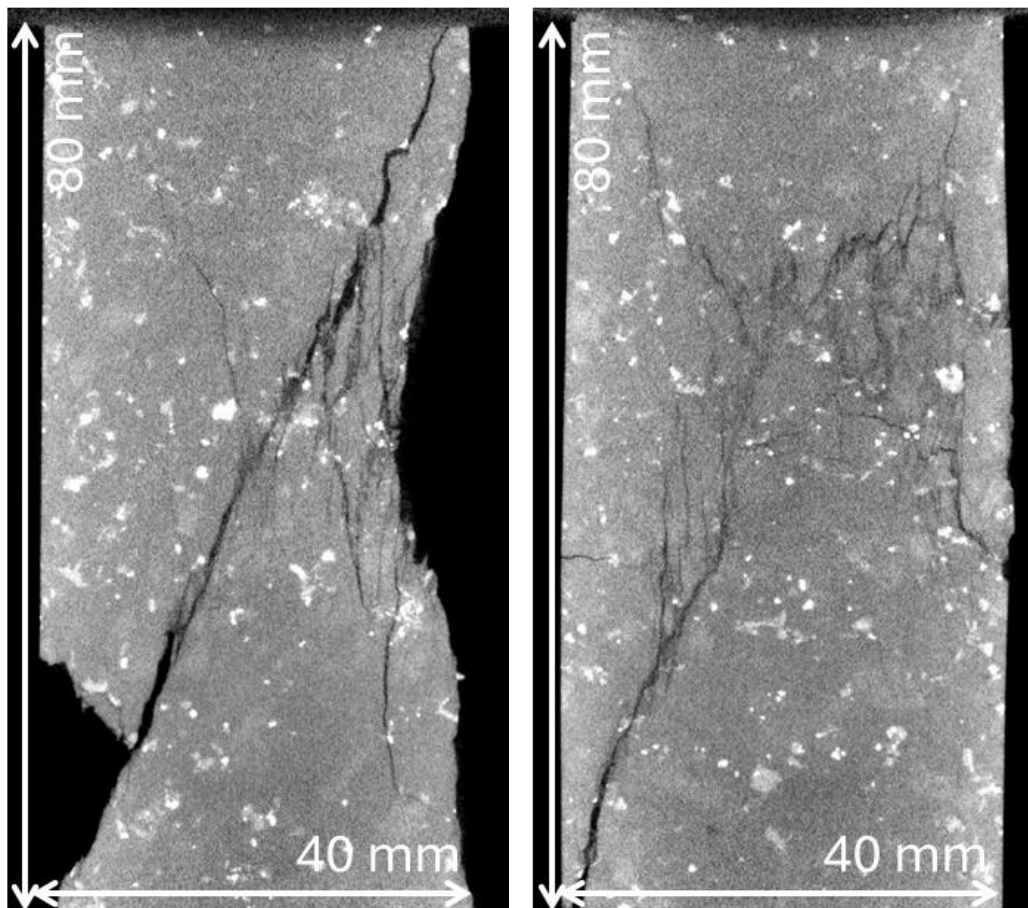


Figure 20: Computertomographic scans (CT-Scan) of oven-dried specimens after uniaxial (left) and triaxial (right) compressive strength test at a strain rate of  $10^{-4} \text{ s}^{-1}$  and 5 MPa confining pressure. Biotite (white), quartz (light grey) and feldspar (dark grey) can be recognised.

## SUBCRITICAL CRACK GROWTH

**Subcritical crack growth** index was calculated from the relation between uniaxial compressive strength  $\Delta\sigma_{\max}$  and strain rate  $\dot{\epsilon}$  following a power-law relation based on a combination of subcritical crack growth and the sliding wing crack model [40]; [59], according to

$$\Delta\sigma_{\max} \propto \dot{\epsilon}^{\frac{1}{n+1}} \quad (1)$$

where  $n$  denotes the subcritical crack growth index (e.g. [42]). Subcritical crack growth indices were 38 for oven-dried samples deformed with graphite powder, and 50 for saturated samples (Table 10). Teflon and using no lubricant reduced the subcritical crack growth index to lower values. In principle, the index can be used to describe the pseudo-viscous behaviour of rocks at temperatures below 200 °C and to upscale strength properties to quasi-static time scales.

Table 10: Subcritical crack growth index for Padang granite TG34.

Lubricant	Subcritical crack growth index $n$
Graphite powder UCS	38
Graphite powder UCS saturated	50
Graphite powder TCS 3 MPa confining pressure	36
Teflon 0.025 mm	31
Teflon 0.5 mm	27
no lubricant	27

### 3.2.5 Acoustic Emission (AE) analysis

**Acoustic emission** (AE) were measured on three oven-dried Padang granite TG34 specimens during triaxial compressive strength tests. The specimens were tested at 9 MPa confining pressure and a nominal strain rate of  $10^{-7} \text{ s}^{-1}$ ,  $10^{-5} \text{ s}^{-1}$ , and  $10^{-3} \text{ s}^{-1}$ , respectively. During the tests, the axial load, acoustic emissions with a duration of less or more than 100  $\mu\text{s}$ , the cumulative hits of the events and the test duration were measured (Figure 21). The duration of the test was approximately 1700 minutes at the slow rate, 25 minutes at the medium rate, and 0.3 minutes at the high deformation rate. During the tests, around 120,000 cumulative AE-events were recorded for the low strain rate, and 20,000 hits for the high strain rate. At the medium strain rate, approximately 42,000 hits were recorded (Figure 22).

With increasing strain rate, the number of total AE-events decreases. While part of the decreasing amount of recorded AE events with increasing strain rate is likely related to an overlay of individual fracture events at high strain rates making it harder for the automatic software to detect single events, the observation is in principle in line with the idea that at low strain rates, microcracks are allowed to grow subcritically, gradually weakening the specimen. In contrast, at high strain rate, test duration is short, and the amount of time at a specific stress level above a critical stress allowing subcritical crack growth is lower, resulting in less crack growth and higher strength (Figure 23). However,



the amount of AE events does not exceed 10 000 prior to failure for all strain rates, and a significant difference between the AE recordings is observed in particular during failure, with low strain rates adding the largest amount of AE events during a two-step macroscopic fracture process, which is in line with the observation that interlocking is more pronounced at low strain rates.

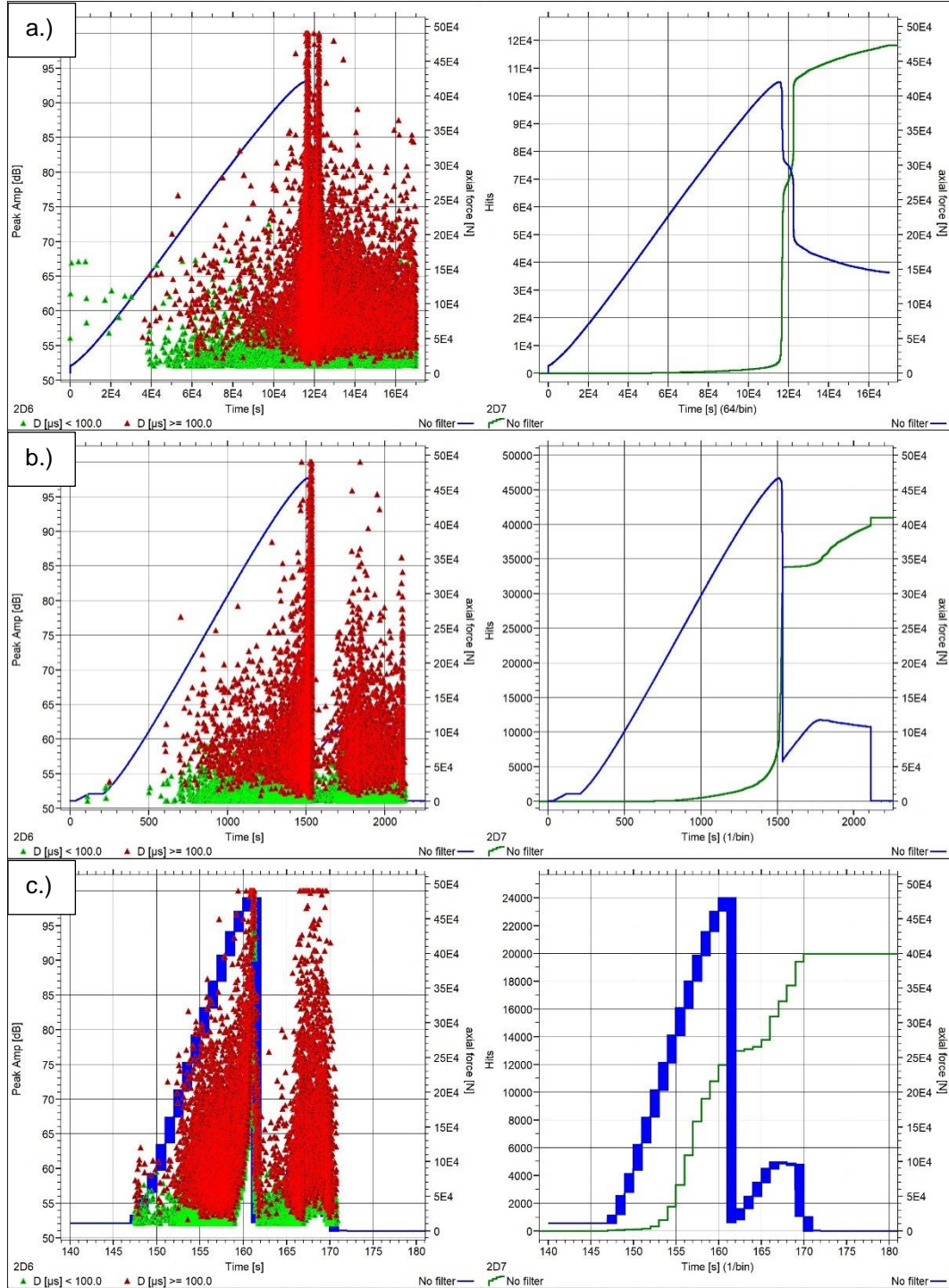


Figure 21: AE records of oven-dried Padang granite TG34 specimens at 9 MPa confining pressure and at a strain rate of (a)  $1 \cdot 10^{-7} \text{ s}^{-1}$ , (b)  $1 \cdot 10^{-5} \text{ s}^{-1}$ , and (c)  $1 \cdot 10^{-3} \text{ s}^{-1}$ . Blue indicates axial load, green and red triangles represent AE-events shorter and longer than 100  $\mu\text{s}$ , the green line illustrates the cumulative number of hits.

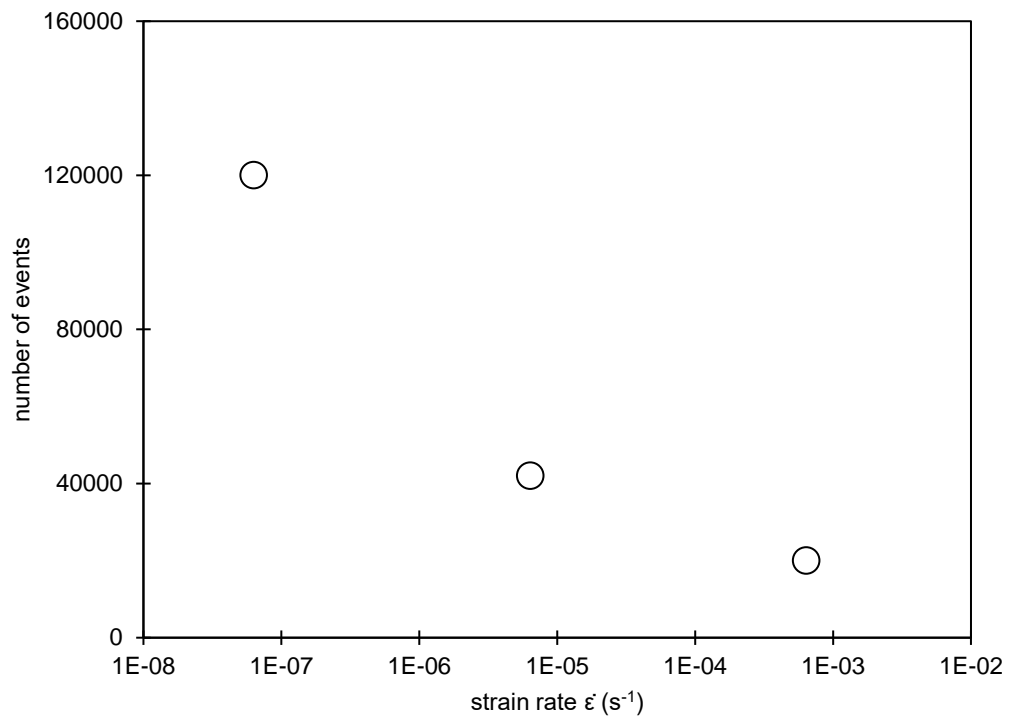


Figure 22: Number of AE-events vs strain rate for oven-dried specimens tested under triaxial compression at 9 MPa confining pressure. AE-events louder than 52 dB were measured only.

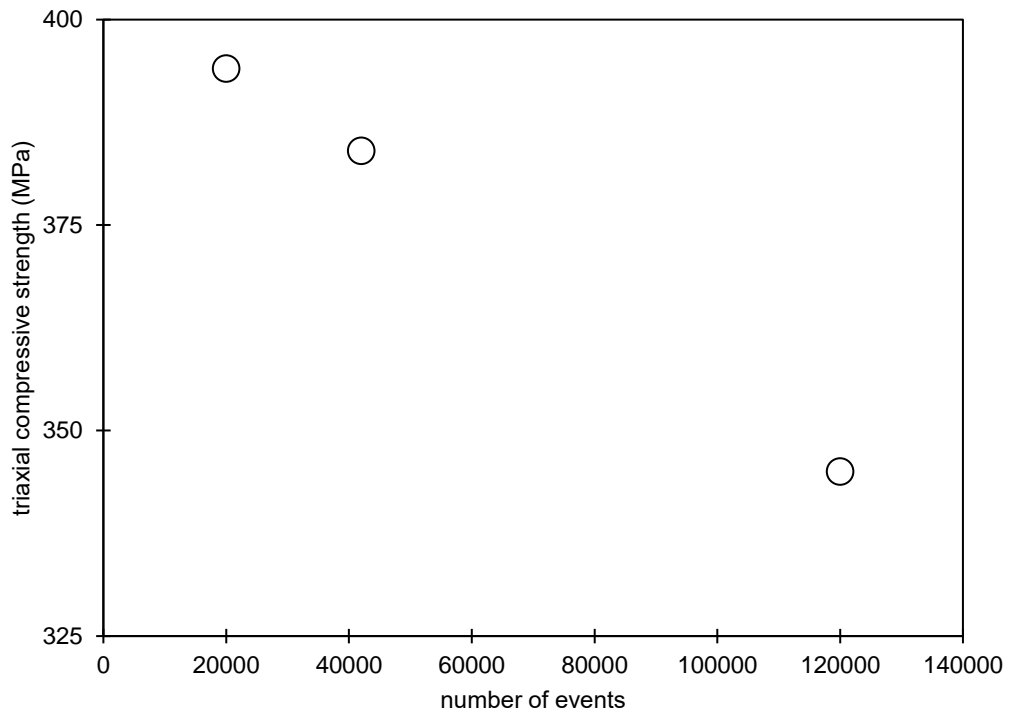


Figure 23: Triaxial compressive strength vs number of AE-events for oven-dried specimens tested under triaxial compression at 9 MPa confining pressure. AE-events louder than 52 dB were measured only.

# Numerical Simulations

## 1. Fundamental modelling principles of crystalline rock failure

Two types of numerical methods are available for analysis of intact rock mechanical behaviour: continuum and discontinuum methods [68]. An important difference between these two types of methods is how the damage (degradation and failure) process is represented, indirectly or directly [65]. The continuum methods use average measures of material degradation in constitutive relations to represent micro-structural damage, while the discontinuum methods idealise the material as a collection of separate units such as particles bonded together at their contact points and use the breakage of the bonds to represent damage [65]. Crystalline rocks typically contain randomly oriented grains, grain boundaries and defects in form of microcracks. The mathematical principles of two methods (crack phase field damage and Voronoi grain base) to simulate failure in crystalline rock such as granite are described in the following. The simulation was realized with 1) the crack phase field damage method by COMSOL Multiphysics software and 2) with the Voronoi grain-based method by RS2 software.

### 1.1 Numerical approach 1: Crack phase field damage model (CPFDM)

The microcracks propagate when the rock is loaded beyond a certain threshold. As illustrated in Figure 24, the development of cracking or damage is characterised by several thresholds, typically crack closure ( $\sigma_{cc}$ ), crack initiation ( $\sigma_{ci}$ ), and crack damage ( $\sigma_{cd}$ ). The crack closure threshold ( $\sigma_{cc}$ ) refers to the stress at which pre-existing microcracks in the material are closed due to the compression of the sample. This threshold is identified when the stress-strain curve becomes linear. After crack closure, the material behaves elastically until the onset of dilation caused by the formation of new microcracks.

The crack initiation threshold ( $\sigma_{ci}$ ) is considered as the beginning of inelastic deformation (dilation) following the linear-elastic loading phase. The cracking that begins at this stage of loading is considered stable, as an increase in load is required to induce further dilation and cracking in the sample.

Existing cracks start to propagate, and new cracks form stably when the damage initiation threshold is exceeded. However, critical rock mass damage only occurs when the crack density is sufficient for cracks to merge into shear bands or tensile fractures causing localisation.

When the total volumetric strain starts to indicate bulk volumetric growth, the stress is referred to as the crack damage threshold ( $\sigma_{cd}$ ) assuming that the transition from compaction to dilation is caused by the opening and merging of microcracks in the sample, making the damage development unstable [9]; [10]; [22]; [23]; [49]; [50] and [61].

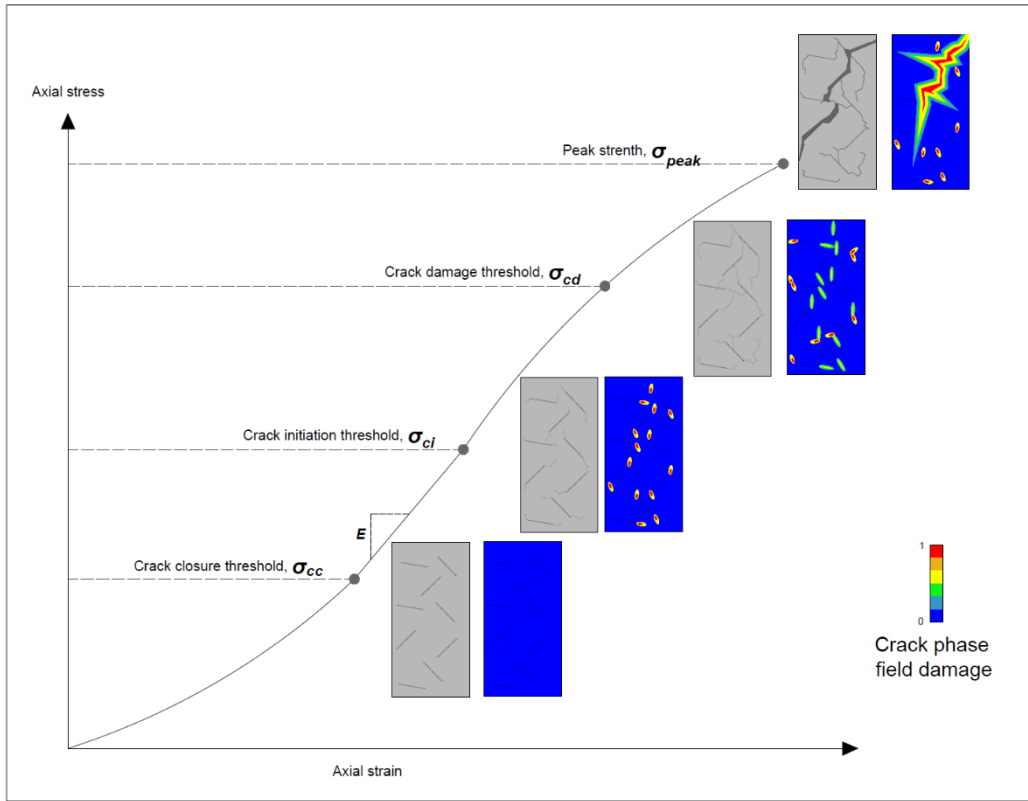


Figure 24: Stages of crack development in rock during uniaxial compressive test and its representation in the mechanic and phase field model.

The crack initiation mechanism can be examined using three main criteria for solids with microcracks: stress-based criteria [24], energy-based criteria [76], and strain-based criteria [78].

The first criterion for crack initiation was proposed by Griffith [30] stating that tensile (mode-I) fractures occur when the energy stored in the rock exceeds the surface energy of the rock material at crack tips. Since its publication, the Griffith criterion has been extended to mode-II cracks and modified to account for more complex loading conditions. According to Griffith's theory, crack propagation occurs when the energy release rate surpasses the energy required for crack propagation. The methodology rooted in Griffith's theory assumes the presence of initial cracks and their self-similar growth [14].

Sih [76]; [77] successfully used a strain energy density factor to predict crack initiation and direction. The theory is based on two fundamental hypotheses: (1) the critical intensity of strain energy governs the onset of crack propagation, and (2) crack initiation begins in radial direction where the strain energy density is minimal.

In recent decades, phase field models have been extensively utilised to simulate an array of fracture problems, including dynamic fracture [13]; [60] and [97], ductile fracture, [1]; [12]; [52] and [72] cohesive fracture [60]; [86] and [87], in the STS tests [98]; [99], notched semi-circular bend (NSCB) tests [96], direct tension tests [96], and hydraulically driven fracturing [50].

Phase Field Models (PFMs) within the mechanics community are widely considered an extension of Griffith's fracture theory and have garnered increasing popularity in recent years [54]; [55]. The anisotropic phase field model proposed by Miehe et al. [55] is employed to demonstrate the construction of PFMs.

In this study, we propose a phase field model for simulating brittle fractures in granite by using the driving force called principal stress criterion in the evolution equation of the phase field which was presented by Miehe [54]. The strain and/or stress tensor is decomposed into a negative part as compressive tensor and a positive part as tensile tensor [53]. By using the spectral setting in COMSOL, this driving force is established using both compressive and tensile components of the stress.

Consider an elastic body  $\Omega \subset R^d$  (where  $d \in \{1,2,3\}$ ), representing the spatial dimensions as illustrated in Figure 26d. The external boundary and the internal discontinuity set of this elastic body are denoted as  $\delta\Omega$  and  $\Gamma$ , respectively. The phase field method is typically employed by integrating it with a variational approach, which necessitates that the fracture energy  $\psi_f$  be derived from the stored elastic energy  $\psi_\varepsilon$ . Fracture propagation can be conceptualised as a process that minimizes the energy functional  $L$  according to

$$L = \underbrace{\int_{\Omega} \psi_{\varepsilon}(\varepsilon) d\Omega}_{\psi_{\varepsilon}} + \underbrace{\int_{\Gamma} G_c d\Gamma}_{\psi_f} - \underbrace{\int_{\Omega} b \cdot u d\Omega - \int_{\partial\Omega_t} t \cdot u dS}_{W_{\text{ext}}}, \quad (2)$$

where  $u$  represents the displacement field,  $\psi_{\varepsilon}$  is the elastic energy density,  $G_c$  denotes the critical energy release rate, and  $W_{\text{ext}}$  signifies the external work, with  $b$  being the body force and  $t$  the surface traction. Additionally, the linear strain tensor  $\varepsilon = \varepsilon(u)$  is defined as

$$\varepsilon = \frac{1}{2} [\nabla u + (\nabla u)^T]. \quad (3)$$

A key difficulty in applying the variational approach directly to fracture processes in numerical simulations is managing the discontinuous displacement field at fracture sets and determining the optimal fracture set in phase field so that the length of the fracture set in both physical fields is consistent. To overcome these numerical challenges, Bourdin et al. [14] and Miehe et al. [51] regularised the variational model by introducing the energy functional,  $E$ :

$$E = \int_{\Omega} \psi_{\varepsilon}(\varepsilon, \varphi) d\Omega + \int_{\Omega} G_c \left( \frac{\varphi^2}{2l_0} + \frac{l_0}{2} |\nabla \varphi|^2 \right) d\Omega - \int_{\Omega} b \cdot u d\Omega - \int_{\partial\Omega_t} t \cdot u dS, \quad (4)$$

where  $\varphi(x, t) \in [0,1]$  (with  $x$  being a position vector) is an auxiliary field, known as the phase field, which is employed to diffuse the crack surface over the domain  $\Omega$  as depicted in Figure 26h. Consequently, in the regularised model, the phase field  $\varphi$  assists in smoothing out discontinuities, facilitating numerical treatment of fractures:

$$\varphi = \begin{cases} 0 & \text{if material is intact} \\ 1 & \text{if material is fully cracked} \end{cases}$$

Additionally, in Eq. (4),  $l_0$  denotes the length scale parameter, which controls the transition region of the phase field. The length scale parameter, therefore, indirectly reflects the width of the crack. This characteristic has been validated by numerous numerical simulations [55]; [96] and [97] which demonstrate that the crack region becomes wider with an increasing  $l_0$ , while the phase field will represent a sharp crack when  $l_0$  approaches zero.

Meihe et al. [54] defined the evolution of the crack phase field as a function of the difference between the effective driving force  $(1 - \varphi)H$  and the geometric crack resistance  $[\varphi - l^2 \Delta \varphi]$  according to

$$\kappa = (1 - \varphi)H - [\varphi - l^2 \Delta \varphi]. \quad (5)$$

Eq. (5) can be interpreted as a generalised Ginzburg-Landau-type structure, where the right-hand side is derived from the variational derivative of a total energy expression,  $H$  is the local crack driving force and  $\kappa$  is crack update or evaluation. The phase-field fracture driving force relies on the principal stress criterion concept, as its ability to predict microstructural crack nucleation and growth has been demonstrated [54]. The elastic energy can be partitioned into different components to model fractures arising from various mechanisms in the phase field method. For instance, shear fracturing is caused by compressive stress, and tensile fracturing occurs under tensile stress. These mechanisms are the ones that occur simultaneously in the failure process of UCS and TCS in rock mechanical tests under compressive and tensile stress, which means that no separation is made between tensile and compressive parts in this method. This approach has the advantage of significantly simplifying the structure of the equations. However, it comes at the expense of physical accuracy, particularly for shear and cyclic loading conditions [17]. Then, the function of crack driving force  $D$  in this method is defined as

$$D = \xi \left\langle \left( \frac{\sigma_{\text{ext}}}{\sigma_c} \right)^2 - 1 \right\rangle, \quad (6)$$

where  $\langle \mp \rangle$  are the Macaulay brackets and  $\sigma_{\text{ext}}$  is the external crack driving stress. Inserting Eq. (6) into the phase-field balance equation (5) yields a model capable of nucleating and growing cracks based on mechanisms driving microstructural damage. The dimensionless parameter  $\xi$  (Eq. (6)) triggers the activation of damage due to the elasto-plastic contribution and governs the post-nucleation behaviour. The phase-field damage tends to increase sharply for high values of  $\xi$ , whereas low propagation rates are obtained for small  $\xi$ . Moreover,  $\xi$  is dependent on the local stored energy density parameter, suggesting the need for experimental calibration to define the most accurate  $\sigma_{\text{ext}}$  and  $\sigma_c$  relation. In this work,  $\sigma_c$  is assumed to be equal to the crack initiation threshold ( $\sigma_{\text{ci}}$ ),  $\xi$  is assumed to be proportional to Mode II fracture toughness  $K_{\text{IIC}}$  and the magnitude of  $\xi$  can be estimated for the choices of  $l_0$ , Poisson's ratio and  $\sigma_c$  [54]; [91]. Miehe et al. [55] formulated a new method, also known as the crack phase field damage method, with discrete element technique based on cracking energy and energy for crack propagation.

The COMSOL Multiphysics software [17] code includes the phase field damage model and in this study the laboratory behaviour of Padang granite TG34 is simulated through the utilisation of Crack Phase Field Damage Model (CPFDM), specifically developed within the COMSOL software framework.

## 1.2 Numerical approach 2: Voronoi grain-based model (VGBM)

An important advantage of grain-based methods such as VGBM compared to conventional continuum methods lies in their ability to simulate the progressive fracturing of robust, brittle rocks under diverse loading conditions. In contrast, continuum methods typically depict intact rock failure solely through yielded elements or zones, activated when the internal stress exceeds the assigned strength threshold. However, grain-based methods excel in emulating fracture initiation during pre-peak loading stages, as well as the subsequent propagation of these fracture events that may culminate in the detachment of rock fragments.

According to Goodman et al. [29] the joint element is a one-dimensional four-noded quadrilateral element with a negligible thickness [68]. It is an edge-to-edge contact in which interconnectivity does not change with time. Figure 26g and Figure 26i present the configurations of a joint element before and after deformation. The two sides of the joint element have equal lengths. Before deformation occurs (cf. Figure 26g) nodes 1 and 2 of the joint element share the same position, while nodes 3 and 4 share a different and other position. When the blocks start to deform, the nodes can move normally and tangentially from each other. Therefore, the stiffness matrix of the Goodman's joint consists of two components: normal stiffness  $K_n$  and shear stiffness  $K_s$ . According to Riahi et al. [68], large displacement, rotation, or strains of discrete objects can be accommodated by the joint element as long as these mechanisms do not change contacting node couples. Based on Hooke's Law, equations (7) and (8) establish the relationships between normal ( $\Delta U_n$ ) and shear ( $\Delta U_s$ ) displacement and normal ( $\Delta F_n$ ) and shear ( $\Delta F_s$ ) force increments (Figure 26d).

$$\frac{\Delta F_n}{L} = K_n \Delta U_n \quad (7)$$

$$\frac{\Delta F_s}{L} = K_s \Delta U_s \quad (8)$$

In the context of the VGBM-RS2, the yielding of joint elements is determined by specific failure criteria like the Mohr-Coulomb failure criterion. Within this model, yielding can take place either within the grains themselves or at the grain boundaries. In some cases, fractures within individual grains might occur due to weaker points, while in other scenarios, the intergranular boundaries could be weaker and thus are more prone to yielding and fracturing. The model accommodates both possibilities, allowing for a comprehensive representation of the varying ways in which yielding and fracturing can manifest within the material's structure.

Riahi et al. [68] compared this new technique also known as the combined continuum-interface method to the discrete element technique and emphasise that at a specific instance in time, if an assembly of discrete objects with edge-to-edge contacts are replaced by a combined continuum-interface model, the resulting algebraic equations would be identical. The advantage of discontinuum methods and the combined continuum-interface method over continuum methods is that progressive fracturing of hard brittle rocks under various loading conditions can be explicitly simulated.

The RS2 software [70] code is based on the combined continuum-interface model. In this study the laboratory behaviour of Padang granite TG34 is simulated through the utilisation of a combined continuum-interface Voronoi Grain Based Model (VGBM), specifically developed within the RS2 software framework.

## 2. Model configuration

Numerical models were developed to replicate the laboratory experiments performed on Padang granite TG34 specimens within this study. Numerical simulations were conducted using a cylindrical specimen with an idealised dimension of 40 mm in diameter and 80 mm in length (Figure 25).

In the model for the uniaxial compressive strength test (UCS), the experimental setup involved the implementation of steel loading platens positioned both above and below the sample (Figure 26a and Figure 26d).

For the time-dependent study used in CPFDM, loading was applied with a controlled strain rate ranging from  $1 \cdot 10^{-3}$  to  $1 \cdot 10^{-6} \text{ s}^{-1}$ , corresponding to a displacement rate of  $0.08 \cdot 10^{-3}$  to  $0.08 \cdot 10^{-6} \text{ mm.s}^{-1}$ . The RS2 software is based on a stationary method, therefore it is required to match the strain rate with the amount of displacement at each stage of the simulation. The amount of constant strain in each stage was calculated by multiplying the total model length (including length of specimen and two pieces of steel plate) by the strain rate providing the applied displacement rate of  $1.6 \cdot 10^{-5} \text{ m}$  per stage, corresponding to a strain rate of  $1 \cdot 10^{-4} \text{ s}^{-1}$ .

The geometric configuration of the models as well as the boundary conditions and microcracks are illustrated in Figure 26a and Figure 26d. The upper boundary induces displacement and the lower boundary remains fixed during the loading.

We utilised an unstructured mesh of triangular finite elements (Figure 26c) to discretise the problem domain. In this mesh, pre-existing cracks are characterised by crack nodes, and new cracks are introduced by the phase field damage model in the matrix domain (Figure 26f and Figure 26h).

The mineral parameters for the modulus of elasticity, density, and Poisson's ratio were incorporated into the CPFDM using an image analysis technique (Figure 25).

Additionally, micro-fractures with a length of 1 mm were randomly generated using DFN library.

In VGBM, as suggested by the previous studies, at least 10 blocks across the width of the sample should be realised to capture realistic fracturing patterns [25]; [27]; [28]; [31]; [41]; [48] and [95]. The sizing of Voronoi blocks with an average diameter of 1 mm was determined by implementing an average length of the sides of the Voronoi grains of 0.75 mm. In this study, our modelling approach aimed to approximate the mean grain size, rather than precisely replicating the grain size distribution. This distinction is a consequence of the limitations inherent in the modelling tools provided by RS2. Within the blocks, discretisation was achieved using six-noded triangular elements, and the mesh density was optimised to strike a balance between computational cost and mesh quality within the blocks (Figure 26e).



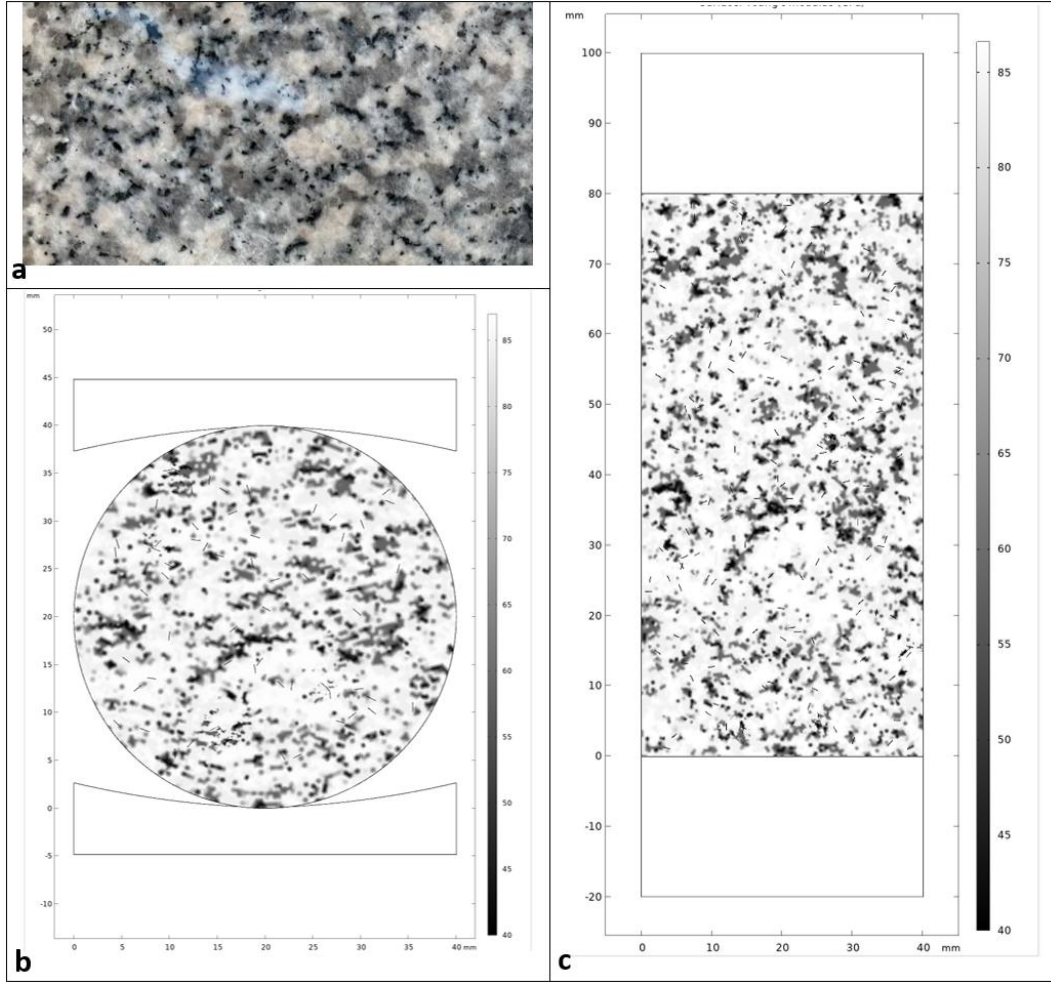


Figure 25: The mineralogical parameters used for CPFDM based on image analysis technique (a) photo of Padang granite TG34, (b) mineral's Young's modulus distribution in STS and (c) mineral's Young's modulus distribution in UCS.

Regarding the configuration of block shapes, the "medium irregular" option was chosen to introduce a high degree of geometrical homogeneity into the model (depicted in Figure 26a-b). Once the initial Voronoi mesh was generated, it remained constant throughout the subsequent analyses to obviate the need for recalibrating model parameters each time a new mesh was used, thus streamlining the analysis process.

Chemical analyses and petrological investigations conducted in the laboratory showed that the granite's mineralogical composition predominantly comprises quartz, feldspars (both K-rich and Ca-rich), and biotite. The simulation considers only a single mineral type representing silicate grains. The chosen constitutive failure model within the VGBM is the Mohr-Coulomb failure criterion, which accommodates peak and residual strength values and incorporates a tension cut-off yield function. The "elastic-brittle-plastic" characteristic signifies an instantaneous drop in material strength from peak to residual levels upon yielding. Comprehensive details about the yield function, potential function, and plastic flow rules can be found in the RS2 manual [70].

Lateral displacement monitoring points were added along both sides of each specimen (Figure 26a and Figure 26d). By calculating the average lateral displacement, the corresponding lateral strain at each stage of the test was determined. To record the mechanical response of the specimen, axial stress monitoring points were strategically

placed along the central axis of the specimen in VGBM and in top of the specimen in CPFDM. These monitoring points were evenly distributed to capture a comprehensive view of the axial stress distribution. The average of these recorded values served as a representative measure of axial stress. The combination of axial stress and lateral displacement monitoring points provides a comprehensive perspective on the specimen's response to loading.

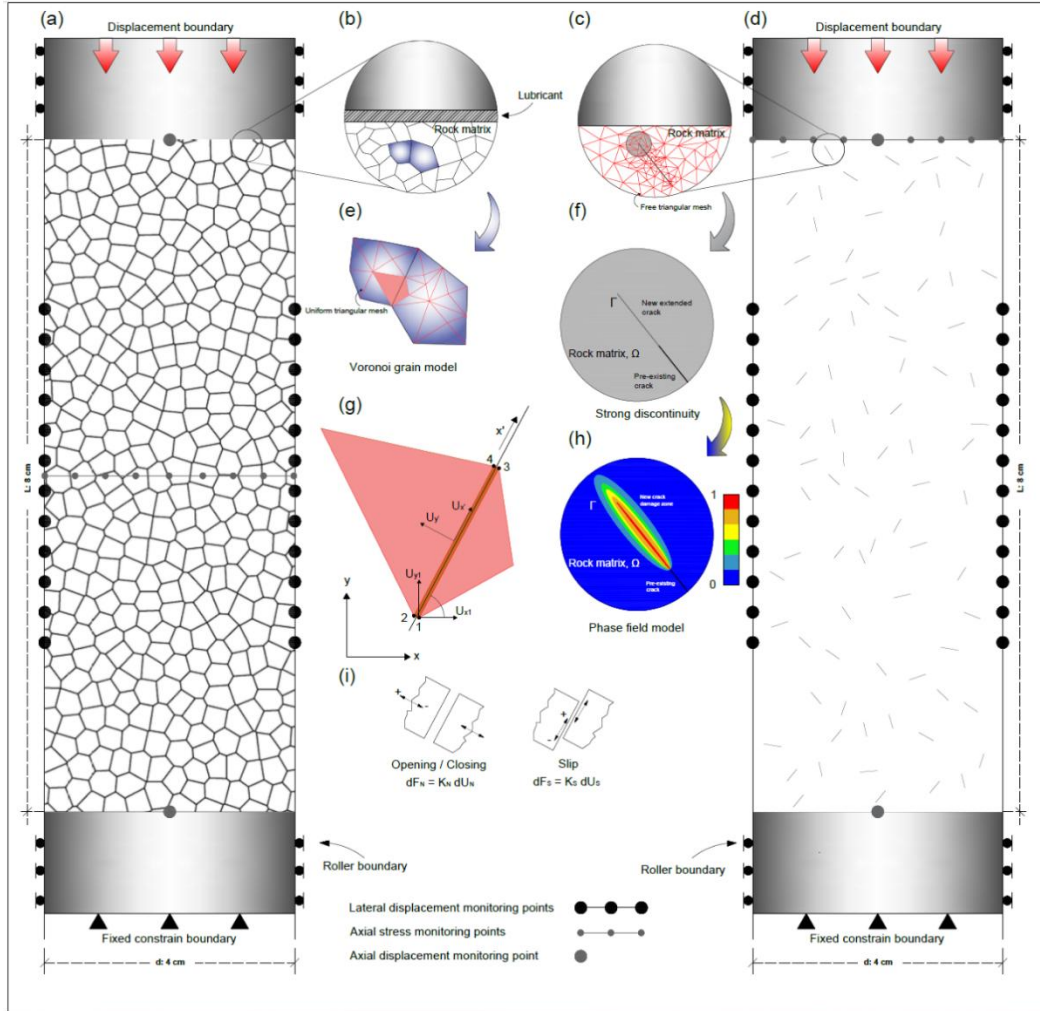


Figure 26: (a) Uniaxial compressive strength test model used by VGBM-RS2, (b) lubricant position, (c) free triangular mesh in COMSOL, (d) uniaxial compressive strength test model used by CPFDM-COMSOL, (e) triangular mesh in RS2, (f) pre-existing and new crack in CPFDM, (g) Goodman's joint element in the interface between two blocks, (h) new existing crack in phase field model.

## 2.1 Calibration assumptions

### 2.1.1 CPFDM-COMSOL

The purpose of the calibration of the CPFDM was to align its key parameters, i.e., UCS, STS, and Young's modulus with the laboratory properties of Padang granite TG34. Microstructural properties can be categorised in three groups, including those associated with:

- 1) Crack geometry, i.e., crack length,  $L$  (mm) and crack frequency  $q$  (cm<sup>2</sup>),
- 2) Phase field damage parameters, i.e., critical fracture stress  $\sigma_c$  (MPa), post peak slope  $\xi$  (dimensionless), internal length scale  $l_0$  (mm) and external stress  $\sigma_{ext}$  (MPa) calculated from the output of the model at the macroscopic failure stress, and
- 3) Elastic material properties, i.e., Young's modulus (GPa), Poisson's ratio (-) and bulk density (kg.m<sup>-3</sup>).

It should be noted that  $l_0$  is set to 1 % of the length of pre-existing cracks and is maintained as a constant, and size of mesh is set to at least 10 % of  $l_0$ .

Figure 27 shows the calibration flowchart of main parameters of CPFDM.

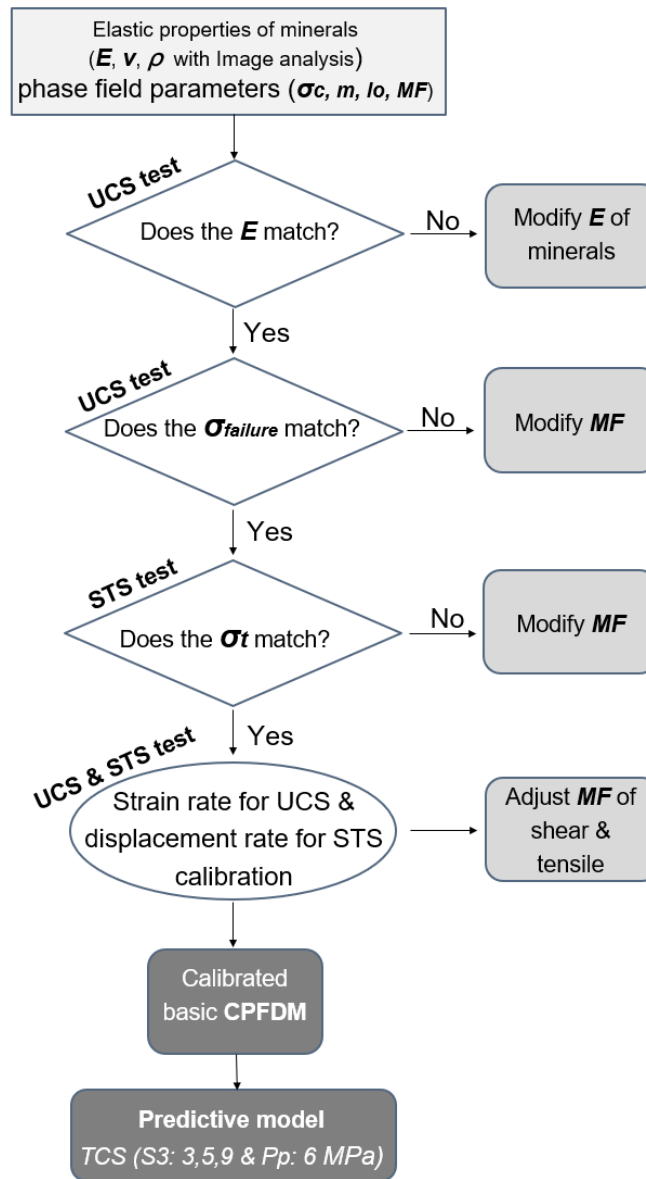


Figure 27: Calibration flowchart of main parameters in CPFDM-COMSOL ( $MF$ : material factor).

## 2.1.2 CPFDM-COMSOL sensitivity analysis

The sensitivity analyses were based on a calibrated model for Padang granite TG34. These analyses involved UCS calculating when varying one particular factor while maintaining all other factors constant. As illustrated in Figure 28, with a constant material factor ( $\xi$ ) and critical stress ( $\sigma_c$ ), an increase in the number of micro-fractures leads to a higher geometric factor, resulting in a decrease in uniaxial resistance. Additionally, an increase in critical stress ( $\sigma_{ci}$ ) from 50 to 80 MPa leads to an enhancement in uniaxial strength. This relationship is also true for different strain rates. Furthermore, an increase in the material factor ( $\xi$ ) results in a decrease in uniaxial strength (Figure 29). Similar to Figure 28, an increase in critical stress corresponds to an increase in the amount of reinforcement. This relationship holds across different models with varying numbers of micro-fractures.

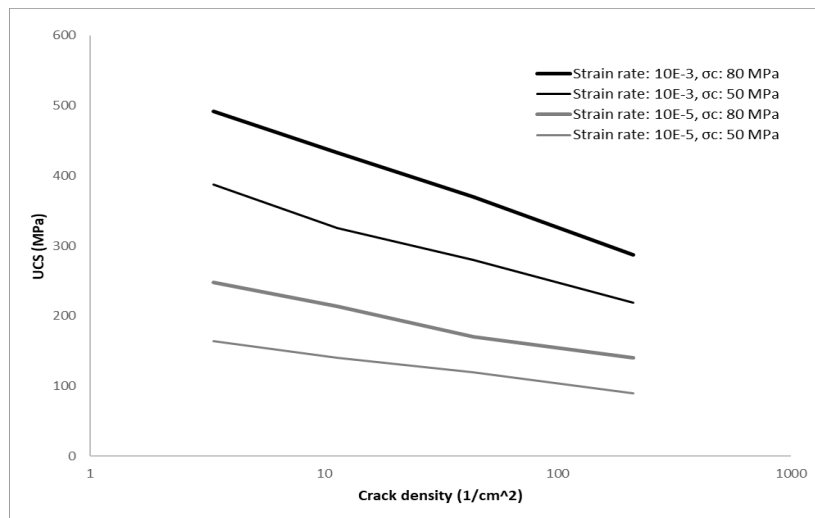


Figure 28: Effect of critical stress and relation between frequency of pre-existed micro crack and UCS (material factor,  $\xi = 1$ ).

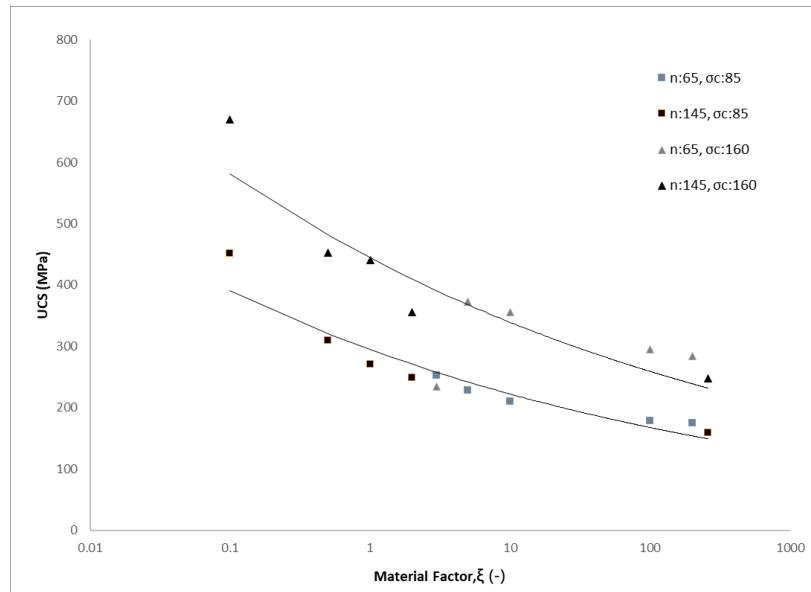


Figure 29: Relation between material factor and UCS.

## 2.2 VGBM-RS2

The primary objective of calibrating the VGBM was to align its macroscopic properties with the laboratory properties of Padang granite TG34. This calibration process encompassed matching key parameters such as STS, UCS, and Young's modulus to their corresponding laboratory values. Achieving this alignment required adjustments to several micro-properties, including those associated with both individual grains and grain boundaries.

By iteratively refining these micro-properties, the calibrated VGBM could accurately replicate the macroscopic behaviour of Padang granite TG34 observed in laboratory tests. The calibration process involved a delicate balance between adjusting these micro-properties while ensuring that the resulting model remained physically meaningful and relevant to the investigated rock material.

### 1) Properties of grains:

- a. Peak and residual tensile strength in MPa ( $\sigma_{tg}$  and  $\sigma_{tgr}$ );
- b. Peak and residual cohesion in MPa ( $c_g$  and  $c_{gr}$ );
- c. Peak and residual angle of internal friction in degree ( $\phi_g$  and  $\phi_{gr}$ );
- d. Young's modulus in GPa ( $E_g$ );
- e. Poisson's ratio in (-) ( $\nu_g$ ).

### 2) Properties of grain boundaries (i.e., joints):

- a. Peak and residual tensile strength in MPa ( $\sigma_{tj}$  and  $\sigma_{tjr}$ );
- b. Peak and residual cohesion in MPa ( $c_j$  and  $c_{jr}$ );
- c. Peak and residual friction angle in degree ( $\phi_j$  and  $\phi_{jr}$ );
- d. Shear stiffness and normal stiffness in MPa/m ( $K_s$  and  $K_n$ ).

**Remark 1.** UCS test and STS test are required to calibrate the material properties.

Confined tests (TCS) can be used to calibrate angle of internal friction of grains and friction angle of grain boundaries.

**Remarks 2.** Frictional properties of mineral grains are important in compression test according to the strength envelope of the Mohr-Coulomb failure criterion. Variation of friction angles between different mineral grains in the same rock sample is not significant. The average angle of internal friction of grains can be estimated from mineral experiments directly, or calibrated from residual behaviours in uniaxial compression test or macroscopic frictional behaviours in confined compression tests.

**Remarks 3.** The tensile strength of persistent discontinuities is generally zero. If a non-persistent discontinuity is loaded by a normal tensile stress and a shear stress, the strength should conservatively also be considered as negligible. The tensile strength of all types of discontinuities can therefore be assumed to be zero [90]. Therefore, by choosing a large value for the maximum tensile stress of the joints, we practically eliminated its effect in the model.

In Figure 30 is shown the calibration flowchart of main parameters of VGBM.

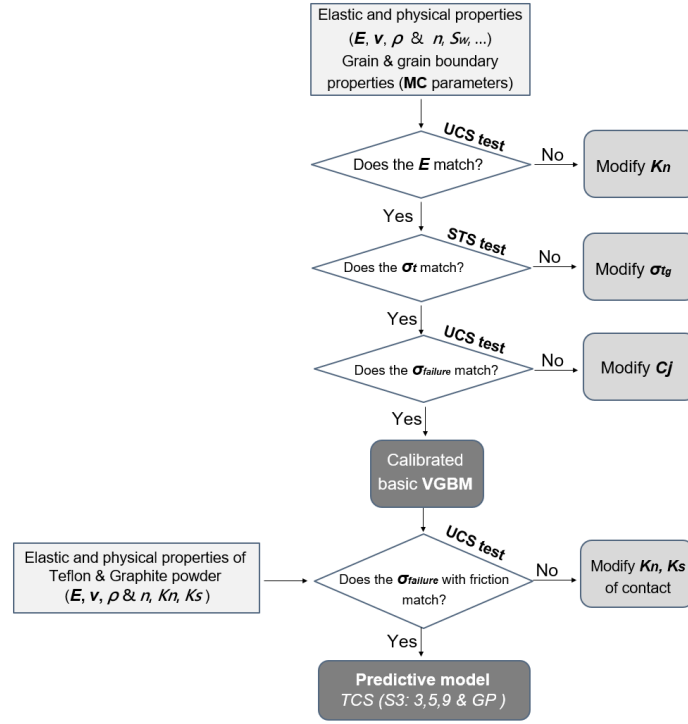


Figure 30: Calibration flowchart of main parameters in VGBM-RS2.

### 2.2.1 VGBM-RS2 sensitivity parameters analysis

In the broader context, each micro-parameter inherently exerts influence over multiple macroscopic responses within the VGBM. Nonetheless, the sensitivity study undertaken in this research has successfully identified the most pertinent correlations between micro-properties and their corresponding macroscopic outcomes. This strategic identification of key correlations has enabled the development of a comprehensive methodology that can be applied to calibrate the VGBM for diverse types of rocks, rendering the approach practical and adaptable.

The sensitivity analyses were built upon the foundation of the calibrated model for Padang granite. In these analyses, the methodology involved varying individual micro-properties while maintaining all other factors constant. By systematically altering one micro-property at a time, the study discerned the distinct effects of each micro-parameter on the behaviour of the VGBM. Furthermore, the investigation extended its purview to encompass additional factors, including the impact of finite element mesh and the arrangement of Voronoi tessellation. Additionally, the study examined the coherence of friction between the specimen and the steel jaw.

Rogenes et al. [71] presented comprehensive results from the sensitivity analysis of his VGBM model, thoroughly discussing the impact of each micro-parameter on various thresholds. This study extends that analysis by investigating the effect of these micro-parameters only on UCS. In summary, we can conclude that an investigation into the roles of normal ( $K_n$ ) and shear ( $K_s$ ) stiffness of grain boundary within the VGBM-RS2 revealed that the  $K_n/K_s$  ratio significantly affects the UCS (Figure 32); higher ratios, achieved by reducing  $K_s$ , lead to greater shear displacements and faster tension development at crack tips, decreasing UCS. Figure 32 shows that increasing  $K_n$  enhances

model rigidity, raising both the Young's modulus and UCS, and reducing block displacement, thereby inhibiting fracture initiation and propagation. Rogenes et al. [71] showed that variations in the Young's modulus ( $E_g$ ) of Voronoi grains influence not only the macroscopic Young's modulus but also Crack Damage ( $CD$ ), with higher  $E_g$  promoting trans-granular fractures and unstable fracture propagation. Changes in the Poisson's ratio of Voronoi grains affect the macroscopic Poisson's ratio and UCS by reducing lateral strain and increasing material rigidity. The study also found that peak cohesion of joints ( $c_j$ ) and Voronoi grains ( $c_g$ ) determines UCS, with strength increasing with decreasing  $c_j$  or  $c_g$ , and highlights limitations in modelling rocks with high UCS-to-STS ratios. Friction angle parameters of joints and internal friction of grains, while minimally impacting UCS (Figure 31), are crucial for accurately representing friction in triaxial tests. Finally, grain tensile strength significantly impacts macroscopic tensile strength and UCS, with the model's tensile strength reaching approximately 90 % of the value of grain's tensile strength, emphasizing its importance in fracture behaviour. The calibration of the angle of internal friction was done with results from triaxial compressive strength tests.

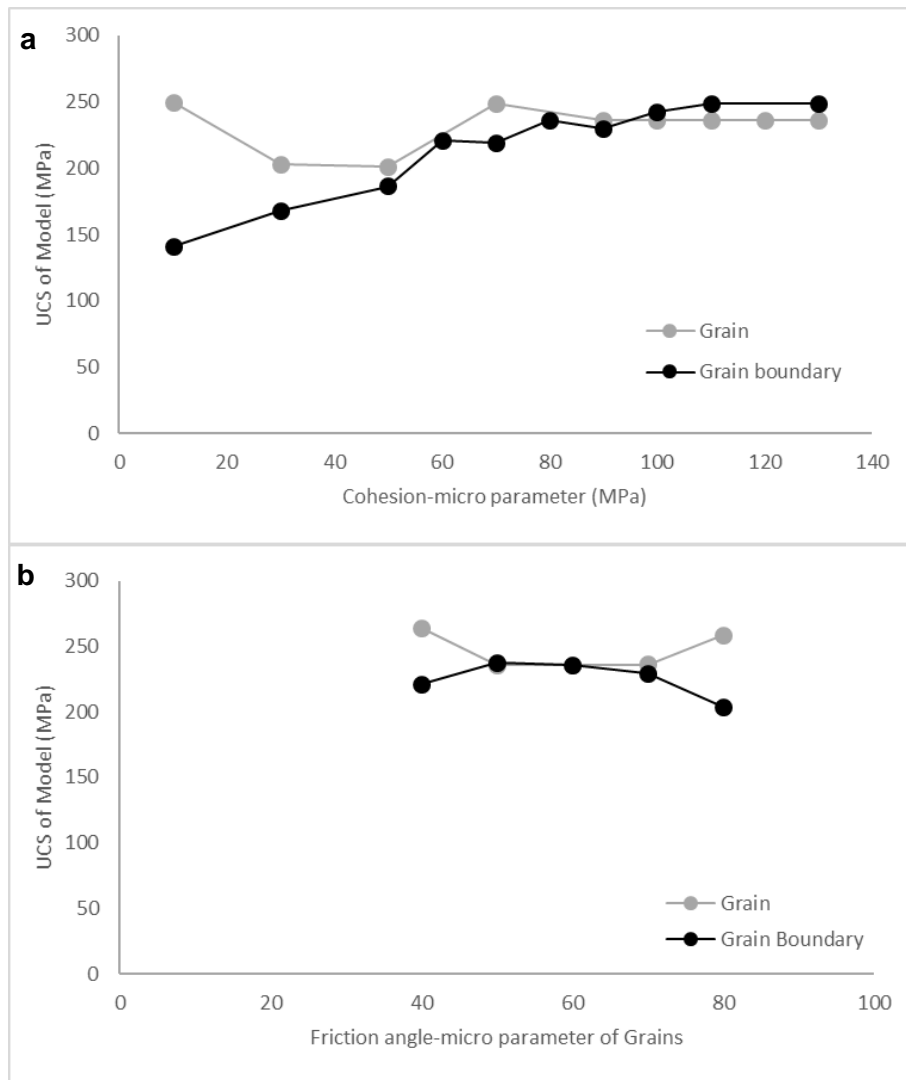


Figure 31: Sensitivity analysis of Mohr-coulomb parameters of VGBM-RS2: (a) effect of cohesion of grain and grain boundary on UCS, (b) effect of friction angle of grain and grain boundary on UCS.

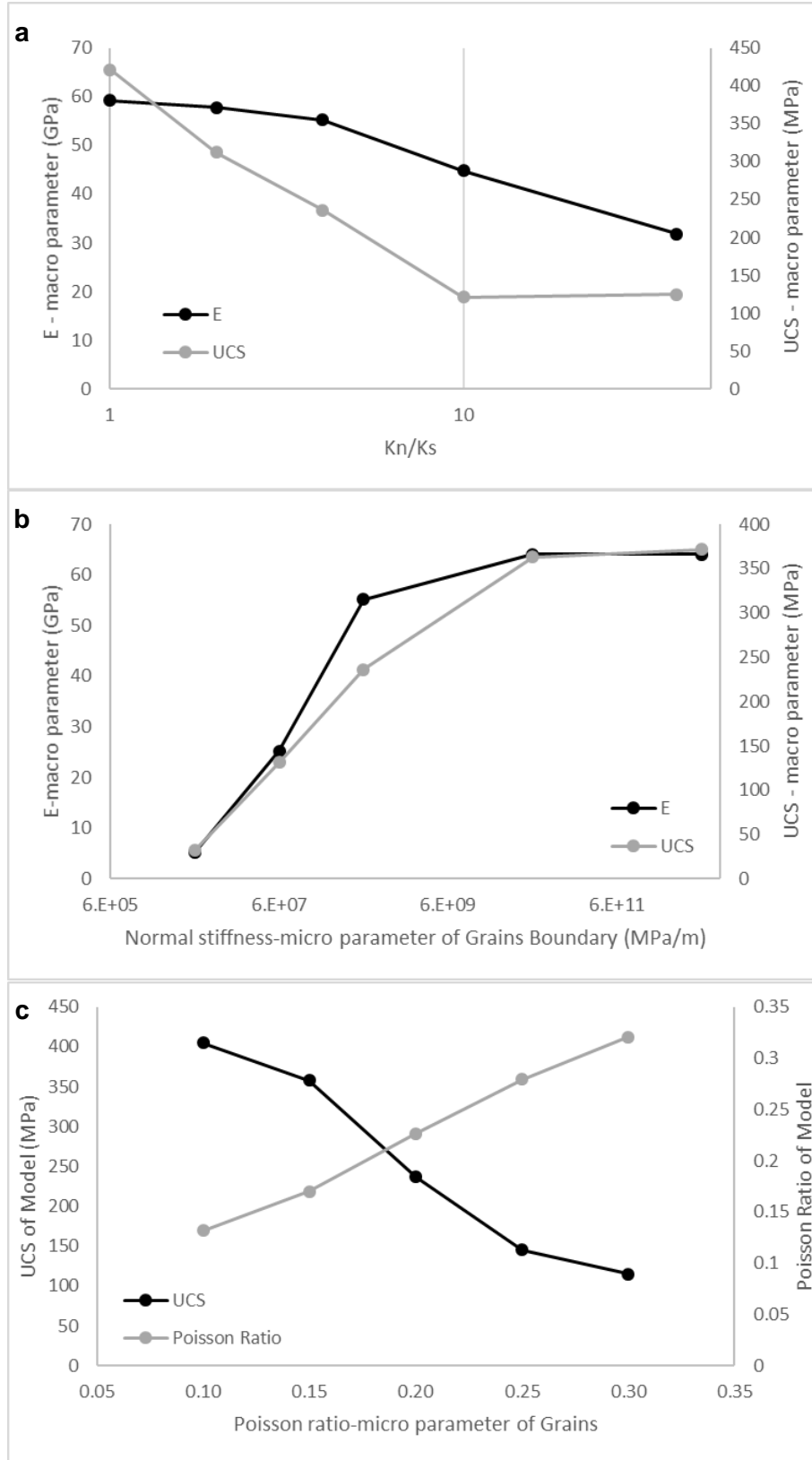


Figure 32: Sensitivity analysis of stiffness parameters of VGBM-RS2: (a) effect of the  $K_n/K_s$  ratio on bulk Young's modulus and UCS, (b) effect of  $K_n$  on Young's modulus and UCS with constant  $K_n/K_s$  ratio, (c) effect of Poisson's ratio of grain on UCS and Poisson's ratio of model.



An assessment of the Finite Element Method (FEM) mesh on VGBM-RS2 results, conducted through UCS tests with element counts ranging from 6,000 to 12,000, revealed that increasing the number of FEM elements leads to a decrease in UCS, likely due to enhanced particle damage and fracturing (Table 11). However, Young's Modulus and Poisson's Ratio remained largely unaffected by mesh variations, indicating stability in these parameters. Additionally, the influence of Voronoi tessellation arrangement was evaluated through ten difference UCS test iterations with constant geometric heterogeneity and average joint length but varying grain positions. Results showed that grain arrangement affected compressive strength by less than  $\pm 7\%$ , suggesting a modest impact on the material's response to compressive loads (Figure 33).

Table 11: Effect of the number of finite elements on VGBM-RS2 response.

Test model	Finite mesh elements	Strength (MPa)
UCS	6,000	237
	10,000	236
	12,000	230

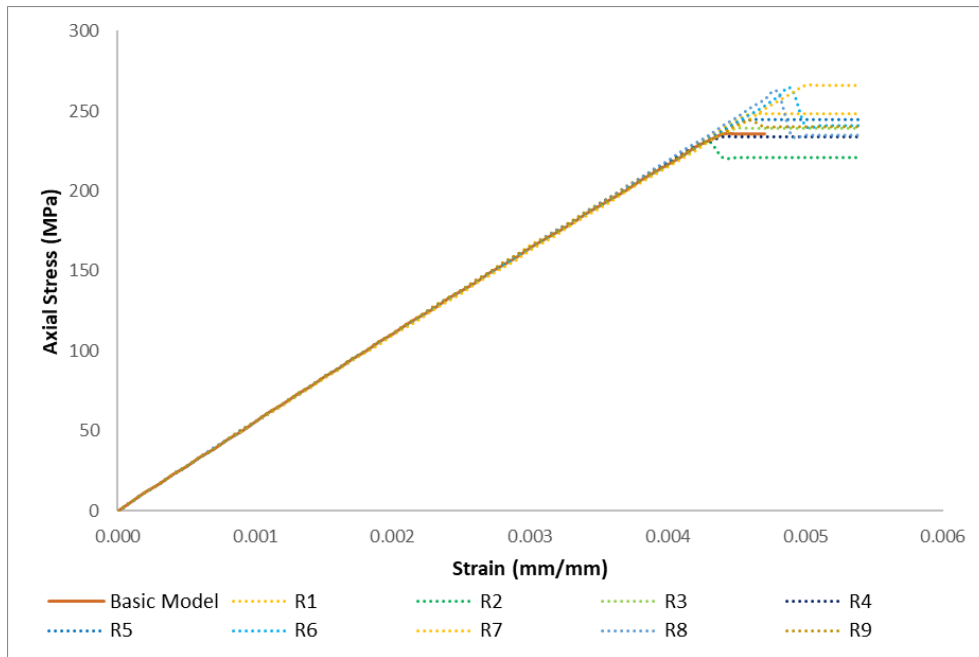


Figure 33: Numerical uniaxial compression test results of specimens used to investigate the effect of nine different grain arrangements.

## 2.3 Input calibrated parameters

The basic model (without lubricant) was calibrated first using the experimentally obtained microstructural parameters for further modelling with different strain rates and under different boundary conditions. The results of calibration parameters of VGBM-RS2 and CPFDM-COMSOL are summarized in Table 12 and Table 13.

Table 12: Calibrated micro-parameters used in the VGBM-RS2 for basic model of Padang granite TG34.

Type	Grain	Grain boundary
Stiffness micro-parameters	$E_g$ : 62 (GPa)	$K_n$ : $6.0 \cdot 10^8$ (MPa/m)
	$\nu_g$ : 0.2 (-)	$K_s$ : $1.5 \cdot 10^8$ (MPa/m)
Strength micro-parameters	$\phi_g$ : 50 (°)	$\phi_j$ : 60 (°)
	$c_g$ : 75 (MPa)	$c_j$ : 63 (MPa)
	$\sigma_{tg}$ : 10 (MPa)	$\sigma_{ij}$ : 30 (MPa)
	$\phi_{tg}$ : 10 (°)	$\phi_{ij}$ : 10 (°)
Residual strength micro-parameters	$\psi$ : 10 (°)	./.

Table 13: Calibrated micro-parameters used in the CPFDM-COMSOL for basic model of Padang granite TG34.

Type	Input parameters	Value
Linear elastic parameters	Quartz	$E$ : 63 (GPa)
		$\nu$ : 0.05 (-)
		$\rho$ : 2,648 (kg/m <sup>3</sup> )
	Plagioclase	$E$ : 58 (GPa)
		$\nu$ : 0.3 (-)
		$\rho$ : 2,610 (kg/m <sup>3</sup> )
	Feldspar	$E$ : 54 (GPa)
		$\nu$ : 0.3 (-)
		$\rho$ : 2,540 (kg/m <sup>3</sup> )
	Biotite	$E$ : 40 (GPa)
		$\nu$ : 0.25 (-)
		$\rho$ : 2,844 (kg/m <sup>3</sup> )
Pre-existing cracks geometry	inclination	0 - 170 (°)
	length	1 (mm)
	number	5 (1/cm <sup>2</sup> )
Phase field damage	Scalar length $l_0$	0.01 (mm)
	Critical stress $\sigma_c$	85 (MPa)
	Post peak slope $\xi$	0.18 (-)

## 3. A posteriori-simulation of experiments

### 3.1 Basic model and strain rate effect simulation

#### 3.1.1 CPFDM-COMSOL basic model

The results of the UCS test without lubricant between steel pistons and specimen's end phases (basic model) are visually presented in Figure 34, which plots all four obtained curves simultaneously. The CPFDM effectively represent various phases of the fracturing process, as described by Bieniawski [9]; [10]. These phases include the linear elastic response, initiation crack stress, stable crack propagation, unstable crack propagation, and eventual failure. However, it is important to note that certain aspects, such as the crack closure phenomenon and post-peak behavior, were not replicated by the model. The base model was simulated according to standard procedures under a strain rate of  $1 \cdot 10^{-5} \text{ s}^{-1}$ . Figure 35 illustrates the primary stages of crack initiation and failure in UCS test.

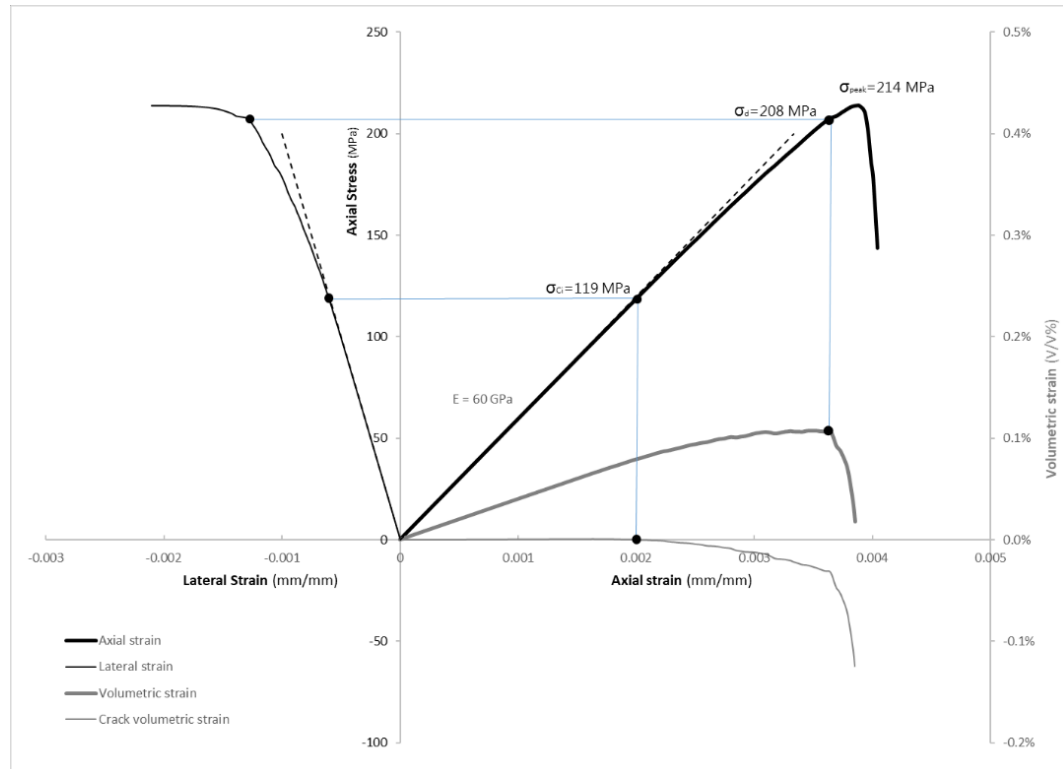


Figure 34: Stress-strain curves of basic model of CPFDM-COMSOL.

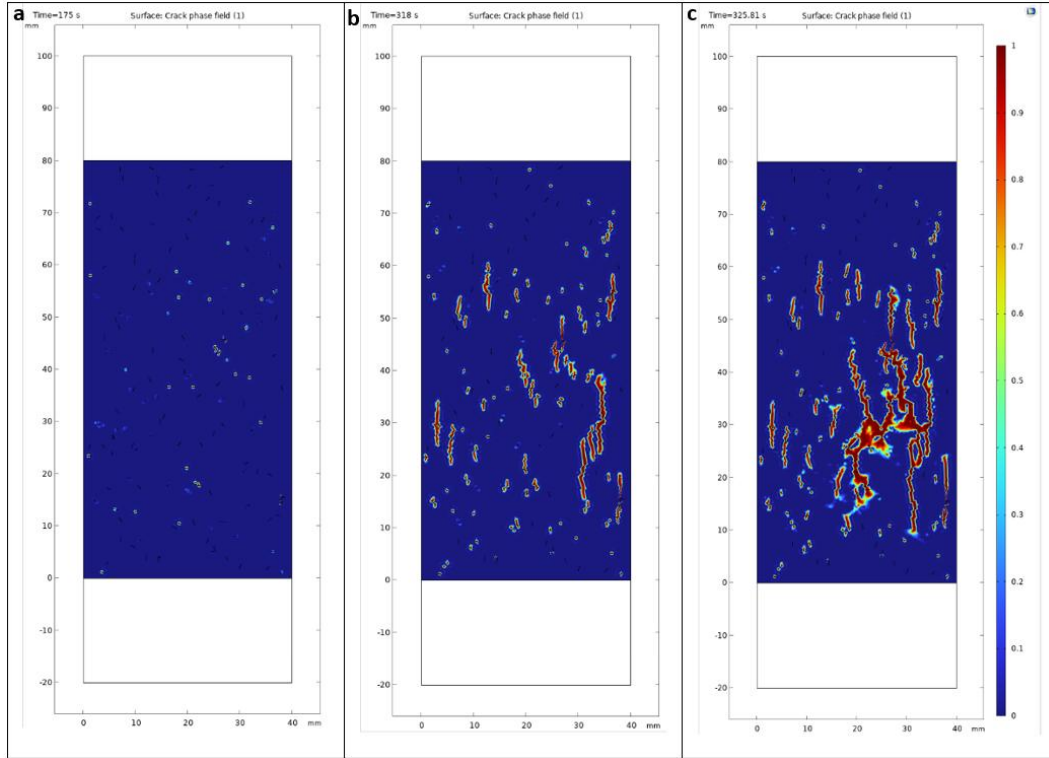


Figure 35: (a) Crack initiation, (b) final failure, and (c) post failure in basic model of CPFDM-COMSOL.

### 3.1.2 Strain rate effect simulation with CPFDM-COMSOL

To investigate the ability to simulate the effect of strain rate on the UCS, one model with a slower strain rate  $1 \cdot 10^{-6} \text{ s}^{-1}$  and two models with faster strain rates  $1 \cdot 10^{-4} \text{ s}^{-1}$  and  $1 \cdot 10^{-3} \text{ s}^{-1}$  were developed. For calibration, all parameters were kept the same as the base model, with adjustments made only to the material factor ( $\xi$ ). The material factor ( $\xi$ ) is related to the rate-dependent fracture toughness ( $K_C$ ). It should be noted that Yang et al. [92] and Bazant et al. [7] showed the relationship between strain rate and toughness in rocks. Figure 36 presents the graphs obtained from the aforementioned simulation results. Additionally, Table 14 compares the accuracy of these modelling results with the values obtained from practical tests.

Table 14: Comparing results of Padang granite TG34 experimental UCS test and modelling with the CPFDM-COMSOL under different strain rate.

Strain rate ( $\text{s}^{-1}$ )	Laboratory test (MPa)	CPFDM (MPa)	Material factor, $\xi$
$1 \cdot 10^{-3}$	258	255	0.65
$1 \cdot 10^{-4}$	$216 \pm 28$	231	0.25
$1 \cdot 10^{-5}$	$216 \pm 7$	214	0.18
$1 \cdot 10^{-6}$	$194 \pm 15$	204	0.17

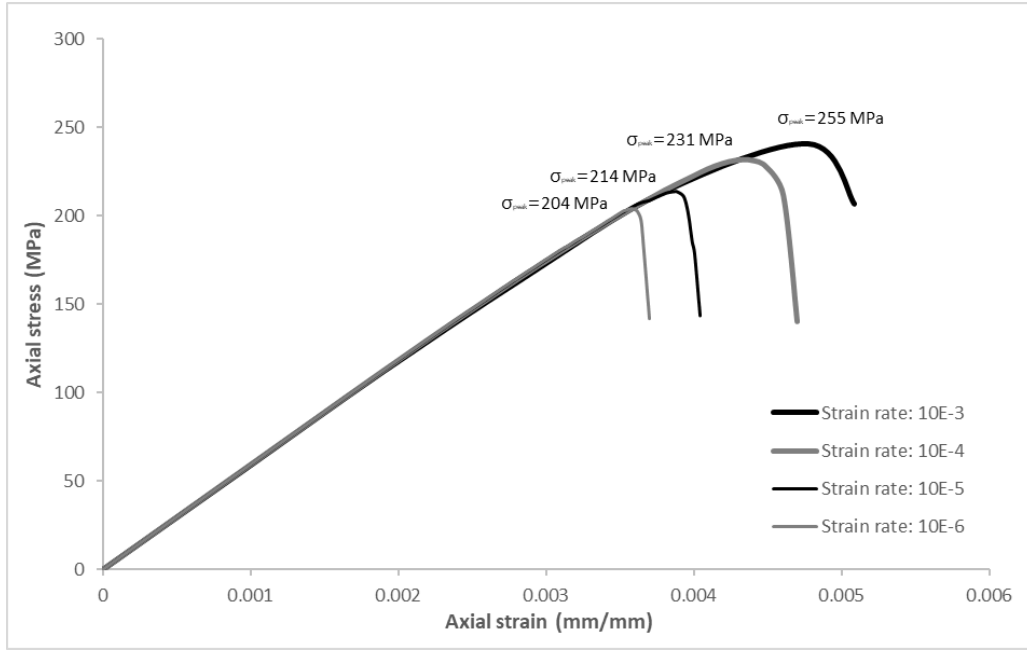


Figure 36: Stress-strain curves of UCS with different strain rate simulation with CPFDM-COMSOL.

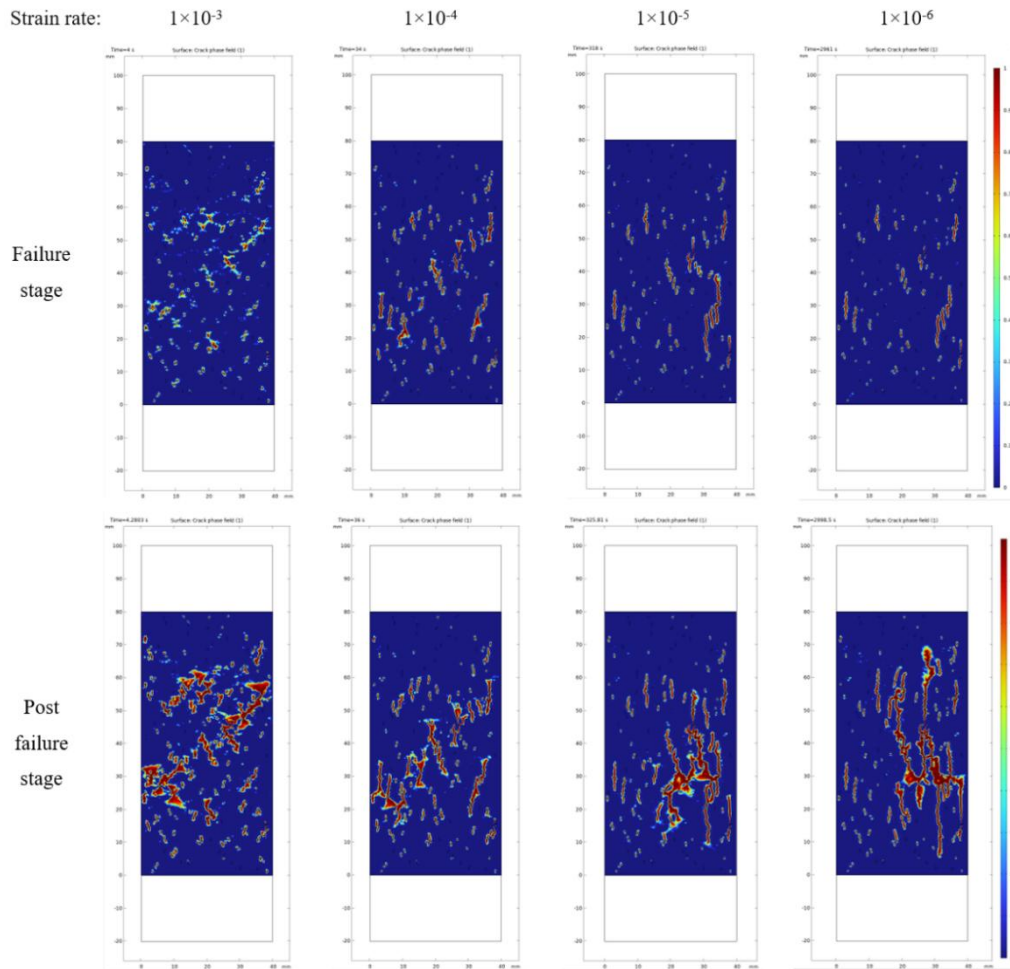


Figure 37: Failure and post failure stage of UCS for different strain rate simulations with CPFDM-COMSOL.

In Figure 37, the stages of failure and post-failure in uniaxial models under different strain rates are shown. With decreasing strain rate, fractures reorient from diagonal to vertical. This indicates a transition in the failure mechanism from shear to tensile type.

### 3.1.3 VGBM-RS2 basic model

The results of the UCS test with natural contact (without lubricant) are visually presented by plotting all three obtained curves simultaneously in Figure 38. A comprehensive representation of various phases of the fracturing process, as described by Bieniawski [8], [9], is observed through the application of the VGBM. Specifically, the following phases are evident in the curves: linear elastic response, initiation crack stress, stable - unstable crack propagation, and eventually failure. However, it is important to highlight that certain aspects, such as the crack closure phenomenon and post-peak behaviour, were not replicated by the model.

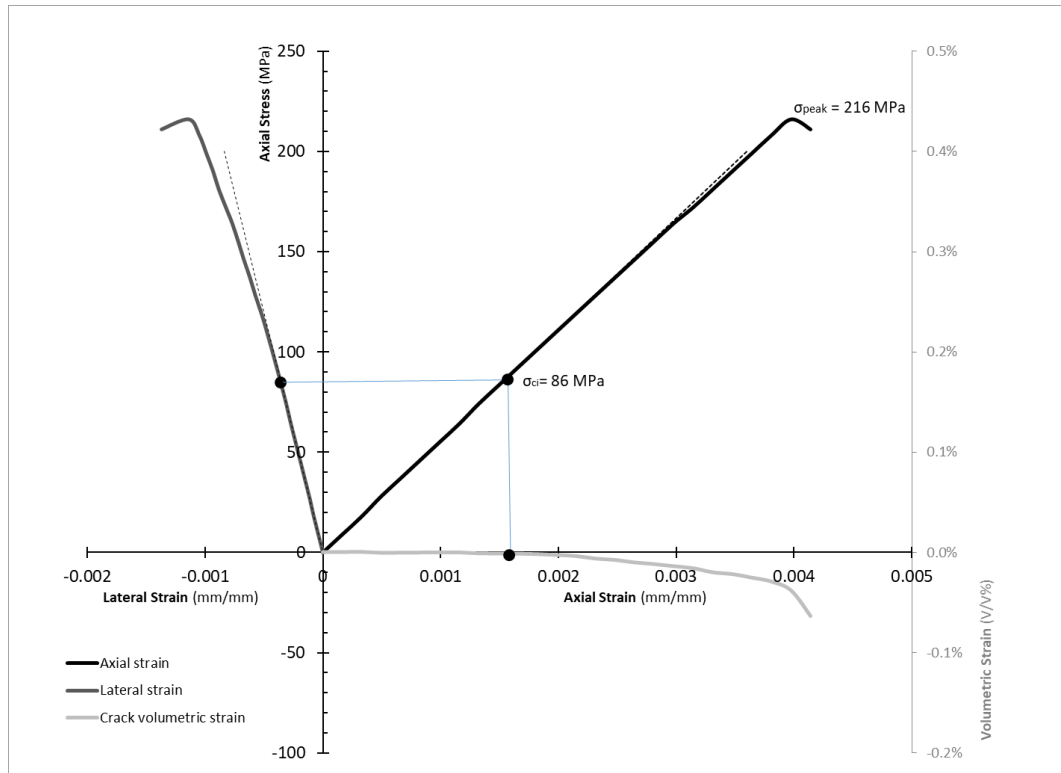


Figure 38: Stress-strain curves of basic model simulation of VGBM-RS2.

## 3.2 STS test simulations with calibrated parameters

In the model for the STS test configuration, steel loading platens were employed both above and below the test sample, as illustrated in Figure 39. The STS test entails the application of vertical constraint to the lower part of the specimen, while direct vertical displacement is imposed on the upper part. The contact interface between the upper part and the loading platen follows an arc region contact geometry, set at an angle of 15°.

Similar to the approach applied to the unconfined compression test, the STS test was executed in discrete stages.

The peak vertical load, denoted as  $P_{\max}$ , was subsequently extracted and serves as a pivotal parameter for further analysis according to the ASTM D3967-95a whose standard equation is employed to compute the splitting tensile stress on and the splitting tensile strength of the specimen. The controlled displacement increments, combined with the recording of reaction forces, contributed to the reliability and precision of the obtained results.

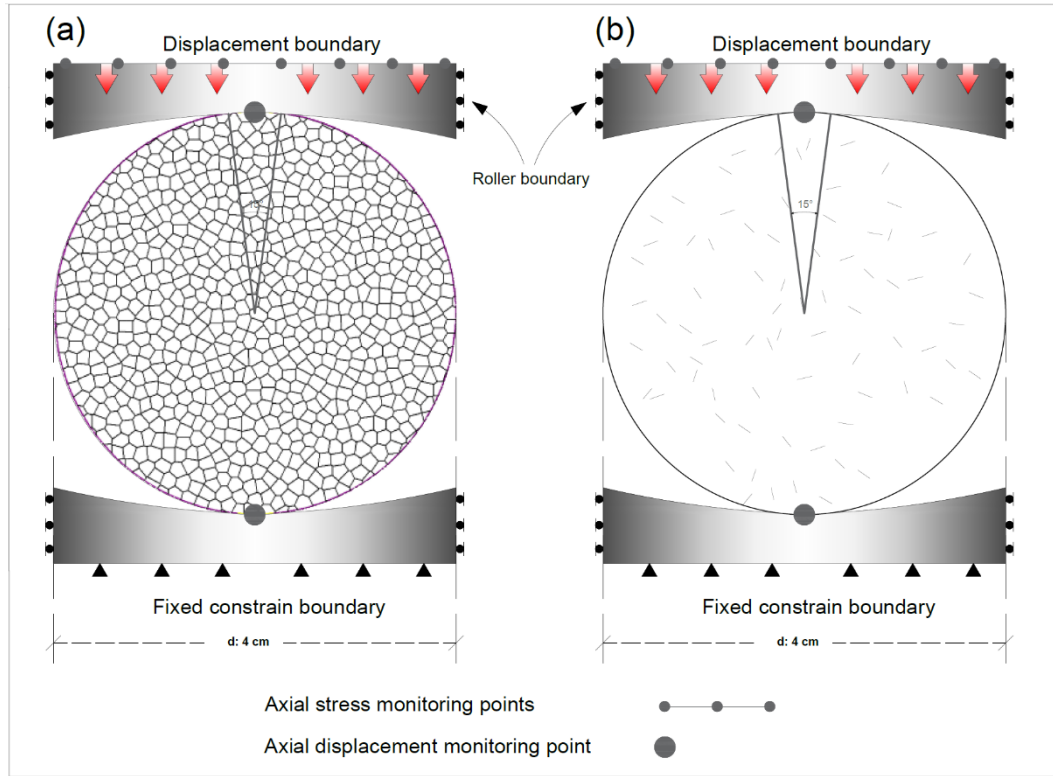


Figure 39: STS test model configuration (a) VGBM-RS2, (b) CPFDM-COMSOL.

### 3.2.1 STS simulation with CPFDM-COMSOL

The provided load-displacement diagram in Figure 40 illustrates the behaviour of Padang granite TG34 under indirect tensile stress loading during the STS test at three different displacement rates. The x-axis represents axial displacement in mm, while the y-axis represents  $P_{\max}$  in kN and had converted to maximum tensile stress in MPa for each rate. The model's calculated tensile strength closely aligns with the laboratory average, deviating by less than 1 % from the observed value.

Figure 42, Figure 43 and Figure 44 illustrate the fracture process during STS test on a rock specimen, with displacement rates of  $1.5 \cdot 10^{-4}$ ,  $1.5 \cdot 10^{-3}$  and  $1.5 \cdot 10^{-2} \text{ mm.s}^{-1}$ . These images show key stages from initial loading, crack initiation, and propagation, to final failure. Figure 42 to Figure 44 show that the fractures from the centre of the rock disc has started to grow towards the direction of maximum stress, i.e., upwards and downwards. Given the consistent orientation and distribution of pre-existing joints across all models, the initiation point of the fracture remains the same for all displacement rates. However,

during the crack propagation phase, the intensity of fracturing increases with higher loading speeds. This phenomenon manifests as a stronger and sharper fracture with greater aperture in thin sections (Figure 41). Displacement rates in STS models were calibrated equivalent to UCS models, with material factors of 0.05, 0.03 and 0.018 for models with displacement rates of  $1.5 \cdot 10^{-2}$ ,  $1.5 \cdot 10^{-3}$  and  $1.5 \cdot 10^{-4}$  mm.s<sup>-1</sup>, respectively.

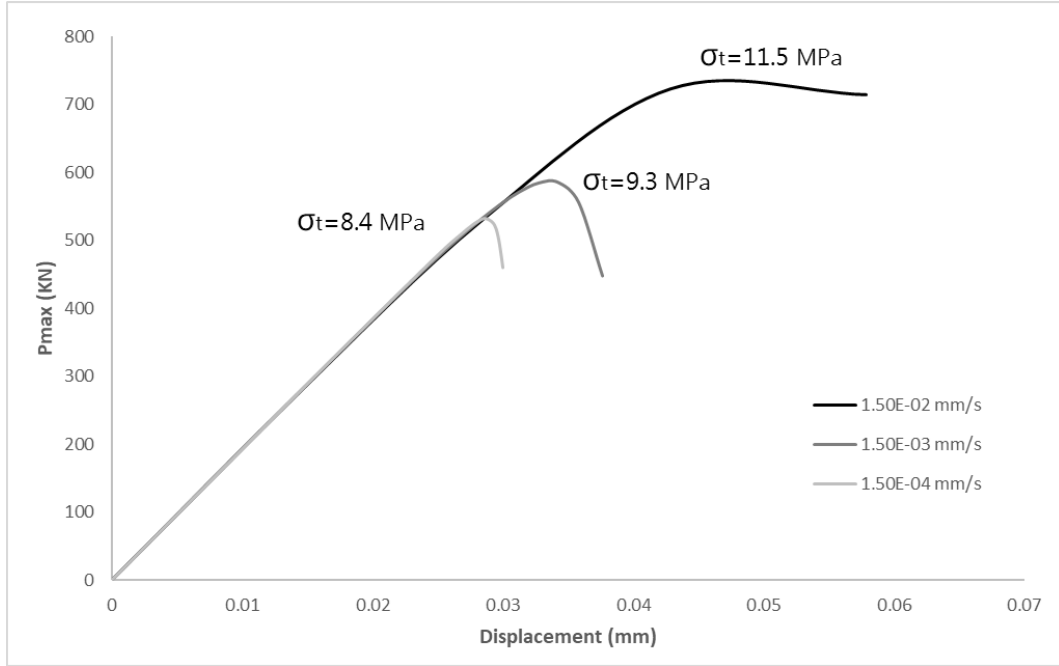


Figure 40: Axial load – axial displacement curve of STS tests with different displacement rates from CPFDM-COMSOL.



Figure 41: Microscopic view of tensile fracture under cross-polarized light: STS test with (a) displacement rate  $1.5 \cdot 10^{-4}$  mm.s<sup>-1</sup>, (b) displacement rate  $1.5 \cdot 10^{-3}$  mm.s<sup>-1</sup>, (c) displacement rate  $1.5 \cdot 10^{-2}$  mm.s<sup>-1</sup>.



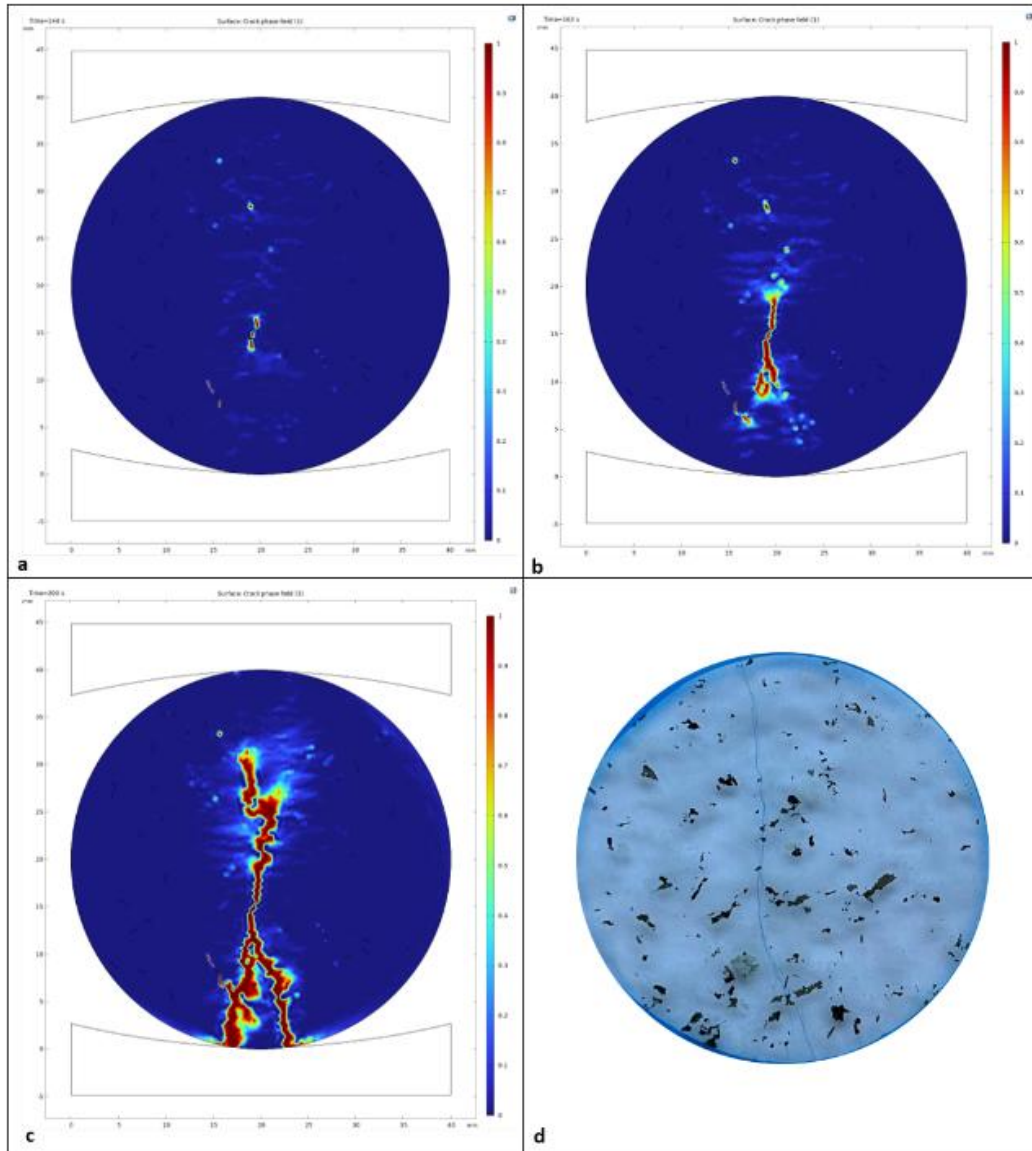


Figure 42: STS test simulation of displacement rate  $1.5 \cdot 10^{-4} \text{ mm.s}^{-1}$  with CPFD-M-COMSOL: (a) crack initiation, (b) crack propagation, (c) final failure and (d) thin section in natural light.

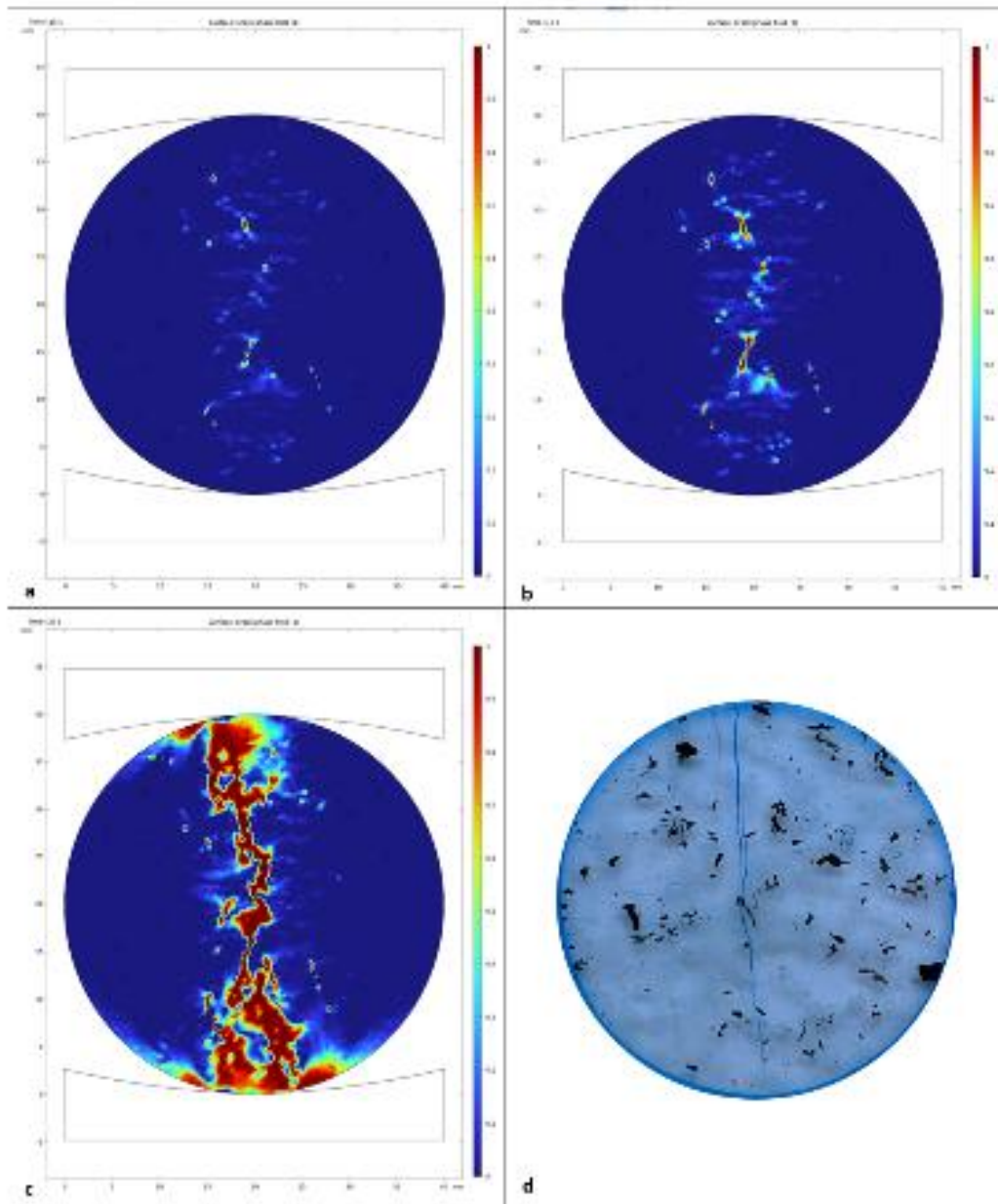


Figure 43: STS test simulation of displacement rate  $1.5 \cdot 10^{-3} \text{ mm.s}^{-1}$  with CPFDM-COMSOL: (a) crack initiation, (b) crack propagation, (c) final failure and (d) thin section in natural light.

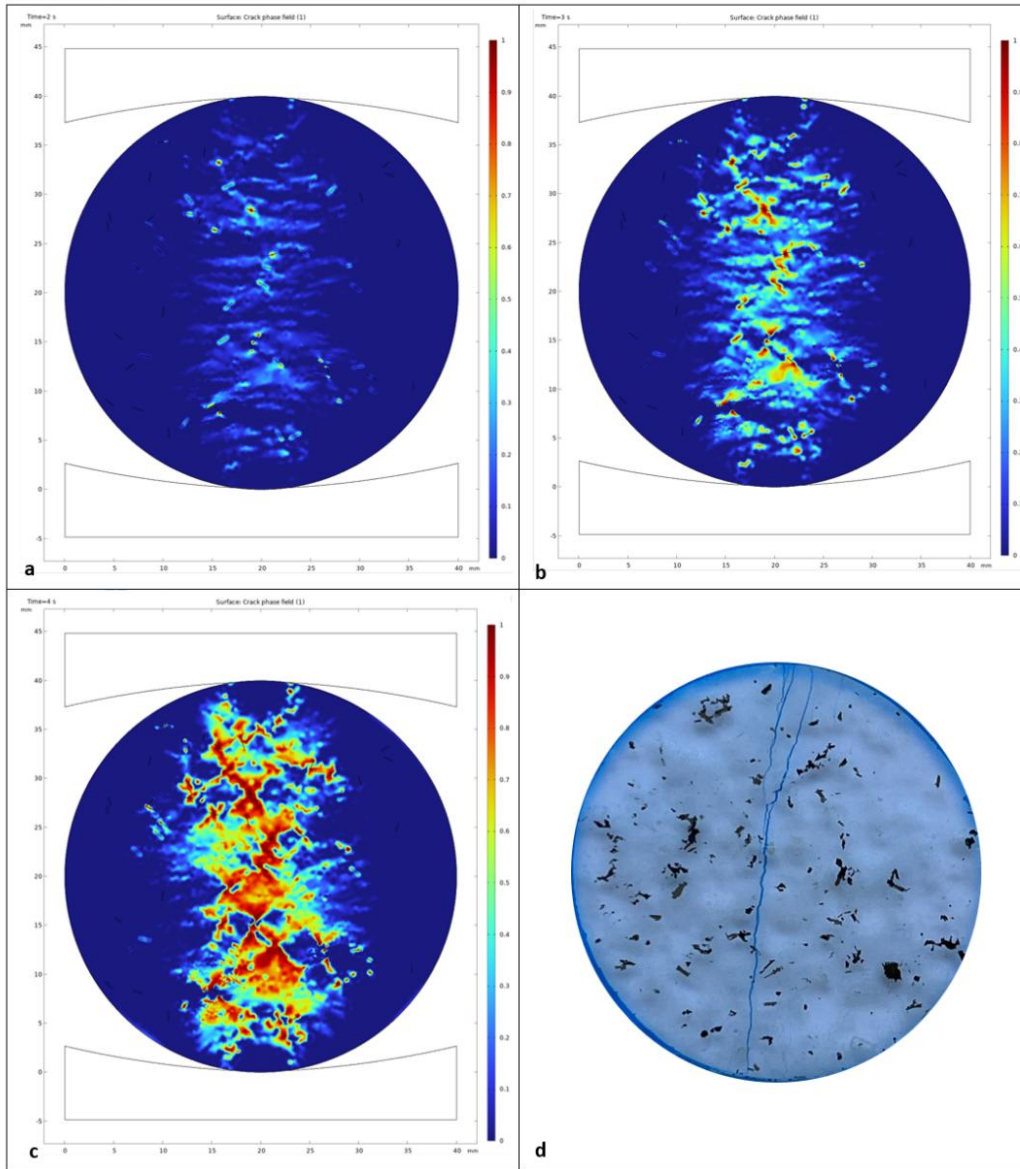


Figure 44: STS test modelling of displacement rate  $1.5 \cdot 10^{-2} \text{ mm.s}^{-1}$  with CPFDM-COMSOL (a) Crack initiation, (b) Crack propagation, (c) final failure and (d) Thin section in natural light.

### 3.2.2 STS simulation with VGBM-RS2

In each stage of the STS test, vertical displacement increments of  $1.5 \cdot 10^{-3}$  mm were applied. The corresponding reaction force was recorded at each stage. Figure 45 visually presents the outcome of the numerical STS test.

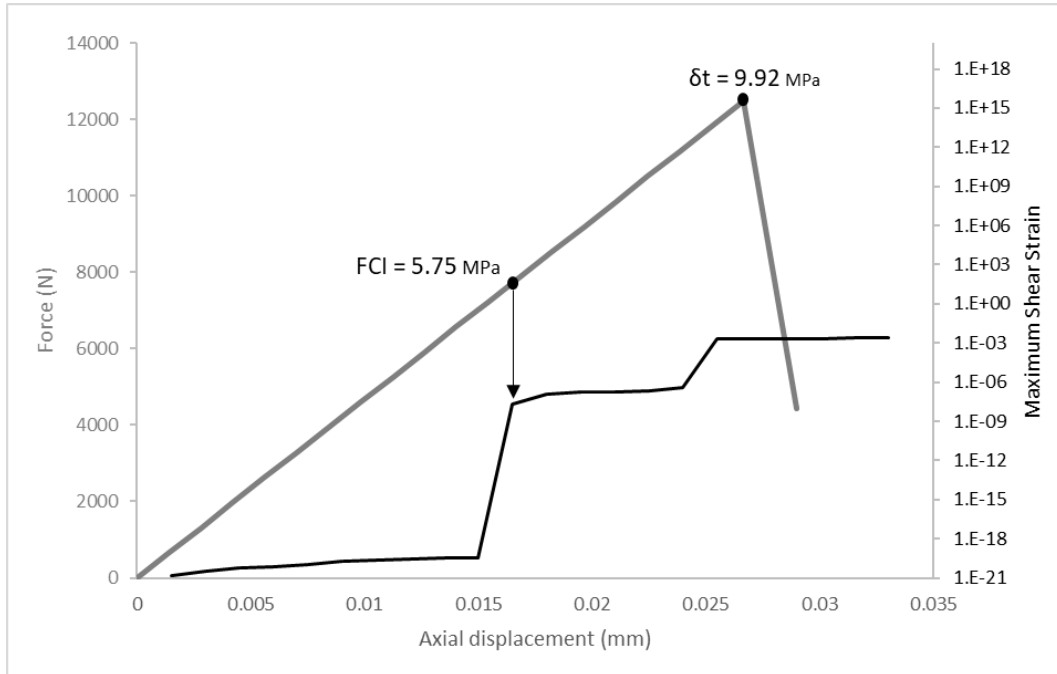


Figure 45: STS test simulation from VGBM-RS2.

Figure 46 illustrates the specific failure mode, characterised by a fracture occurring at the central region of the sample. The model effectively captures the brittle behaviour associated with the STS test, replicating the observed tendencies of Padang granite TG34 to fracture under tensile loading conditions. In terms of quantitative accuracy, the VGBM prediction of tensile strength is noteworthy. The model's calculated tensile strength closely aligns with the laboratory average, deviating by less than 2 % from the observed value.

The successful representation of the failure mode, the observation of brittle behaviour, and the close prediction of tensile strength substantiate the VGBM capability to emulate key aspects of the STS test. These results not only demonstrate the model's ability to capture specific material responses but also underscore its utility in providing meaningful and accurate insights into the behaviour of Padang granite TG34 in various loading scenarios and thus prediction.

Figure 46 visually captures the phenomenon of progressive damage occurring at different stages of the STS test.

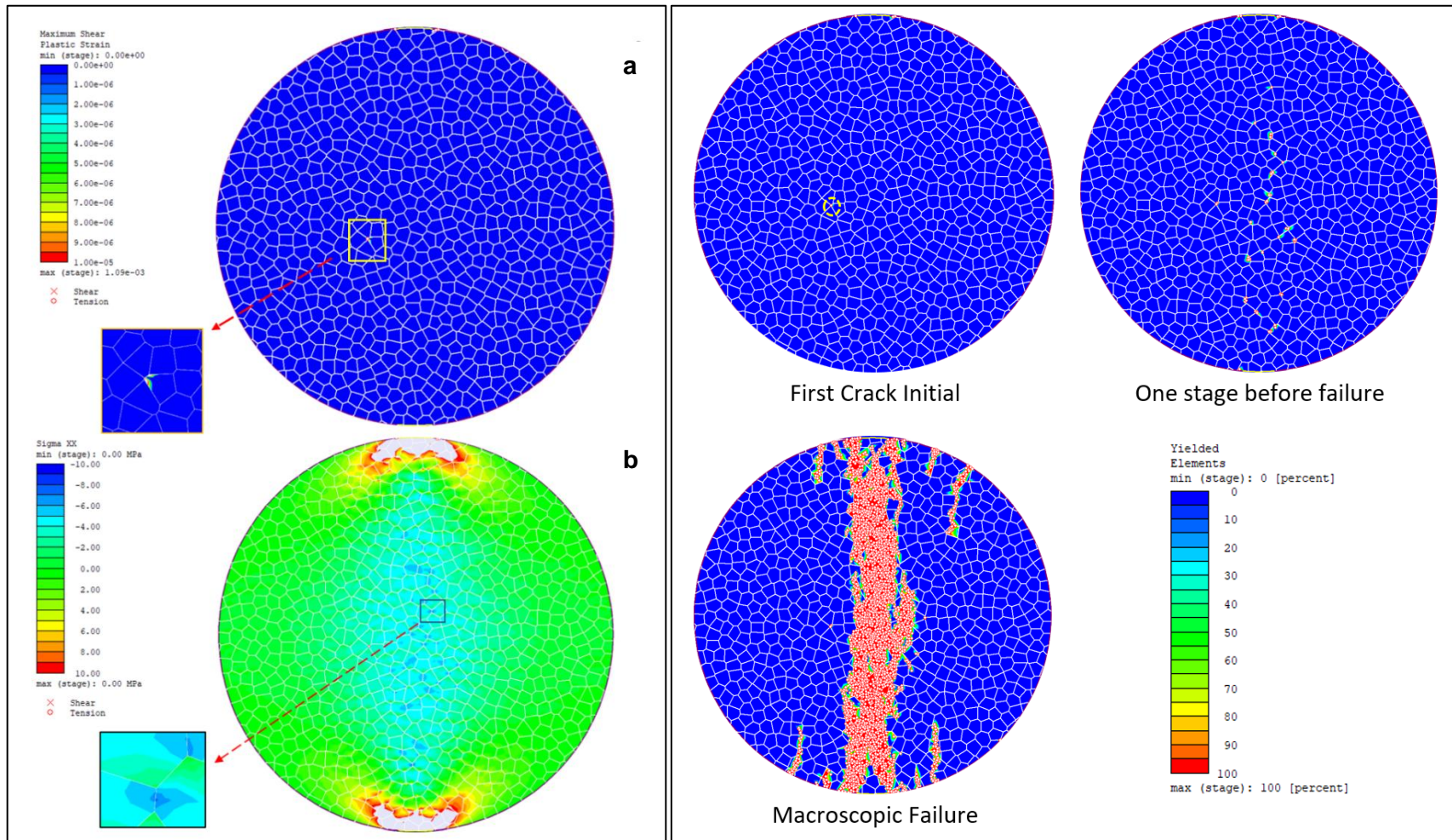


Figure 46: Progressive failure of VGBMs of Padang granite TG34 intact rock under STS test. (a) Maximum shear strain and (b) stress in xx direction or tensile stress at first crack initial stage (left) and different stages of failure (right).



## 4. A priori-simulation of experiments

To evaluate the performance and prediction accuracy of CPFDM-COMSOL and VGBM-RS2 under various boundary conditions, uniaxial and triaxial tests were simulated. The VGBM-RS2 model is capable of simulating both uniaxial compressive strength (UCS) and triaxial compressive strength (TCS) tests by altering the boundary conditions between the loading plate and the rock sample.

The triaxial tests, subjected to effective lateral pressures of 3, 5, and 9 MPa, respectively, were simulated using two methods, CPFDM-COMSOL and VGBM-RS2. In model CPFDM-COMSOL, the tests were performed with a pore pressure of 6 MPa and loading rates of  $1 \cdot 10^{-5}$  and  $1 \cdot 10^{-3} \text{ s}^{-1}$ . In model VGBM-RS2, the tests were conducted with a loading rate of  $1 \cdot 10^{-4} \text{ s}^{-1}$  at dry conditions with graphite powder as lubricant in contact. In all simulations, the properties and calibrated parameters of the base model were used, with only the boundary conditions being modified.

### 4.1 Overview of end friction effect on mechanical laboratory tests

In theory, UCS testing should involve applying a uniform uniaxial stress field to the test specimen. However, this ideal condition is never achieved due to the constraints imposed by the loading platens on the specimen ends. Experimentally, it has long been observed that the entire specimen under uniaxial compression does not fail simultaneously. This observation has prompted many researchers to seek analytical solutions for the stress distribution within the specimen while it is in an elastic state [2].

The impact of testing methodologies was subsequently examined by Kotsovos [44] through experiments conducted on cubes and cylinders of uniform dimensions. He hypothesized that the post-peak behaviour of a specimen is influenced by the restraint imposed by loading platens at the specimen's top and bottom. His findings indicated that the sample could be segmented into two distinct zones based on the stress state during testing:

- (i) an end zone near the loading platen where the lateral restraint of the platen induces a triaxial compression zone, and
- (ii) a central zone characterised by uniaxial compressive loading.

This conceptual division is illustrated schematically in Figure 47. Kotsovos [44] highlighted the significance of friction at the interface, substantiating his explanation with experimental data from tests using high-friction (steel platens) and low-friction (Teflon-treated platens) interfaces. The value  $E_p$  represents the Young's modulus of the loading platens at the top and bottom edges of the specimen. A higher  $E_p$  value indicates stiffer platens, whereas a lower value indicates softer platens. The ratio  $E_p/E_s$  compares the Young's modulus of the platen to that of the specimen. Due to the elastic mismatch between the platen and the specimen, their lateral deformations differ. This difference creates friction at the interface between the platen and the specimen. If  $E_p/E_s > 1$ , indicating stiffer platens (as shown in Figure 47c), this friction generates confining compressive stress at the specimen ends. Conversely, if  $E_p/E_s < 1$ , indicating softer platens (as shown in Figure 47b), it results in lateral tensile stress at the specimen ends.

These stresses are maximal at the specimen ends and decrease towards the centre. Consequently, with stiffer platens, two compression zones form at the specimen ends, leading to fewer fractures in these areas. With softer platens, two tension zones develop, resulting in more fractures and a clear splitting failure mode.

Since the axial stress field in the specimen is not uniformly distributed, radial tension particularly develops near the middle part of the specimen under stiffer constraints. This can cause a layer in this region to buckle outward, leading to lateral tension failure. This layer is thicker in the middle and thins towards the ends, reflecting the shape of the two compression cones at the ends. In contrast, the situation with softer constraints is entirely different [74].

The uneven stress distribution will lead to a deviation of the measured UCS from its intrinsic material property, which will bring adverse effects on the accurate measurement of granite specimen parameters and the study of the rock failure mechanism. Therefore, many studies have been conducted on the effect of friction between the loading plate and specimen such as soil, concrete, and rock [16]; [21]; [45]; [46] and [94]. More importantly, the end effect usually becomes more significant when the specimen is squatter (height/width < 2) [8]; [85].

Haimson and Chang [32], He et al. [34], Shen & Chen [74], Sheng et al. [75] and Zipf [100] have focused on the effect of cross-sectional shape. Hoop tension, induced by the geometry of a cylindrical specimen under compression (Figure 47a), can influence crack propagation and, consequently, the strengths of rocks in both laboratory and in-situ conditions. Although hoop tension also exists in square prism specimens, the tension is less pronounced compared to cylindrical specimens due to the difference in shape.

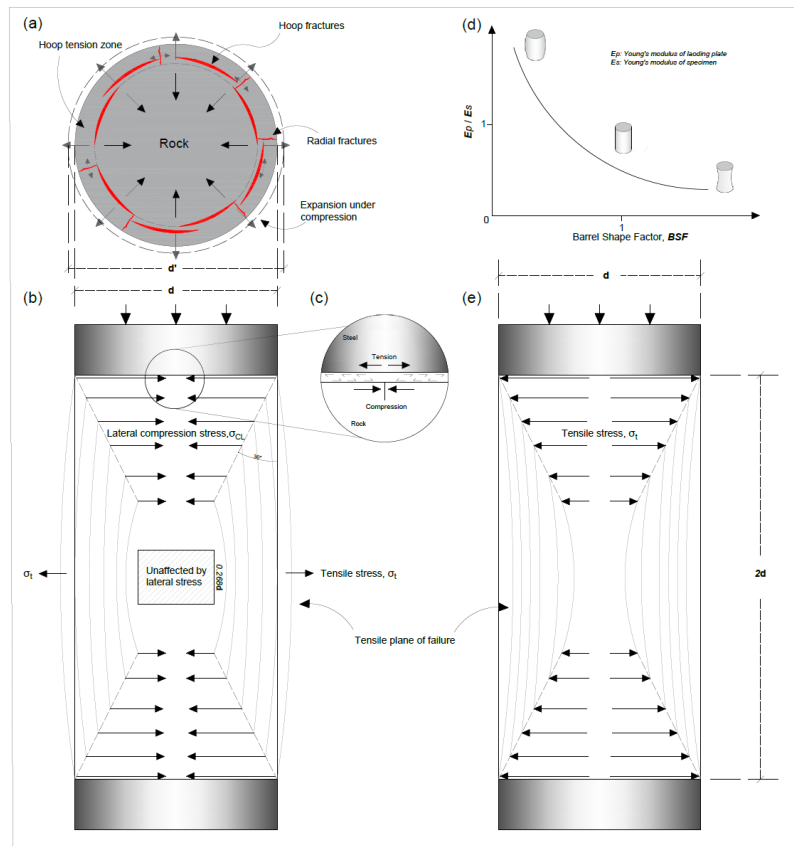


Figure 47: Illustration of confined zones due to frictional end effects in specimens in rock UCS: (a) hoop stress in upper surface of specimen, (b) high friction contact, (c) low friction contact [81]; [82], (d) end friction effect BSF and (e) UCS with no friction effect.

## 4.2 End friction effect simulation with VGBM-RS2

Modelling was done for three types of lubricants including graphite powder, thick Teflon (0.5 mm) and thin Teflon (0.025 mm). These lubricants were considered as a separate layer between the loading steel piston and the granite specimen. The physical and mechanical characteristics of the lubricants are presented in Table 15. The coefficients of friction between the granite specimen and the loading pistons, and between the granite specimen and Teflon sheet, used for modelling UCS and TCS tests, were derived from experimental results in Feng [26] and are presented in Table 16.

Table 15: Physical and mechanical properties of lubricants [33]  
([https://catalog.wshampshire.com/asset/psg\\_teflon\\_ptfe.pdf](https://catalog.wshampshire.com/asset/psg_teflon_ptfe.pdf)).

Type	Properties	Used in models
Graphite powder	$E$ : 8 - 15 (GPa)	$E$ : 10 (GPa)
	$\nu$ : NA (-)	$\nu$ : 0.1 (-)
	$\rho$ : 1.3-1.5 (g/cm <sup>3</sup> )	$\rho$ : 1.3 (g/cm <sup>3</sup> )
Teflon sheet	$E$ : 1 –5 (GPa)	$E$ : 3 (GPa)
	$\nu$ : 0.35- 0.45 (-)	$\nu$ : 0.4 (-)
	$\rho$ : 2.0 – 2.3 (g/cm <sup>3</sup> )	$\rho$ : 2.2 (g/cm <sup>3</sup> )

Table 16: Applied friction coefficients at specimen's end faces.

Type	Friction coefficient ( $\mu$ )	Used in model
Granite and steel	0.15	$K_n$ : $1 \cdot 10^{10}$ (MPa/m)
		$K_s$ : $1.5 \cdot 10^9$ (MPa/m)
		$\mu = K_s/K_n$ : 0.15 (-)
Granite and Teflon sheet	0.05	$K_n$ : $1 \cdot 10^{10}$ (MPa/m)
		$K_s$ : $5 \cdot 10^8$ (MPa/m)
		$\mu = K_s/K_n$ : 0.05 (-)
Granite and graphite powder	NA	$K_n$ : $1 \cdot 10^{15}$ (MPa/m)
		$K_s$ : $1 \cdot 10^6$ (MPa/m)
		$\mu = K_s/K_n$ : $10^{-9}$ (-)

A significant observation is the influence of end friction on strength. Notably, specimens tested with Teflon sheet demonstrate the lowest strength values compared to those tested with graphite powder in agreement with experimental observations (Table 17 and Figure 48). These results highlight the distinct effect of different lubricants on uniaxial compressive strength. The use of graphite powder results in a strength increase of approximately 4.2 % compared to tests without lubricant. Conversely, employing Teflon as a lubricant lead to a decrease in strength of approximately 6.8 to 8.9 %. Accordingly, considering end face friction in numerical simulations is key to properly simulate strength results from experiments.

The stress-strain-relations depicted in Figure 48 show that Poisson's ratios and Young's moduli in the elastic stress range are not affected by the choice of the lubricant. However,



Young's modulus is particularly hard to experimentally determine when using low-stiffness lubricants that contribute to measured bulk axial strain due to the non-linear plastic deformation. Deformation characteristics in the inelastic regime are significantly affected by the choice of the lubricant. The differences are particularly visible for lateral strains at axial stresses exceeding approximately 120 MPa, when lateral strains are largest for Teflon 0.5 mm at equivalent axial stresses, while axial strains are similar for the different lubricants.

Table 17: Comparison of numerical and experimental results for uniaxial compressive strength tests with different lubricants.

Macro-parameters	Laboratory result	Simulation result	Accuracy (%)
Young's Modulus (GPa)	55 ±3	55	100
Poisson's ratio (-)	0.36 ±0.04	0.33	92
UCS (MPa) at ( $1 \cdot 10^{-4} \text{ s}^{-1}$ )	Without lubricant	216 ±28	100
	Graphite powder	243	100
	Teflon 0.5 mm	191	95
	Teflon 0.025 mm	209	99

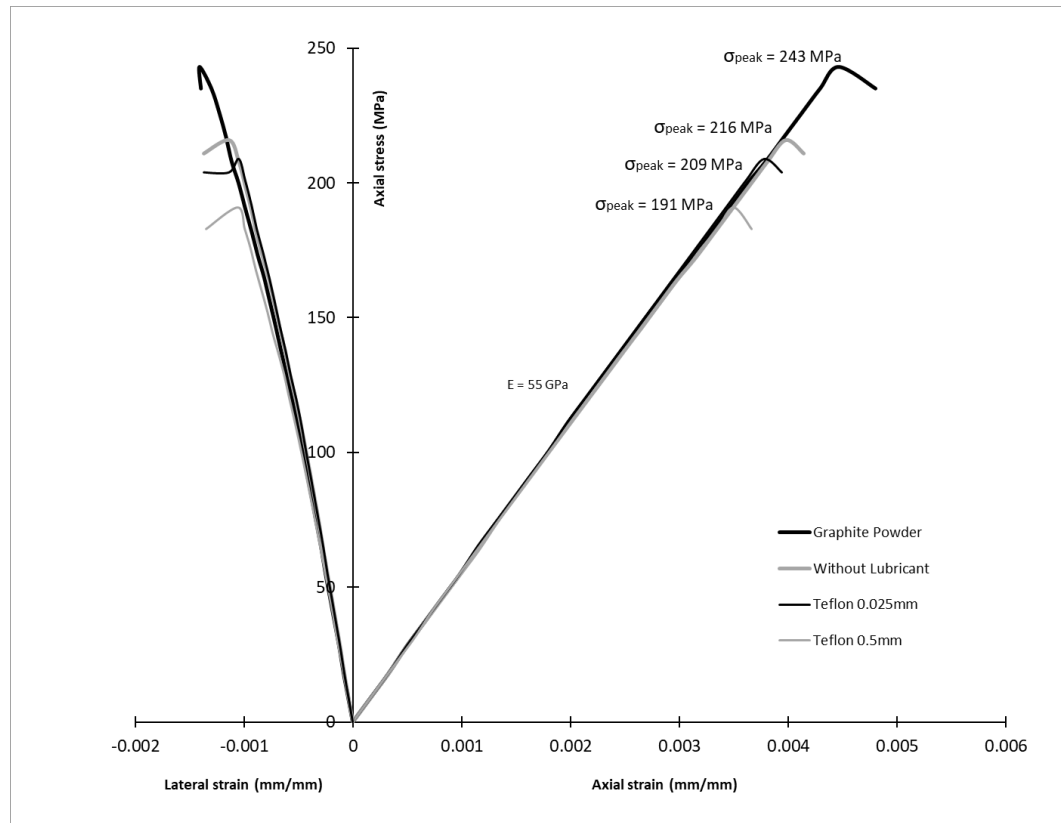


Figure 48: Result of numerical simulation of UCS tests without and with different lubricants.

The effect of friction can be quantified by the Barrel Shape Factor (BSF) according to Bolk [11] describing the ratio of average radial strain at the specimen's end faces to the radial strain at the centre of the specimen (Figure 47d). The BSF for specimens simulated

without lubricant is lowest, i.e., the radial end face deformation is low compared to the radial deformation at the centre of the specimen (Table 18). Interestingly, the two thicknesses of Teflon yield different results, mainly due to the contribution of lateral end face deformation, i.e., lateral end face deformation for Teflon 0.5 mm is about 10 times larger than for Teflon 0.025 mm, pointing to the suspected tensile stress contribution at specimen end faces and/or to a numerical artefact in which the lateral deformation of the Teflon layer pulls the edges of the specimen's end faces, so that the interpolation of lateral strains is miscalculated. Apart from Teflon 0.5 mm, graphite powder produced the highest BSF of the uniformly deforming specimens (Figure 49 and Table 18).

Table 18: Numerical results for radial (lateral) strains at failure base on Barrel shape factor.

Strain	Graphite powder	Teflon 0.5 mm	Teflon 0.025 mm	no lubricant
$(\varepsilon_{r,top} + \varepsilon_{r,bottom})/2$	$0.858 \cdot 10^{-3}$	$1.488 \cdot 10^{-3}$	$0.140 \cdot 10^{-3}$	$0.116 \cdot 10^{-3}$
$\varepsilon_{r,centre}$	$1.554 \cdot 10^{-3}$	$1.092 \cdot 10^{-3}$	$1.242 \cdot 10^{-3}$	$1.344 \cdot 10^{-3}$
BSF	0.55	1.36	0.11	0.087



Figure 49: Specimen length vs lateral displacement of UCS test modelling without and with different lubricants.

In the previous section, it is described that it is generally assumed that the central zone of a slender specimen in uniaxial compressive loading is subjected to a uniform uniaxial stress state and at the top and bottom of the cylinder, a cone-like region will be formed. This region experiences compressive stress when there is friction between the loading plate and the specimen, and tensile stress when there is low friction (Figure 47). Figure 50 shows that if the interface between rock and loading steel plate is equipped with a lubricant layer, tensile zones can develop. Moreover, the development of a compressive stress cone at the top and bottom of the specimen is less intense when lubricants are used, leading to a more homogeneous stress distribution within the sample in agreement with previously published studies [15]; [36] and [82].

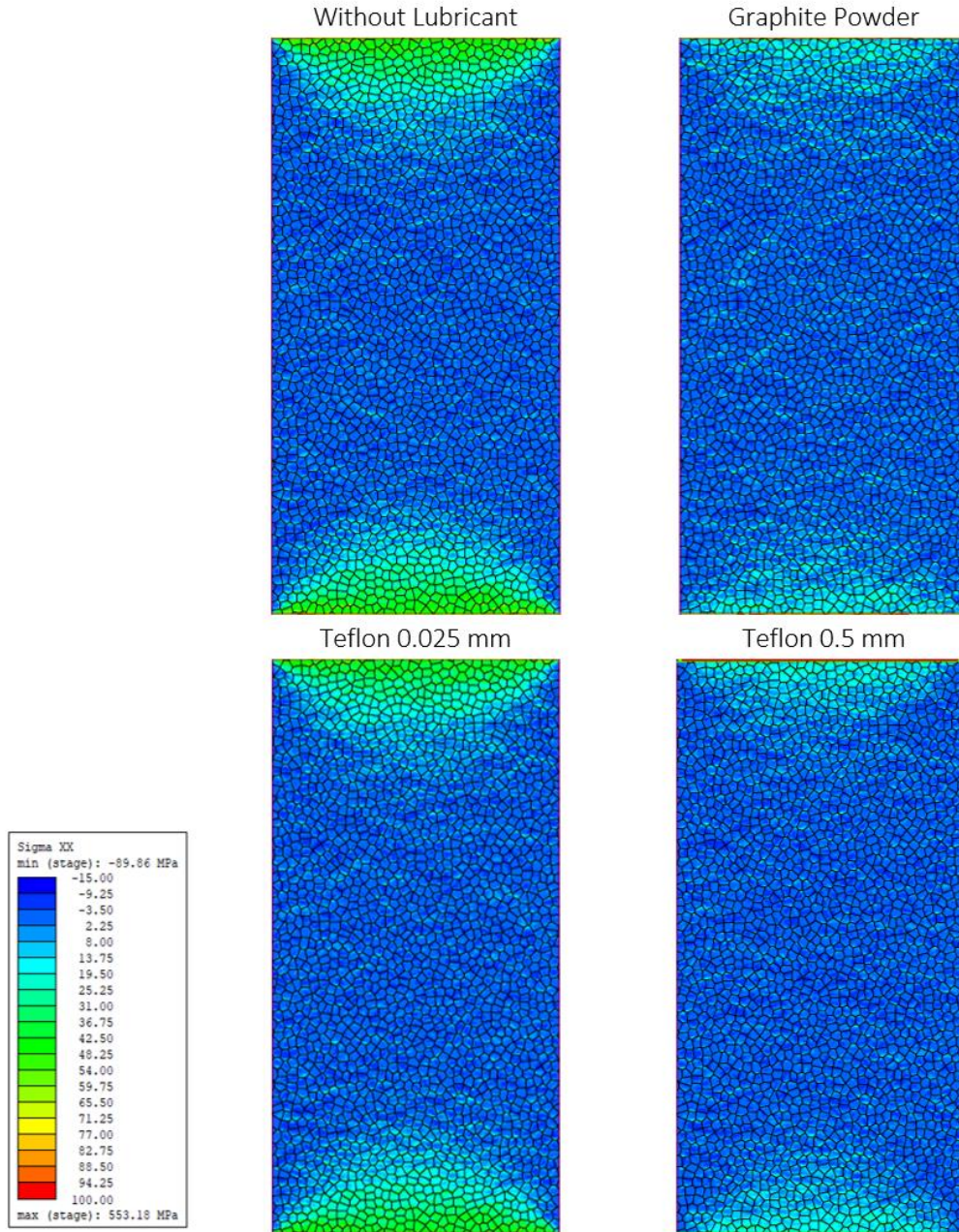


Figure 50: Lateral tensile and compressional stress in UCS model without and with different lubricants in VGBM-RS2.

Figure 51 presents a comparison of numerical simulation results for the VGBM-RS2 under three conditions: without lubricant, with Teflon, and with graphite powder, against a laboratory specimen during failure. Figure 51a illustrates two main fractures along with several smaller, relatively symmetrical fractures in both the model and the laboratory specimen. These main fractures are more dispersed in the centre and at the sides of the specimen, indicating lateral expansion of the specimen's central section. The shear strain magnitudes in both main fractures are approximately equal and amount to about 0.02. These fractures are entirely located within the shear stress concentration zone, and the formation of intersecting joints demonstrates the shear-tensile behaviour of the model. The fracture pattern observed in both the model and the laboratory specimen agree well (Figure 51a and Figure 51b).

The propagation of fractures in the uniaxial test with a Teflon layer as a lubricant is observed only on one side of the sample. This indicates a reduction in tensile forces in the centre of the sample during failure (Figure 51e and Figure 51f).

As illustrated in Figure 51i and Figure 51j, the presence of graphite powder as a lubricant has a pronounced effect on both the laboratory and simulation results. The stress concentration within the sample leads to the formation of a primary fracture with a shearing mechanism at the boundary where tensile shear stress transitions into the tensile cone. In the model, the shear strain value at this fracture is measured to be 0.4.

The formation and magnitude of hoop stress on the upper surface of the laboratory sample and at the point of contact between the sample and the loading plate in the model are depicted in Figure 51. As shown in Figure 51c and Figure 51d, tangential stress in the upper part of the sample without lubricant has led to ring form fractures in both the model and the laboratory sample. However, at the contact surface with graphite powder, due to the absence of hoop strain, the upper surface remains completely intact and unbroken (Figure 51k). On the surface with Teflon as a lubricant (Figure 51h), the hoop stress decreased compared to the normal state, causing only a limited fracture on one side of the cross-section edge in the laboratory sample (Figure 51g). The VGBM simulated vertical fractures caused by the effect of Hoop stress as a minor principal strain concentration at the upper area of the specimen (Figure 51d for test without lubricants, Figure 51h for test with Teflon and Figure 51l for test with graphite powder).

The numerical stress-strain-relations agree fairly well with the experimental for the setup without lubricant (Figure 52), with graphite powder (Figure 53), and with Teflon 0.025 mm (Figure 54). The experimental stress-strain-relations for Teflon 0.5 mm cannot be used due to the hard-to-calibrate contribution to axial strain from the thick Teflon sheet at both end faces.



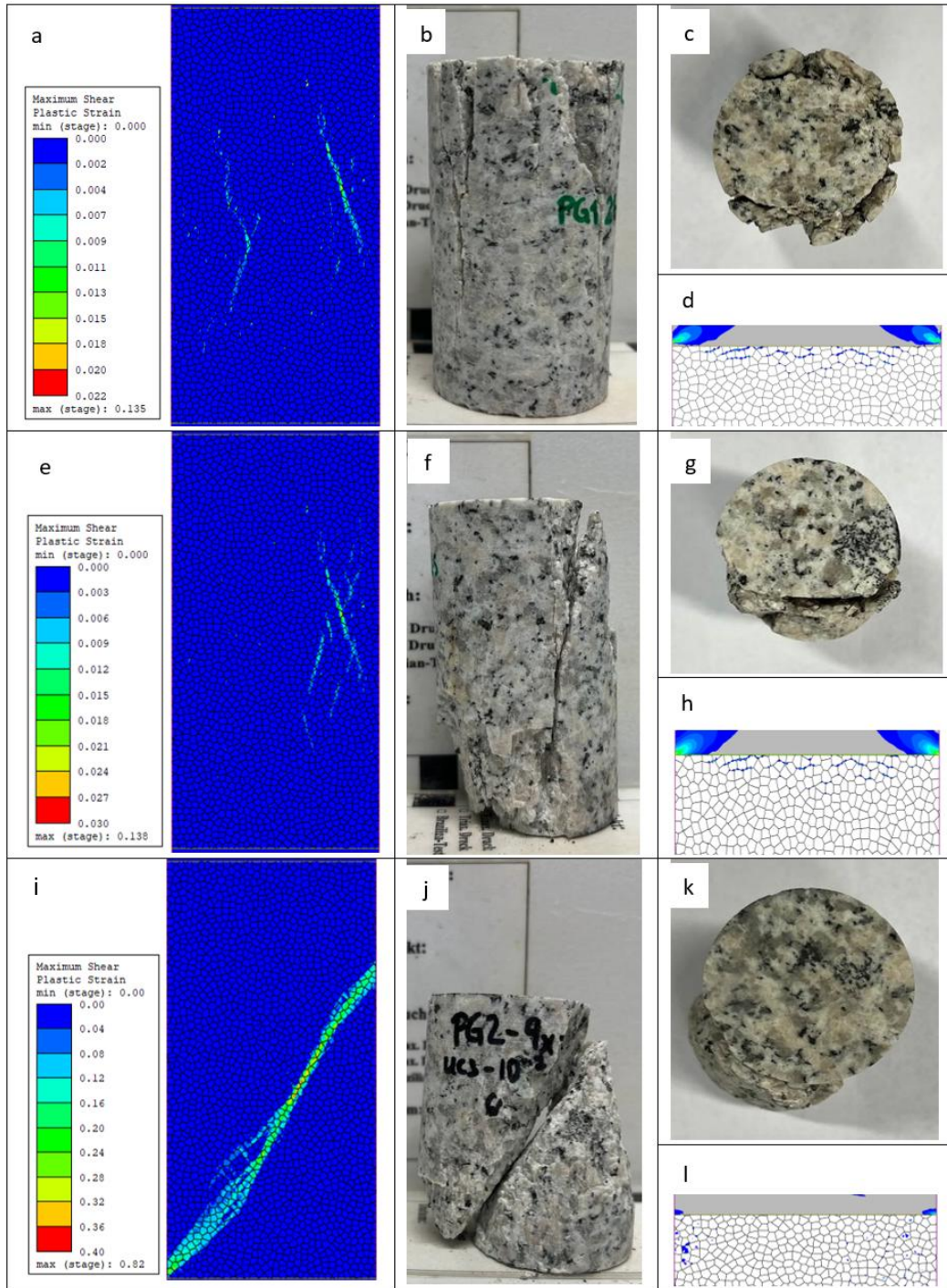


Figure 51: Failure modes under unconfined compression in VGBM-RS2 and laboratory: (a-d) without lubricant, (e-h) with Teflon 0.025 mm, (i-l) with graphite powder; (d, h & l) represent minor principal strain in the upper part of the sample and they are scaled between 0 to 0.001. Legend refers only to a, e, i.

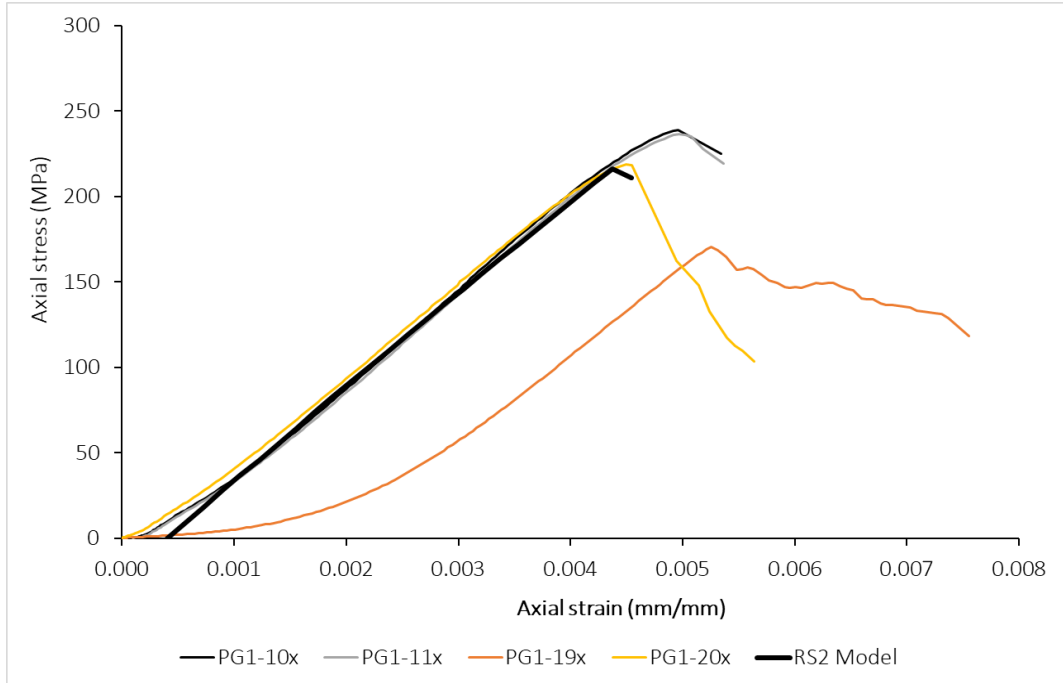


Figure 52: Stress-strain-relations of UCS tests in experiments and simulated with VGBM-RS2 without lubricant.

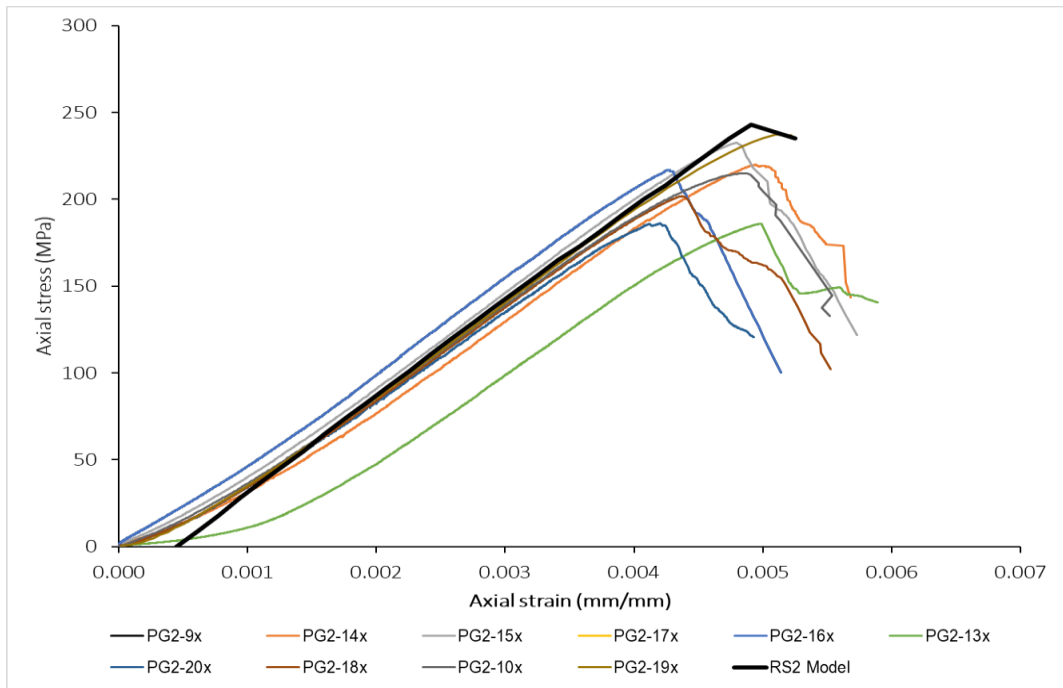


Figure 53: Stress-strain-relations of UCS tests in experiments and simulated with VGBM-RS2 with graphite powder.

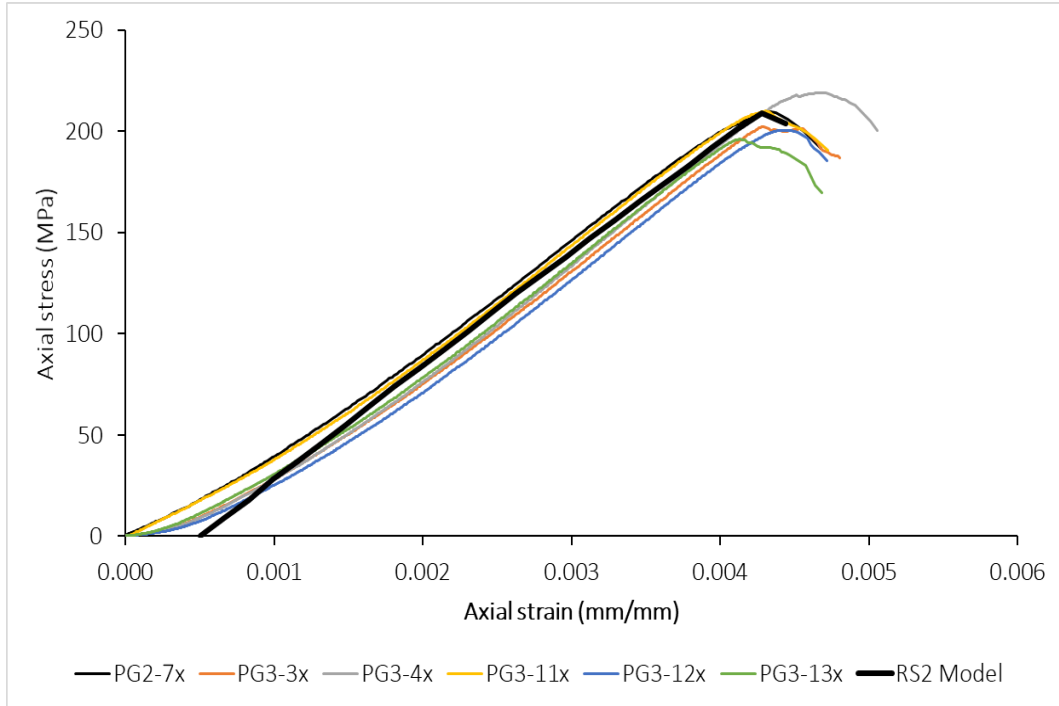


Figure 54: Stress-strain-relations of UCS tests in experiments and simulated with VGBM-RS2 with Teflon 0.025 mm.

### 4.3 Triaxial compressive strength test simulation with CPFDM-COMSOL

In this model, similar to the UCS test model (Figure 26), a vertical displacement is applied to the top of the sample, and confinement pressure is applied by a load boundary to all sides of the sample. This setup allows the study of the specimen's static response and peak stress at the failure stage under various confinement pressures. The material behaviour is modelled using the linear elastic model and phase field damage approach. Effective confining stresses of 3, 5, and 9 MPa, respectively, are applied, and deformation is simulated for a strain rate of  $1 \cdot 10^{-5} \text{ s}^{-1}$ . Additionally, an external stress node was used to apply a 6 MPa pore pressure, i.e., confining pressure was applied with 9, 11, and 15 MPa. In Figure 55, the simulation results of the triaxial test at a strain rate of  $1 \cdot 10^{-5} \text{ s}^{-1}$  are compared to laboratory tested specimen. As seen in Figure 55 the increase in lateral pressure from 3 to 5 MPa results in more micro fractures propagating vertically. The results of the triaxial numerical models and experimental tests are presented in Table 19. Figure 56 demonstrates that the CPFDM-COMSOL effectively models the increase in peak strength with elevated confining pressure. Notably, all parameters of phase field damage and material remained consistent across all tests. The envelope presented aligns with those obtained from laboratory tests up to a confining stress of 9 MPa (Figure 57).

Table 19: Comparison of numerical and experimental results for TCS tests under strain rate  $1 \cdot 10^{-5} \text{ s}^{-1}$ .

Strain rate ( $\text{s}^{-1}$ )	Effective confining pressure (MPa)	Average of laboratory test results (MPa)	Results of CPFDM (MPa)	Accuracy (%)
$1 \cdot 10^{-5}$	3	168	193	87
	5	188	205	92
	9	247	239	97

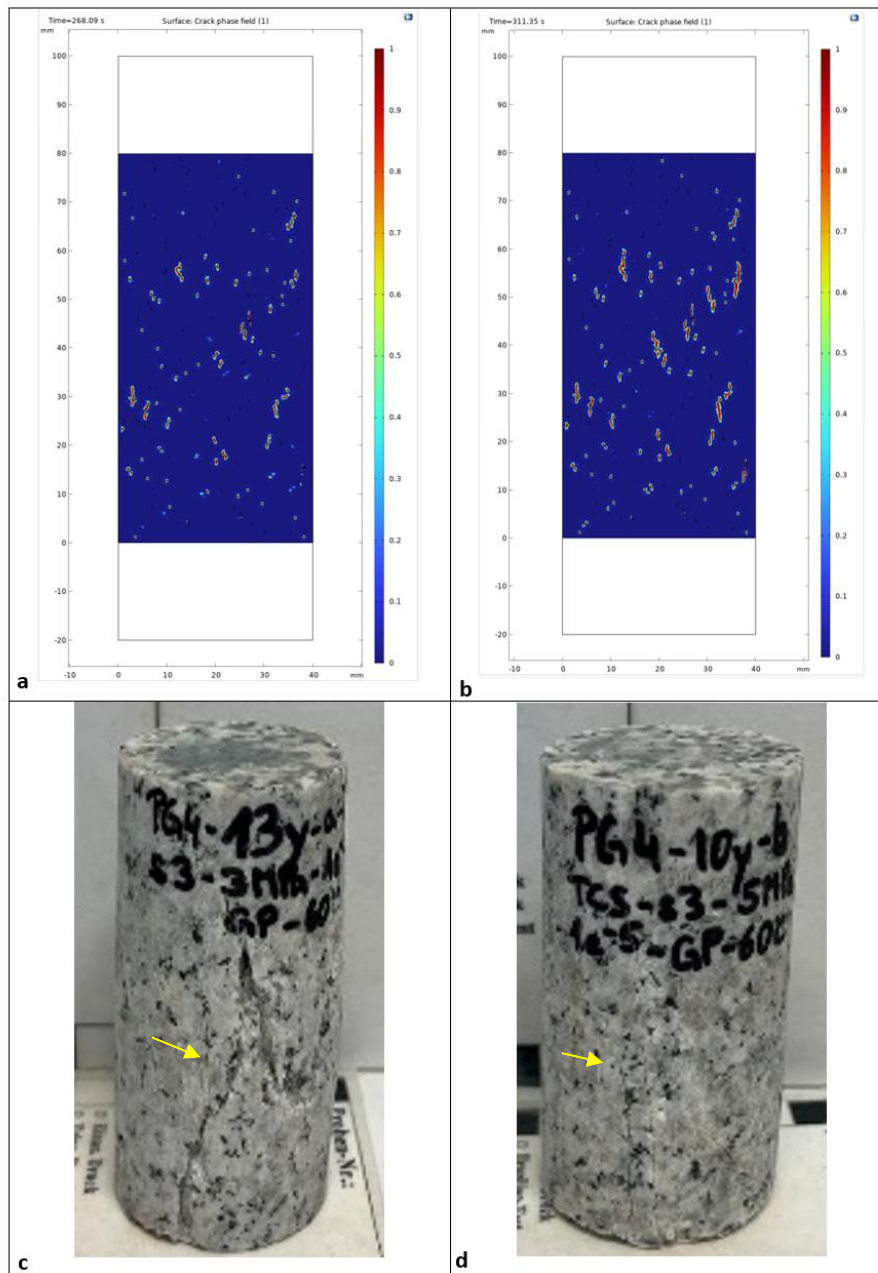


Figure 55: Fracture modes under triaxial compression with strain rate  $1 \cdot 10^{-5} \text{ s}^{-1}$  in CPFDM-COMSOL and laboratory: (a & c) diagonal micro fractures in triaxial test with 3 MPa confining pressure (b & d) vertical micro fractures in triaxial test with 5 MPa confining pressure.



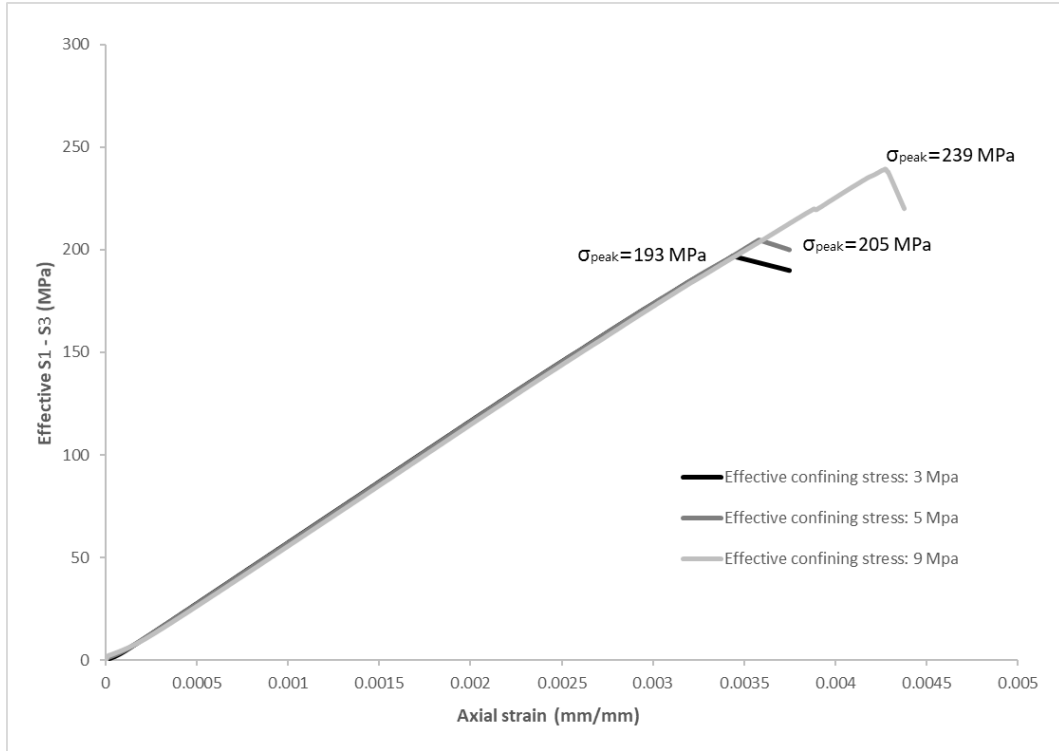


Figure 56: Result of numerical simulation of TCS tests under strain rate  $1 \cdot 10^{-5} \text{ s}^{-1}$  with 6 MPa pore pressure.

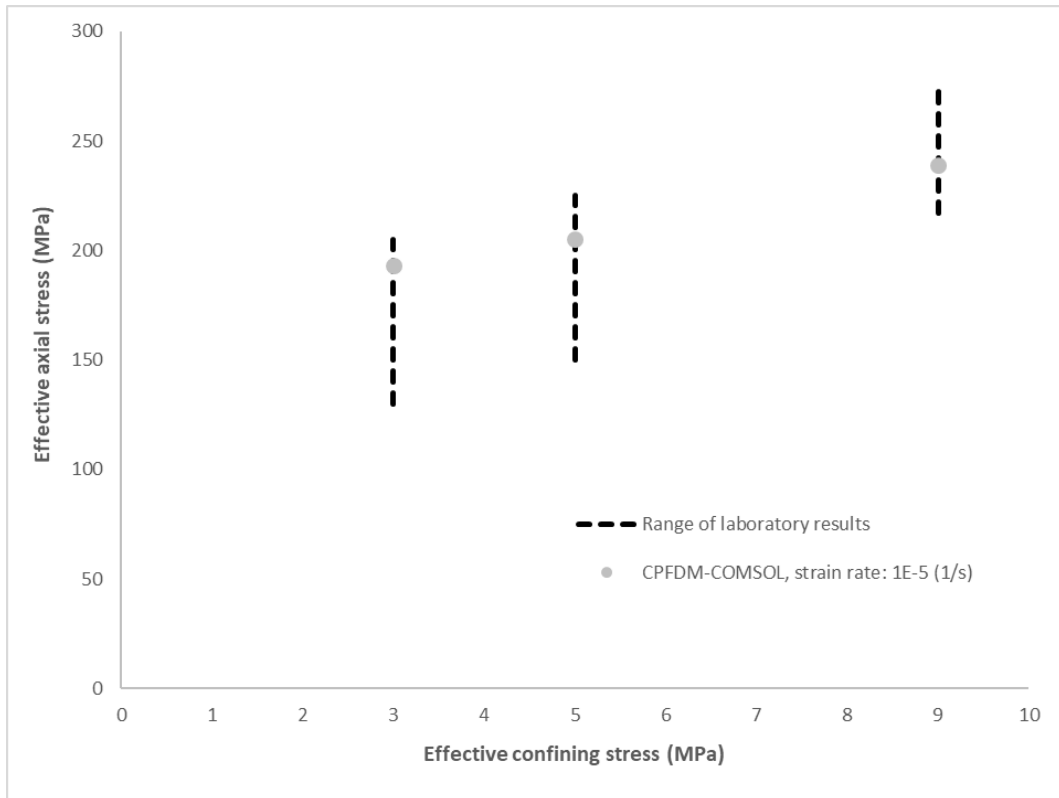


Figure 57: Comparing laboratory results of TCS tests with strain rate  $1 \cdot 10^{-5} \text{ s}^{-1}$  under 6 MPa pore pressure in experiments and simulated with CPFDM-COMSOL

## 4.4 Triaxial compressive test simulation with VGBM-RS2

The numerical model for the triaxial test with graphite powder as lubricant by VGBM was conducted by applying three confining pressures: 3, 5 and 9 MPa. The model's configuration mirrored that used for the UCS test (Figure 26). The analysis was divided into several stationary stages, with the first stage dedicated to applying hydrostatic pressure, followed by the application of deviatoric stress in subsequent stages via vertical displacement imposed on the upper platen. It is important to note that  $1 \cdot 10^{-4}$  axial strain rate increments were used during the next stages.

The results of the triaxial tests are presented in Figure 58 and that demonstrates that the VGBM-RS2 effectively models the increase in peak strength with elevated confining pressure. Notably, all micro parameters of grain and grain boundary remained consistent across all tests. The envelope presented aligns with those obtained from laboratory tests up to a confining stress of 9 MPa. However, at lower confining stresses, the rock strength is overestimated (Figure 59). Results of TCS tests simulation are presented in Table 20.

Table 20: Comparison of numerical and experimental results for TCS tests under strain rate  $1 \cdot 10^{-4} \text{ s}^{-1}$  with graphite powder as a lubricant.

Strain rate ( $\text{s}^{-1}$ )	Confining pressure (MPa)	Average of laboratory test results (MPa)	Results of VGBM (MPa)	Accuracy (%)
$1 \cdot 10^{-4}$	3	257	281	91
	5	290	291	99
	9	325	310	95

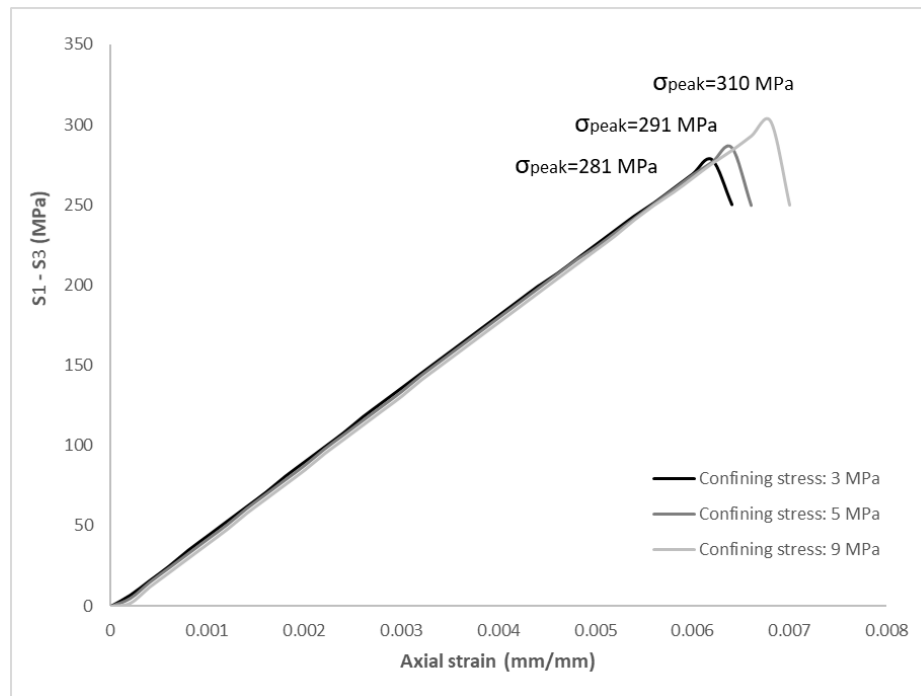


Figure 58: Results of numerical simulation of TCS tests under strain rate  $1 \cdot 10^{-4} \text{ s}^{-1}$  with graphite powder as a lubricant.

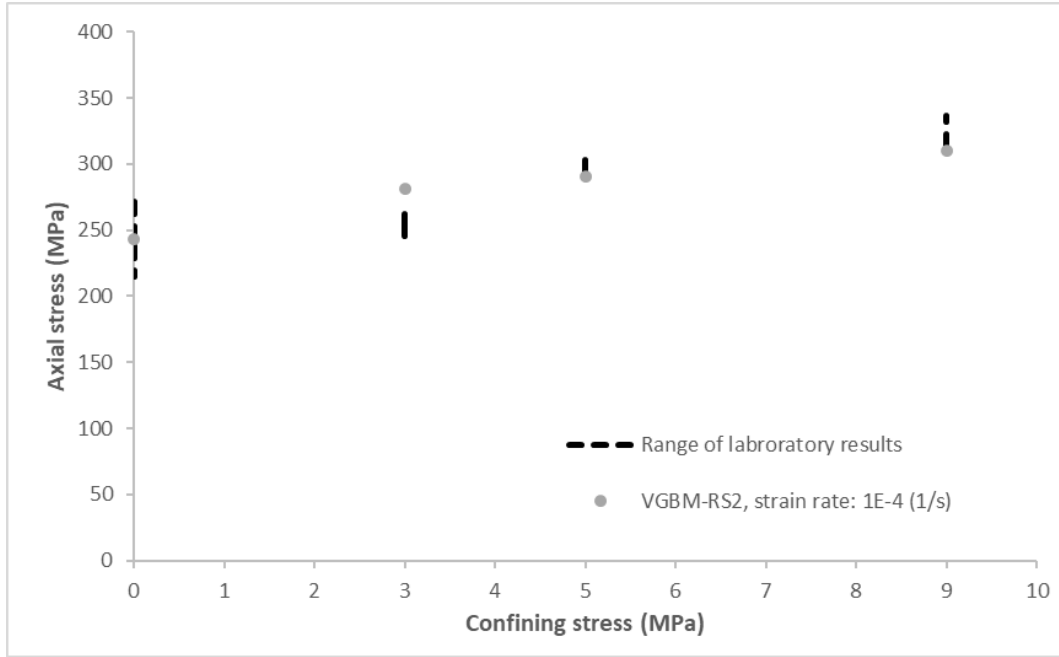


Figure 59: Comparing laboratory results TCS tests with graphite powder as a lubricant in experiments and simulated with VGBM-RS2.

## 4.5 Accuracy of predictions

This study compares the results of UCS, STS, and TCS tests, which were averaged from experimental data, with the outcomes of two simulated models: the Voronoi grain-based model (VGBM) and the crack phase-field damage model (CPFDM). The findings are presented in Table 21, Table 22, Table 23 and Figure 60.

The chart shows that the simulation results for calibrated models (UCS with different strain rates) align very closely with the 1:1 line, indicating that both VGBM and CPFDM are highly effective in accurately simulating geomechanical processes. For predictive simulation models (TCS with different confining pressures and constant pore pressures using graphite powder as lubricant), the models performed well, with most results falling within a 10 % deviation range, except for one instance with an 87 % accuracy rate. This consistency demonstrates the reliability and precision of these models in simulation and prediction.

Table 21: Comparison of numerical and experimental results for STS tests.

Model	Displacement rate (mm.s <sup>-1</sup> )	Lab results Table 4 (MPa)	Simulation results (MPa)	Accuracy (%)
VGBM	$1.5 \cdot 10^{-3}$	$9.2 \pm 1.9$	9.9	93
	$1.5 \cdot 10^{-2}$	$11.1 \pm 1.7$	11.5	97
CPFDM	$1.5 \cdot 10^{-3}$	$9.2 \pm 1.9$	9.3	99
	$1.5 \cdot 10^{-4}$	$8.9 \pm 1.2$	8.4	94

Table 22: Comparison of numerical and experimental results for UCS tests.

Model & Strain rate ( $s^{-1}$ )		Lab results Table 5 (MPa)	Simulation results (MPa)	Accuracy (%)
VGBM $1 \cdot 10^{-4}$	Without lubricant	216 $\pm$ 28	216	100
	Graphite Powder	243 $\pm$ 18	243	100
	Teflon 0.5 mm	182 $\pm$ 12	191	95
	Teflon 0.025 mm	206 $\pm$ 8	209	99
CPFDM	$1 \cdot 10^{-3}$	258	255	99
	$1 \cdot 10^{-4}$	216 $\pm$ 28	231	94
	$1 \cdot 10^{-5}$	216 $\pm$ 7	214	99
	$1 \cdot 10^{-6}$	195 $\pm$ 15	204	96

Table 23: Comparison of numerical and experimental results for TCS tests under strain rate  $1 \cdot 10^{-4} s^{-1}$  with graphite powder as a lubricant by VGBM and strain rate  $1 \cdot 10^{-5} s^{-1}$  with 6 MPa pore pressure by CPFDM.

Model & Strain rate ( $s^{-1}$ )	(effective) confining pressure (MPa)	Lab results Table 7 (MPa)	Simulation results (MPa)	Accuracy (%)
VGBM $1 \cdot 10^{-4}$	3	257 $\pm$ 12	281	91
	5	295 $\pm$ 8	291	99
	9	325 $\pm$ 12	310	95
CPFDM $1 \cdot 10^{-5}$	3	168 $\pm$ 38	193	87
	5	188 $\pm$ 38	205	92
	9	247 $\pm$ 30	239	97

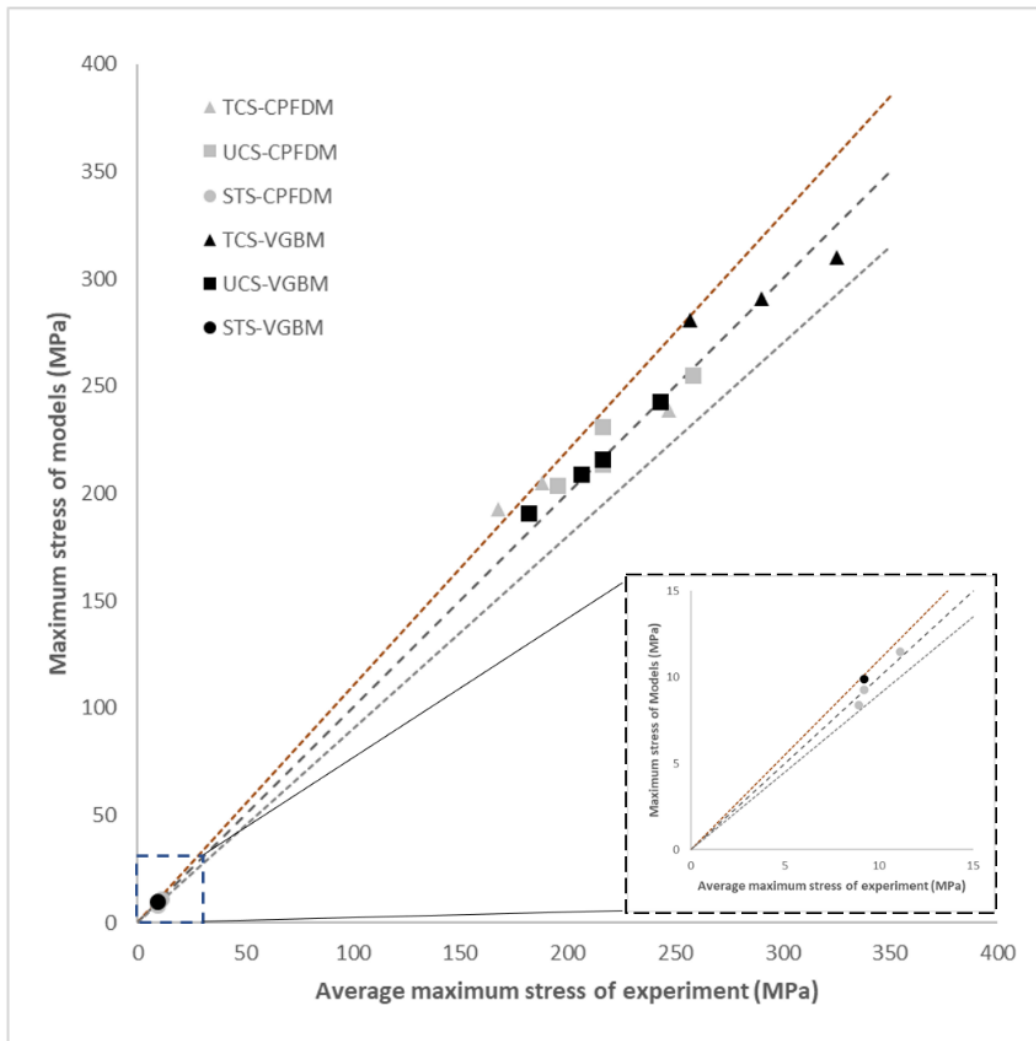


Figure 60: Comparing results from experiments and numerical simulations of geomechanical tests of Padang granite TG34.

# Workflow for benchmarking

The validation of numerical codes in the presented context consists of four processes as presented in Figure 61. The first part involves the generation of a comprehensive, laboratory database that reflects the engineering geological application and range of material properties on a small scale (A). The second part focuses on the numerical modelling of the experimental results complying with the boundary conditions of the basic laboratory tests (here UCS and STS tests). The results of the basic model will be compared with the experimental results (B). Subsequently, boundary conditions will be altered while maintaining material properties and physics from the basic model to predict the outcome (here alteration of confining and pore pressure for TCS). A verification of predictions through experimental findings allows for testing the validity on assumptions in A, e.g., on the physics of the model or microstructural simplifications (C). Interpretation and reporting of results shall be made in a final report (D).

- **A1:** Sample material is selected according to the research question. Generally, a benchmark laboratory dataset suitable for testing numerical codes for their predictive capabilities should minimize any uncertainties related to sample variability and specimen preparation. Particular attention should be paid to specimen preparation when investigating high strength and high stiffness rock material, such as granite, and in the context of geomechanical testing. Careful grinding of stress conducting surfaces of 2 h or more can be required to avoid stress concentrations altering the experimental outcome, potentially involving stricter compliance to requirements suggested in national and international standards and recommendations.

Sample selection and specimen preparation should consider any given or suspected anisotropy and should be carefully documented. Recommendations for documentation include:

- > Sample orientation
- > Specimen orientation and location in sample
- > Fluids, procedures and operators involved in sample preparation
- > Drying and/or storage procedure (duration, temperature)
- > Geometric dimensions of specimens
- > Macroscopically visible irregularities

- **A2:** Characterisation and testing of samples requires a quality control protocol that quantifies the sample and specimen variability, the reproducibility of experimental results and their experimental measurement uncertainties. The latter requires scheduled calibration procedures in defined intervals and an inspection of used measurement devices prior to testing.

The exact experimental setup must be documented including all parts of assemblies that potentially contribute to the experimental outcome. For example, specimen's end face treatment proved significant for numerical simulation of uniaxial compressive strength tests, requiring the model to include parts of the upper and lower piston.

Furthermore, the laboratory conditions should be documented. In particular, for time-dependent processes the contribution of laboratory conditions (temperature, humidity) to experimental results may be significant.

When temporal and spatial upscaling is relevant for the addressed research question in numerical simulations, these factors should be investigated in the laboratory schedule within the temporal and spatial limits of laboratory testing.

A documentation of the microstructural properties of investigate specimens, e.g., via computertomographic scans, thin sections, macroscopic description, is highly recommended to account for the inherently heterogeneous presentation of natural materials like rocks, whose effect on experimental results and relevance for numerical simulation may be significant depending on the code and research question to be addressed. To reproduce time-dependent mechanical properties of rocks, a consideration of microstructural properties proved necessary within this study.

- **B1:** For the setup of numerical simulations the model configuration should include both the geometric parameters of the laboratory equipment and the specimen dimensions, as the exact reproduction of the geometry is crucial for the accuracy of the simulation results. Specific material characteristics such as the mineral grain size (shape, size, frequency) and microcracks (length, orientation, frequency), which significantly influence the mechanical behaviour of the sample material, must also be considered.

In addition to basic physical properties such as density and porosity, mechanical properties such as Young's modulus and Poission`s ratio should be taken into account as input data considering experimental uncertainties and specimen variability/reproducibility. Failure criteria, such as Mohr Coulomb in displacement field and crack damage in phase field, must be adapted to describe the failure behaviour of the sample material.

- **B2:** In order to be able to simulate realistic scenarios, fixed boundary conditions, including displacement, fixed, rolling and free wheel conditions, must be defined. The initial conditions, here for example displacement rate, strain rate, pore and confining pressure should be adapted in accordance with the specified laboratory conditions.
- **B3:** A suitable mesh structure, which includes parameters such as mesh size, frequency, shape and number of nodes, has a significant influence on the quality, accuracy and efficiency of the simulation and should therefore be selected appropriately including a mesh sensitivity study.
- **B4:** When determining the analysis method, a distinction must be made between stationary and time-dependent analyses. The stationary simulation works with a fixed number of stages, while the time-dependent method takes into account the total duration of the simulation and the time intervals in which the results are analysed.
- **B5:** The basic model must be calibrated by comparing the simulation results with the laboratory data so that the accuracy of the simulation results are within experimental uncertainties. A sensitivity analysis of input parameters should be performed to understand and quantify their effects on the numerical outcome,

based on which a reasonable calibration within observed parameter ranges can be performed.

In the context of geomechanical testing and depending on the physics of the code it can be required to compare fracture and failure patterns in numerical simulation and experiment. Severe deviations from the failure patterns may point to fundamental problems in the physical basis of numerical simulations.

Physico-chemical interactions, if not explicitly simulated through chemomechanical coupling, should at least be accounted for by separately simulating and calibrating experiments under different physico-chemical environments, e.g., an individual calibration of oven-dried, humid or saturated samples.

- **C1:** Using the calibrated model, a prediction of the material behaviour under adjusted boundary conditions (e.g., confining and pore pressure) should be achieved while maintaining material properties and model physics.
- **C2:** The results from prediction should be verified with experimental results and evaluated with respect to experimental uncertainties and specimen variability/reproducibility. If the agreement is not within the range of experimental results, steps from B must be repeated. Only if the basic model calibration leads to a correct prediction while maintaining material properties and model physics, a predictive potential of the numerical simulation can be accomplished.
- **C3:** A final sensitivity analysis by varying key parameters enables an assessment of the robustness of the model. Furthermore, critical parameters that significantly influence the numerical model can be identified and/or further specified.
- **C4:** If required by the research question, testing the temporal and spatial upscaling potential of the numerical simulation, considering given limits of the experimental observation, is crucial.
- **D:** Interpretation and reporting should include all laboratory and numerical data and highlight the limitations of the findings.



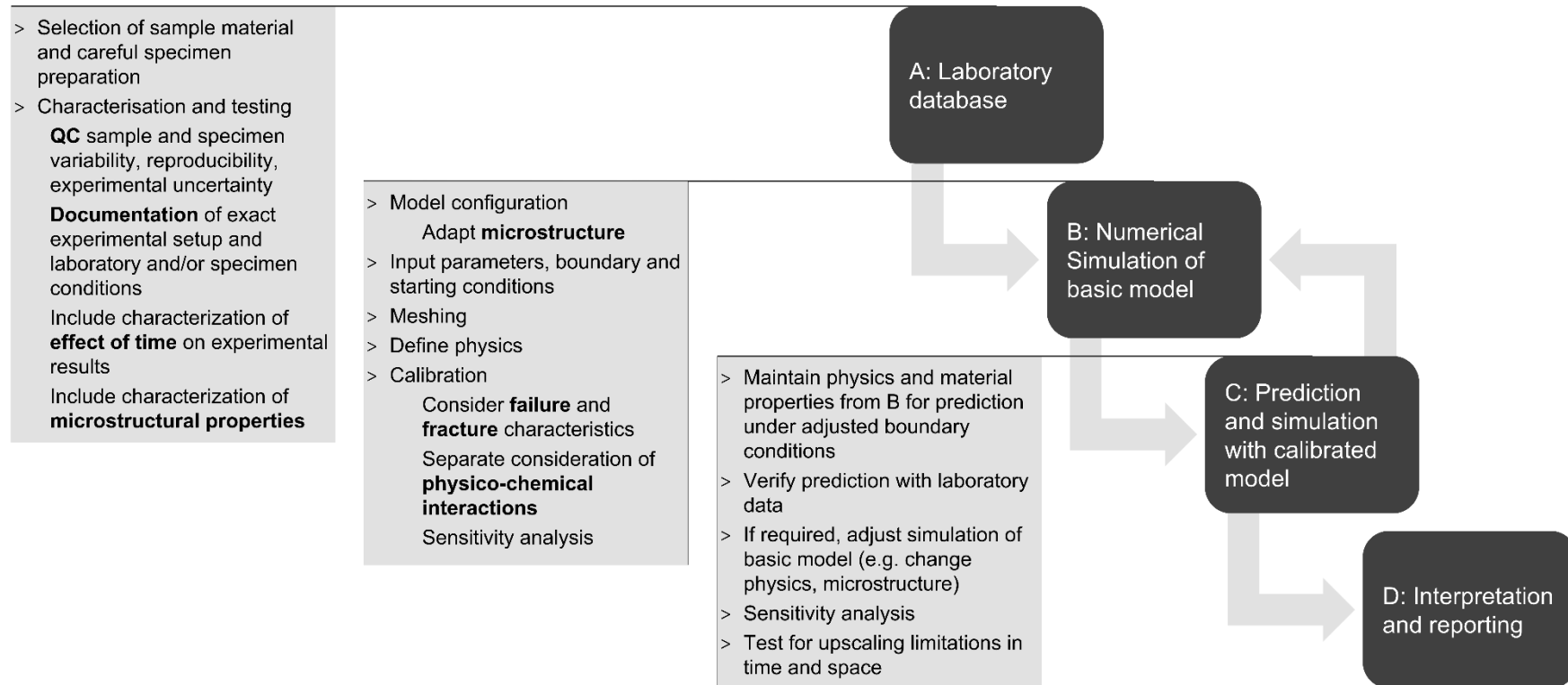


Figure 61: Schematic workflow with several steps for benchmarking.

# Conclusions, outlook and limitations

## 1. Laboratory program

1. The laboratory experimental schedule has been developed specifically for the numerical simulation of time-dependent strength testing processes in granite.
2. Padang granite TG34 was characterised with respect to basic physical and geomechanical properties, such as density (grain and bulk density), porosity (accessible, isolated), thermal properties (thermal conductivity, thermal effusivity, derived heat capacity), permeability, mineralogical composition, texture, ultrasonic-velocities and dynamic moduli, static elastic properties, tensile and compressive failure properties and residual strength properties.
3. During the project period, 70 splitting tensile strength tests, 102 uniaxial and 95 triaxial compressive strength tests were carried out. The accessible and total porosity, ultrasonic P- and S-wave velocity, and thermal conductivity were determined in for specimens prepared for uniaxial and triaxial compressive strength tests.
4. In order to be able to predict the long-term stability of Padang granite TG34, the splitting tensile strength test was carried out at a nominal displacement rate of  $1.5 \cdot 10^{-4}$ ,  $1.5 \cdot 10^{-3}$ , and  $1.5 \cdot 10^{-2}$  mm.s<sup>-1</sup>, and uniaxial and triaxial compressive strength tests were conducted at nominal strain rates of  $1 \cdot 10^{-7}$ ,  $1 \cdot 10^{-6}$ ,  $1 \cdot 10^{-5}$ ,  $1 \cdot 10^{-4}$ , and  $1 \cdot 10^{-3}$  s<sup>-1</sup>.
5. Various lubricants applied to the specimen's end faces were tested to improve the reproducibility of the experimental results and to reduce the influence on strength due to friction between the contact surfaces of the specimens and steel loading plates.
6. Results from uniaxial and triaxial compressive strength tests with various lubricants showed that uniaxial compressive strength 1) is largest, when graphite was used as lubricant, and lowest for Teflon 0.5 mm; 2) is very sensitive to water content, with a significant decrease in strength when samples were saturated; and 3) shows a fairly consistent relation to strain rate, i.e., an increase in compressive strength with increasing strain rate.
7. The hydraulic properties of investigated specimens caused a drainage effect for triaxial compressive strength tests, i.e., triaxial strength is apparently more sensitive to strain rate under saturated conditions compared to uniaxial tests or triaxial tests of dry specimens. The effect is, however, caused by the superposition of two processes: 1) a physico-chemical weakening due to the presence of water, visible at low strain rates when drainage, i.e., maintaining the pore pressure in cracks during inelastic deformation, can be ensured, and 2) dilatancy hardening resulting in an apparent increase in strength at higher strain rates, that is related to insufficient drainage, i.e., pore pressure cannot be maintained locally during inelastic deformation and effective confining pressure increases, causing the bulk sample to fail at higher axial differential stresses. Note

that the apparent similarity of triaxial strength for dry and saturated samples observed at the typical laboratory strain rate of  $1 \cdot 10^{-5} \text{ s}^{-1}$  may tempt one to underestimate the weakening effect of water on the investigated granite samples.

8. Cohesion and angle of internal friction of dry samples do not show a significant relation to strain rate, but for saturated samples angle of internal friction decreases and cohesion increases with increasing strain rate, an observation presumably biased by drainage effects.
9. The fracture friction angle tends to decrease with increasing strain rate.

In order to gain a better understanding of the failure mechanisms of Padang granite TG34, further laboratory tests investigating  $K_{IC}$  [63] and  $K_{IIC}$  [6], which are used to determine fracture toughness and crack growth, are useful. The determination of fracture toughness and crack growth leads to a more reliable data set and can be used for further numerical simulations.

Detailed microscopic investigations using thin section analyses and scanning electron microscopy (SEM) clarify fracture mechanisms and their influence on strength and failure. By investigating the post-failure damage characteristics of time-dependent experiments, the potential for temporal upscaling to long-term processes exceeding the laboratory time scales investigated here can be evaluated.

## 2. Numerical simulation

- > Numerical modeling of complex systems, such as crystalline rocks, requires the simulation of both micro-mechanisms and macro-mechanisms.
- > RS2 software uses mathematical equations to model deformation based on the differential equations of elastic and plastic materials. Consequently, in VGBM rock strength increases linearly with the elastic parameters, such as Young's modulus and Poisson's ratio. However, mechanical fracture parameters, such as internal friction angle and cohesion of grains and joints, do not exhibit a logical relationship with rock strength and thus can be calibrated using a trial and error approach.
- > Since RS2 software employs static equations and a stationary modeling method, it cannot directly simulate time-dependent rock mechanics phenomena, such as experiments with strain rate control. Therefore, the simulation of the effect of strain rate on rock strength was not feasible and had to be simplified with assumptions.
- > The VGBM method in RS2 software effectively simulates the macroscopic and behavior of granite under various tests, including UCS, STS, and TCS.
- > The VGBM method can numerically simulate the effect of using 0.025 mm and 0.5 mm thick Teflon and graphite powder at the contact between the loading plate and the sample to reduce the end friction effect with an accuracy of more than 95 %.
- > COMSOL employs accurate and diverse physical equations in a highly flexible manner, allowing the simulation of different physical environments simultaneously and at any scale, using both stationary and time-dependent methods. This flexibility prevents the use of unrealistic parameter values.

- > In COMSOL, different rock failure criteria are not fully developed within a specific node, making the simulation of the rock failure process challenging and requires coupling of various physical environments.
- > The CPFDM method allows for modeling rock mechanics experiments such as UCS, STS, and TCS with different strain and displacement rates by simulating pre-existing microcracks in the phase field physical environment in COMSOL, achieving an accuracy of over 90 %.
- > The simulation of triaxial tests with pore pressure involves various physical mechanisms, requiring targeted tests to accurately model phenomena such as the stress path, fracture toughness effect and fluid – rock pore interaction.

Given the robust capabilities of COMSOL Multiphysics in simulating experiments under complex and multiphysical boundary conditions, it is recommended to develop advanced models using this software. The following specific steps are suggested:

- > Developing a model for a more detailed study of the effect of microstructure on the simulation results under different testing and boundary conditions
- > Examine the correlation between material coefficients in the phase-field model and fracture toughness, aimed at calibrating the crack phase-field damage model
- > Simulate drainage effects by altering the effective stress field according to fracture progress
- > Create a three-dimensional model to analyse the influence of the intermediate stress tensor in experimental scenarios and three-dimensional crack growth phenomena
- > Test numerical temporal and spatial upscaling potential to predict the long-term behavior of rock mass

### 3. Limitations

The above findings and conclusions are based on a number of limitations associated with the approaches and assumptions associated with this study. These are in particular:

- > All simulations were performed in 2D.
- > The effect of drainage in hydromechanical coupling during deformation of specimens under elevated pore pressure could not be simulated explicitly.
- > Physico-chemical interactions causing chemomechanical coupling, i.e., a change in crack kinetics in the presence of fluid agents, were not simulated explicitly, but with a modification of microstructural model parameters.
- > The validity of temporal upscaling of experimental and numerical findings to strain rates below those investigated in this study remains unclear due to the unknown contribution of microstructural processes, that need further attention.

## 4. Data access

Experimental and numerical data is provided in the digital appendix published as:

Witte L.C., Asghari Chehreh H., Backers T., Duda M., Aydin M. & Parvin S., 2024.  
Digital appendix to 'Predictive capability of coupled rock behaviour – development of an experimentally based benchmark for numerical quality assurance (BeNuQuA)'. ReSeeD Research Data Repository, Research Data Services (RDS) of the Ruhr University Bochum.

# References

- [1] Ambati M. & De L., 2016. Lorenzis, Phase-field modeling of brittle and ductile fracture in shells with isogeometric NURBS-based solid-shell elements. *Computational Methods in Applied and Mechanical Engineering*, 312, 351-373.
- [2] Andreev G.E., 1995. Brittle failure of rock materials. Rotterdam, Balkema.
- [3] ASTM E228-17, 2004. Standard Test Method for Linear Thermal Expansion of Solid Materials with a Push-Rod Dilatometer. ASTM International.
- [4] ASTM D7984-21, 2021. Standard Test Method for Measurement of Thermal Effusivity of Fabrics Using a Modified Transient Plane Source (MTPS) Instrument. ASTM International.
- [5] Aydin A., 2014. Upgraded ISRM Suggested Method for Determining Sound Velocity by Ultrasonic Pulse Transmission Technique.
- [6] Backers T. & Stephansson O., 2012. ISRM Suggested Method for the Determination of Mode II Fracture Toughness. *Rock Mechanics and Rock Engineering*, 45, 6, 1011-1022.
- [7] Bazant Z.P., Bai S.P. & Gettu R., 1993. Fracture of rock: effect of loading rate. *Engineering Fracture Mechanics*, 45, 3, 393-398.
- [8] Bieniawski Z. & Bernede M., 1979. Suggested methods for determining the uniaxial compressive strength and deformability of rock materials: Part 1. Suggested method for determining deformability of rock materials in uniaxial compression. *International Journal of Rock Mechanics and Mining Sciences & Geomechanics Abstracts*, 16, 138-140.
- [9] Bieniawski Z., 1967a. Mechanism of brittle fracture of rock: part I—theory of the fracture process. *International Journal of Rock Mechanics and Mining Sciences & Geomechanics Abstracts*, 4, 4, 405-406.
- [10] Bieniawski Z., 1967b. Mechanism of brittle fracture of rock: part II—experimental studies. *International Journal of Rock Mechanics and Mining Sciences & Geomechanics Abstracts*, 4, 4, 419-423.
- [11] Bolk H., 1980. The Creep test (SCW Record 5). Study Centre for Road Construction: Arnhem, The Netherlands.
- [12] Borden M.J., Hughes T.J., Landis C.M., Anvari A. & Lee I.J., 2016. A phase-field formulation for fracture in ductile materials: Finite deformation balance law derivation, plastic degradation, and stress triaxiality effects. *Computational Methods in Applied and Mechanical Engineering*, 312, 130-166.
- [13] Borden M.J., Verhoosel C.V., Scott M.A., Hughes T.J. & Landis C.M., 2012. A phase-field description of dynamic brittle fracture. *Computational Methods in Applied and Mechanical Engineering* 217, 77-95.
- [14] Bourdin B., Francfort G. A. & Marigo J.J., 2008. The variational approach to fracture. *Journal of Elasticity*, 91, 5-148.
- [15] Brady B., 1971. Effects of inserts on the elastic behaviour of cylindrical materials loaded between rough endplates. *International Journal of Rock Mechanics and Mining Sciences & Geomechanics Abstracts*, 8, 357-69.
- [16] Brown E.T. & Gonano L.P., 1974. Improved compression test technique for soft rock. *Journal of Geotechnical Engineering Division*, 100, 2, 196-199.
- [17] COMSOL Multiphysics 6.2
- [18] Cundall P.A. & Hart R.D., 1992. Numerical modeling of discontinua. *Engineering Computations*. 9, 2, 101-113.

- [19] DIN EN 1936:2007-02, 2007. Prüfverfahren für Naturstein - Bestimmung der Reindichte, der Rohdichte, der offenen Porosität und der Gesamtporosität. Beuth-Verlag, Berlin.
- [20] DIN EN ISO 17892-3:2016-07. Geotechnische Erkundung und Untersuchung – Laborversuche an Bodenproben – Teil 1. Beuth-Verlag, Berlin.
- [21] Duda M. & Renner J., 2013. The Weakening Effect of Water on the Brittle Failure Strength of Sandstone. *Geophysical Journal International*, 192, 3, 1091-1108.
- [22] Eberhardt E., Stead D., Stimpson B. & Read R., 1998. Identifying crack initiation and propagation thresholds in brittle rock. *Canadian Geotechnical Journal*, 35, 222-233.
- [23] Eberhardt E., Stead D. & Stimpson B., 1999. Quantifying progressive prepeak brittle fracture damage in rock during uniaxial compression. *International Journal of Rock Mechanics and Mining Sciences* 36, 361-380.
- [24] Erdogan F. & Sih G.C., 1963. On the crack extension in plates under plane loading and transverse shear. *Journal of Basic Engineering*, 85, 4, 519-527.
- [25] Fabjan T., Ivars D.M. & Vukadin V., 2015. Numerical simulation of intact rock behaviour via the continuum and Voronoi tessellation models: a sensitivity analysis. *Acta Geotechnica Slovenica*, 12, 2, 5-23.
- [26] Feng X., Zhang X., Yang C., Kong R., Liu X. & Peng S., 2017. Evaluation and reduction of the end friction effect in true triaxial tests on hard rocks. *International Journal of Rock Mechanics & Mining Sciences*, 4, 2, 699-704.
- [27] Fu Y., 2005. Experimental quantification and DEM simulation of micro-macro behaviors of granular materials using X-ray tomography imaging. PhD thesis, Louisiana State University.
- [28] Gao F. & Stead D., 2014. The application of a modified Voronoi logic to brittle fracture modelling at the laboratory and field scale. *International Journal of Rock Mechanics and Mining Sciences*, 68, 1-14.
- [29] Goodman R.E., Taylor R.L. & Brekke T.L., 1963. A Model for the Mechanics of Jointed Rock. *Journal of the Soil Mechanics and Foundations Division*, 94, 3.
- [30] Griffith A.A., 1921a. The phenomena of rupture and flow in solids. *Philosophical Transactions of the Royal Society*, 221, 163-197.
- [31] Gui Y.L., Zhao Z.Y., Ji J., Wang X.M., Zhou K.P. & Ma S.Q., 2016. The grain effect of intact rock modelling using discrete element method with Voronoi grains. *Geotechnique Letters*. 6, 2, 136-143.
- [32] Haimson B. & Chang C., 2000. A new true triaxial cell for testing mechanical properties of rock, and its use to determine rock strength and deformability of Westerly granite. *International Journal of Rock Mechanics and Mining Sciences*, 37, 285-296.
- [33] Haynes W.M., Lide D.R. & Bruno T.J., 2015. *CRC Handbook of Chemistry and Physics* 95th Edition, pp 2666.
- [34] He M., Miao J. & Feng J., 2010. Rock burst process of limestone and its acoustic emission characteristics under true-triaxial unloading conditions. *International Journal of Rock Mechanics and Mining Sciences*, 47, 286-98.
- [35] Hoek E. & Brown E.T., 1980. *Underground excavations in rock*. Institution of mining and metallurgy, Hertford. Stephen Austin and Sons Ltd., London, pp 527.
- [36] Hudson J.A. & Harrison J.P., 2000. *Engineering rock mechanics - an introduction to the principles*. Elsevier. G.C.
- [37] ISRM, 2015. *The ISRM Suggested Methods for Rock Characterization, Testing and Monitoring: 2007-2014*, Editor: R. Ulusay. Springer, pp 293.
- [38] Jing L., 2003. A review of techniques, advances and outstanding issues in numerical modelling for rock mechanics and rock engineering. *International Journal of Rock Mechanics and Mining Sciences*, 40, 3, 283-353.

- [39] John M., 1972. The influence of length-to-diameter ratio on rock properties in uniaxial compression; a contribution to standardisation in rock mechanics testing. Council for Scientific and Industrial Research No ME1083/5.
- [40] Kachanov M.L., 1982. A microcrack model of rock inelasticity. Part II: propagation of microcracks. *Mechanics of Material*, 1, 1, 29-41.
- [41] Kazerani T. & Zhao J., 2010. Micromechanical parameters in bonded particle method for modelling of brittle material failure. *International Journal for Numerical and Analytical Methods in Geomechanics*. 34, 18, 1877-1895.
- [42] Kemeny J.M., 1991. A model for non-linear rock deformation under compression due to sub-critical crack growth. *International Journal of Rock Mechanics and Mining Sciences & Geomechanics Abstracts*, 28, 6, 459-467.
- [43] Koelen K., Alber M., Duda M. & Backers T., 2021. Effect of sloppy sample preparation on results from uniaxial compressive strength tests. *IOP Conference Series: Earth and Environmental Sciences* 833 012030. Turin, Italy.
- [44] Kotsovos M.D., 1983. Effect of testing techniques on the post-ultimate behaviour of concrete in compression. *Matériaux et Constructions* 16, 3–12.
- [45] Labuz J.F. & Bridell J.M., 1993. Reducing frictional constraint in compression testing through lubrication. *International Journal of Rock Mechanics and Mining Sciences & Geomechanics Abstracts*, 30, 451-455.
- [46] Lee H. & Haimson B.C., 2011. True triaxial strength, deformability, and brittle failure of granodiorite from the San Andreas Fault Observatory at Depth. *International Journal of Rock Mechanics and Mining Sciences*, 48, 7, 1199-1207.
- [47] Lepique M., 2008. Empfehlung Nr. 10 des Arbeitskreises 3.3. Versuchstechnik Fels der Deutschen Gesellschaft für Geotechnik e. V.: Indirekter Zugversuch an Gesteinsproben - Spaltzugversuch. *Bautechnik* 85, 9, 623-627.
- [48] Lisjak A. & Grasselli G., 2014. A review of discrete modeling techniques for fracturing processes in discontinuous rock masses. *Journal of Rock Mechanics and Geotechnical Engineering*, 6, 4, 301-314.
- [49] Martin C., 1993. The strength of massive Lac du Bonnet granite around underground openings. PhD Thesis, University of Manitoba, USA.
- [50] Martin C. & Chandler N., 1994. The progressive fracture of Lac du Bonnet granite. *International Journal of Rock Mechanics and Mining Sciences & Geomechanics Abstracts*, 31, 643–659.
- [51] Miehe C. & Mauthe S., 2016. Phase field modeling of fracture in multi-physics problems. Part III. Crack driving forces in hydro-poro-elasticity and hydraulic fracturing of fluid-saturated porous media. *Computational Methods in Applied and Mechanical Engineering*, 304, 619-655.
- [52] Miehe C., Welschinger F. & Aldakheel F., 2014. Variational gradient plasticity at finite strains. Part II: Local–global updates and mixed finite elements for additive plasticity in the logarithmic strain space. *Computational Methods in Applied and Mechanical Engineering*, 268, 704-734.
- [53] Miehe C. & Mauthe S., 2015. Phase field modeling of fracture in multi-physics problems. Part I. Balance of crack surface and failure criteria for brittle crack propagation in thermo-elastic solids. *Computational Methods in Applied and Mechanical Engineering*, 294, 449-485.
- [54] Miehe C., Welschinger F. & Hofacker M., 2010. Thermodynamically consistent phase-field models of fracture: variational principles and multi-field FE implementations, *International Journal for Numerical Methods in Engineering* 83, 10, 1273-1311.
- [55] Miehe C., Hofacker M. & Welschinger F., 2010. A phase field model for rate-independent crack propagation: Robust algorithmic implementation based on operator splits. *Computational Methods in Applied and Mechanical Engineering*, 199, 45, 2765-2778.



- [56] Mogi K., 2007. Experimental rock mechanics. Taylor & Francis, London, pp 361.
- [57] Mogi K., 1966. Some precise measurements of fracture strength of rocks under uniform compressive stress. *Felsmechanik und Ingenieurgeologie*, 4, 41-55.
- [58] Mutschler T., 2004. Neufassung der Empfehlung Nr. 1 des Arbeitskreises Versuchstechnik Fels der Deutschen Gesellschaft für Geotechnik e. V.: Einaxiale Druckversuche an zylindrischen Gesteinsprüfkörpern. *Bautechnik*, 81, 825-834.
- [59] Nemat-Nasser S. & Horii H., 1982. Compression-induced nonplanar crack extension with application to axial splitting, exfoliation, and rockburst. *Journal of Geophysical Research*, 87(B8), 6805-6821.
- [60] Nguyen V.P. & Wu J.Y., 2018. Modeling dynamic fracture of solids with a phase-field regularized cohesive zone model. *Computational Methods in Applied and Mechanical Engineering*, 340, 1000-1022.
- [61] Nicksiar M. & Martin C., 2012. Evaluation of methods for determining crack initiation in compression tests on low-porosity rocks. *Rock Mechanics and Rock Engineering*, 45, 607-617.
- [62] Obert L. & Duvall W.I., 1967. Rock mechanics and the Design of Structures in rock. John Wiley & Sons, London, p 650.
- [63] Ouchterlony F., 1988. ISRM Suggested Methods for Determining the Fracture Toughness of Rock. *International Journal of Rock Mechanics and Mining Sciences & Geomechanics Abstracts*, 25, 2, 71-96.
- [64] Pan Z.P., Feng X.T., Hudson J.A., 2009. Study of failure and scale effects in rocks under uniaxial compression using 3D cellular automata. *International Journal of Rock Mechanics and Mining Sciences & Geomechanics Abstracts*, 46, 674-685.
- [65] Potyondy D.O. & Cundall P.A., 2004. A bonded-particle model for rock. *International Journal of Rock Mechanics and Mining Sciences*, 41, 8, 1329-1364.
- [66] Protodyakonov M.M., 1969. Method of determining the strength of rocks under uniaxial compression. In: Protodyakonov MM., Koifman GI. (eds) *Mechanical properties of rocks*, translated from Russian. Israel Program for Scientific Translations, Jerusalem.
- [67] Renner J., Hettkamp T. & Rummel F., 2000. Rock mechanical characterization of an argillaceous host rock of a potential radioactive waste repository. *Rock Mechanics and Rock Engineering*, 33, 3, 153-178.
- [68] Riahi A., Hammah E.R & Curran J.H., 2010. Limits of applicability of the finite element explicit joint model in the analysis of jointed rock problems. 44th US Rock Mechanics Symposium - 5th US/Canada Rock Mechanics Symposium.
- [69] Reißer P., 2022. Empfehlung Nr. 2: Dreiaxiale Druckversuche an Gesteinsproben. In *Empfehlungen des Arbeitskreises 3.3 Versuchstechnik Fels der Deutschen Gesellschaft für Geotechnik e. V. (1. Ed.)* Ernst & Sohn.
- [70] Rocscience Inc. RS2 v. 11.018 2023.
- [71] Rogenes E., Muniz de Farias M. & Rasmussen L.L. 2022. The Continuum Voronoi Block Model for simulation of fracture process in hard rocks. *International Journal for Numerical and Analytical Methods in Geomechanics*, 46, 89-112.
- [72] Shanthraj P., Sharma L., Svendsen B., Roters F. & Raabe D., 2016. A phase field model for damage in elasto-viscoplastic materials. *Computational Methods in Applied and Mechanical Engineering*, 312, 167-185.
- [73] Sandström B. & Tullborg E.L., 2006. Forsmark site investigation. Fracture mineralogy, Results from KFM06B, KFM06C, KFM07A, KFM08A, KFM08B. SKB P-06-226, Svensk Kärnbränslehantering AB, pp 108.
- [74] Shen M. & Chen J., 2006. *Rock Mass Mechanics*, Tongji University. Press, Shanghai, China.
- [75] Sheng D., Westerberg B., Mattsson H. & Axelsson K., 1997. Effects of end restraint and strain rate in triaxial tests. *Computers and Geotechnics*, 21, 163-82.

- [76] Sih G.C., 1991. Mechanics of fracture initiation and propagation: surface and volume energy density applied as failure criterion. Netherlands, Kluwer Academic Publishers.
- [77] Sih G.C., 1974. Strain–energy–density factor applied to mixed mode crack problems. *International Journal of Fracture*, 10, 3, 305-321.
- [78] Stacey T.R., 1981. A simple extension strain criterion for fracture of brittle rock. *International Journal of Rock Mechanics and Mining Sciences & Geomechanics Abstracts*, 18, 469-474.
- [79] Stephens M.B., Fox A., La Pointe, P., Simeonov, A., Isaksson, H., Hermanson, J. & Öhman, J., 2007. Geology Forsmark – Site descriptive modelling, Forsmark stage 2.2. SKB Rapport R-07-45, Svensk Kärnbränslehantering AB.
- [80] Streckeisen, A., 1976. To each plutonic rock its proper name. *Earth Science Reviews* 12.
- [81] Tang L., Ke M. & Yan J-h, 2004. A key problem overlooked during experiments to determine rock properties in the post-peak region. *International Journal of Rock Mechanics and Mining Sciences*, 41, 55-60.
- [82] Tang C., Tham L. & Lee P., 2000. Numerical studies of the influence of microstructure on rock failure in uniaxial compression—part II: constraint, slenderness and size effect. *International Journal of Rock Mechanics and Mining Sciences*, 37, 571-583.
- [83] Thuro K., Plinninger R.J., Zäh S. & Schütz S., 2001. Scale effects in rock strength properties. Part 1: unconfined compressive test and STS test. In: Sarkka P, Elorata P, eds. *ISRM regional symposium, EUROCK 2001, Rock Mechanics – A Challenge for Society*, Espoo, pp 169–74.
- [84] Tuncay E. & Hasancebi N., 2009. The effect of length to diameter ratio of test specimens on the uniaxial compressive strength of rock. *Bulletin of Engineering Geology and the Environment*, 68, 49, 1-497.
- [85] Van Vliet M. & Van Mier J., 1996. Experimental investigation of concrete fracture under uniaxial compression. *Mechanics of Cohesive-frictional Materials*, 1, 115-127.
- [86] Verhoosel C.V. & de Borst R., 2013. A phase-field model for cohesive fracture. *International Journal for Numerical Methods in Engineering*, 96, 1, 43-62.
- [87] Vignollet J., May S., De Borst R. & Verhoosel C.V., 2014. Phase-field models for brittle and cohesive fracture. *Meccanica*, 49, 11, 2587-2601.
- [88] Wichter L., 2022. Empfehlung Nr. 12 des Arbeitskreises 3.3. Versuchstechnik Fels der Deutschen Gesellschaft für Geotechnik e. V.: Mehrstufentechnik bei dreiaxialen Druckversuchen und direkten Scherversuchen.
- [89] Witte L., Duda M., Aydin M., Chehreh AA. & Backers T., 2023. Geomechanical characterization of two granites to establish an experimentally based benchmark for numerical simulation – a laboratory study. 15th ISRM Congress 2023 & 72nd Geomechanics Colloquium. Schubert & Kluckner (eds.).
- [90] Wittke W., 2014. Rock mechanics based on an anisotropic jointed rock model (AJRM). WILEY-VCH. pp 891.
- [91] Xu B., Xu T., Xue Y., Heap M.J., Ranjith P.G., Wasanthe P.L.P. & Li Z., 2022. Phase field modeling of crack growth and interaction in rock. *Geomechanics and Geophysics for Geo-Energy and Geo-Resources*, 8, 180.
- [92] Yang k., Zhang F., Hu D. & Tan X., 2022. Effect of real-time high temperature and loading rate on mode I fracture toughness of granite. *Geothermal Energy*, 10, 14, 1-16.
- [93] Yu J., Wang Y., Wang Q., Zhu Q. & Fu S., 2019. Study of triaxial mechanical test based on MSV method for reducing end friction effect. *Journal of China Three Gorges University*, 41, 5, 59-64.
- [94] Yun X.Y., Mitri H.S., Yang X.L. & Wang Y.K., 2010. Experimental investigation into biaxial compressive strength of granite. *International Journal of Rock Mechanics and Mining Sciences*, 47, 334-341.

- [95] Zhang C., Mitra R., Oh J., Canbulat I. & Hebblewhite B., 2018. Numerical analysis on mining-induced fracture development around river valleys. *International Journal of Mining, Reclamation and Environment*. 32, 7, 463-485.
- [96] Zhou S., Zhuang X., Zhu H. & Rabczuk T., 2018. Phase field modelling of crack propagation, branching and coalescence in rocks. *Theoretical and Applied Fracture Mechanics*, 96, 174-192.
- [97] Zhou S., Rabczuk T. & Zhuang X., 2018. Phase field modeling of quasi-static and dynamic crack propagation: COMSOL implementation and case studies. *Advances in Engineering Software*, 122, 31-49.
- [98] Zhou S.W. & Xia C.C., 2018. Propagation and coalescence of quasi-static cracks in STS disks: an insight from a phase field model. *Acta Geotechnica*, 14, 11, 1–20.
- [99] Zhou S. & Zhuang X., 2018. Adaptive phase field simulation of quasi-static crack propagation in rocks. *Underground Space* 3, 3, 190-205.
- [100] Zipf Jr. R.K., 1992. Analysis of stable and unstable pillar failure using a local mine stiffness method. In: *Proceedings of the workshop on coal pillar mechanics and design*. Washington (DC): U.S. Bureau of Mines, 128–43.

# Digital Appendix

## 1. Geophysical parameters

- > Specimen dimensions, density, porosity
- > Ultrasound velocity, thermal properties

## 2. Geomechanical parameters

- > Splitting tensile strength
- > Uniaxial compressive strength
- > Triaxial compressive strength
- > Triaxial compressive strength with pore pressure

## 3. COMSOL Multiphysics - CPFDM

### 3.1 Models of UCS test simulation

- > UCS strain rate:  $1 \cdot 10^{-5} \text{ s}^{-1}$

### 3.2 Models of STS test simulation

- > STS displacement rate:  $1.5 \cdot 10^{-3} \text{ mm/s}$

### 3.3 Models of TCS test simulation

- > TCS strain rate:  $1 \cdot 10^{-5} \text{ s}^{-1}$ , effective confining stress 3 MPa, pore pressure 6 MPa

## 4. RS2 RocScience - VGBM

### 4.1 Models of UCS test simulation

- > UCS strain rate:  $1 \cdot 10^{-4} \text{ s}^{-1}$  without lubricant
- > UCS strain rate:  $1 \cdot 10^{-4} \text{ s}^{-1}$  with 0.5 mm Teflon sheet
- > UCS strain rate:  $1 \cdot 10^{-4} \text{ s}^{-1}$  with 0.025 mm Teflon sheet
- > UCS strain rate:  $1 \cdot 10^{-4} \text{ s}^{-1}$  with graphite powder

### 4.2 Models of STS test simulation

- > STS displacement rate:  $1.5 \cdot 10^{-3} \text{ mm/s}$

### 4.3 Models of TCS test simulation

- > TCS strain rate:  $1 \cdot 10^{-4} \text{ s}^{-1}$ , confining stress 3 MPa, graphite powder